

Emergent Fermion Dynamical Symmetry for Monolayer Graphene in a Strong Magnetic Field

Mike Guidry^{(1),*} Lian-Ao Wu^{(2),†} and Fletcher Williams^{(1)‡}

⁽¹⁾*Department of Physics and Astronomy, University of Tennessee, Knoxville, Tennessee 37996, USA*

⁽²⁾*Department of Physics, University of the Basque Country UPV/EHU, 48080 Bilbao,*

IKERBASQUE Basque Foundation for Science, 48013 Bilbao, EHU Quantum Center,

University of the Basque Country UPV/EHU, Leioa, Biscay 48940, Spain

(Dated: December 15, 2023)

We review the physics of monolayer graphene in a strong magnetic field, with emphasis on highly collective states that emerge from the weakly interacting system because of correlations (emergent states). After reviewing the general properties of graphene and of electrons in a magnetic field, we give a brief introduction to the integer quantum Hall effect (IQHE) and the fractional quantum Hall effect (FQHE) in a 2D electron gas as foundation to show that monolayer graphene in a magnetic field exhibits both effects, but with properties modified by the influence of the graphene crystal. After giving an introduction to standard methods of dealing with emergent states for this system, we show that an $SO(8)$ fermion dynamical symmetry governs the emergent degrees of freedom and that the algebraic and group properties of the dynamical symmetry provide a new view of strongly correlated states observed in monolayer graphene subject to a strong magnetic field.

PACS numbers: 71.10.-w, 71.27.+a, 74.72.-h

Contents

I. Introduction	2	5. Bulk–Boundary Correspondence	17
II. Some material properties of graphene	2	6. Incompressible States	17
III. Fundamental properties of graphene	3	C. Summary: Integer Quantum Hall Effect	17
IV. Structure of Graphene	3	VIII. The Fractional Quantum Hall Effect	17
A. Electronic structure	3	A. Properties of the fractional quantum Hall state	17
B. Lattice structure	3	B. The Laughlin wavefunction	18
C. Band structure	4	IX. Graphene in Strong Magnetic Fields	18
1. Tight binding approximation	4	A. Quantization of Dirac Landau levels	18
2. Dispersion in graphene	6	B. Degeneracy of Landau levels	19
D. Low-energy excitations	7	X. Quantum Hall Effects in Graphene	21
E. Chirality	9	A. Strength of correlations in graphene	21
V. Classical and Quantum Hall Effects	9	B. The graphene integer quantum Hall effect	21
A. The classical Hall effect	9	C. The effect of strong correlations in graphene	22
B. Quantum Hall effects	10	D. The graphene fractional quantum Hall effect	22
VI. Non-Relativistic Landau Levels	10	XI. $SU(4)$ Quantum Hall Ferromagnetism	22
A. Schrödinger equation and solution	11	A. Degeneracies and filling of Landau levels	22
B. Properties of Landau levels	11	B. $SU(4)$ quantum Hall states in graphene	23
C. Degeneracy and level densities	11	1. Effective Hamiltonian	23
VII. The Integer Quantum Hall Effect	12	2. Symmetry and explicit symmetry breaking	24
A. Discovery of the integer quantum Hall effect	12	XII. Emergent States in Magnetic Fields	26
B. Understanding the integer quantum Hall effect	12	A. The role of correlations	26
1. Impurity scattering and mobility gaps	13	B. Symmetry-breaking interactions	26
2. Edge states and conduction	15	XIII. Low-Energy Collective Modes	27
3. Topology of the 2D Brillouin Zone	15	A. Basis states for collective modes	27
4. Topological Protection of Hall Plateaus	16	B. Most general many-body wavefunction	27
		C. Explicit vs. spontaneous symmetry breaking	28
		XIV. Fermion Dynamical Symmetry	29
		A. The microscopic dynamical symmetry method	29
		B. Dynamical symmetry solution algorithm	29
		C. Validity of the dynamical symmetry approach	30
		XV. Dynamical Symmetry in Graphene	30

*Electronic address: guidry@utk.edu

†Electronic address: lianaowu@gmail.com

‡Electronic address: fletcher.williams@knoxvillecatholic.com

A. Basis states	30
B. SO(8) generators and Lie algebra	30
C. A more physical generator basis	31
D. Coupled representations for pair operators	31
E. SO(8) pair states in graphene	32
F. The SO(8) collective subspace	32
G. Structure of SO(8) pairs	33
1. Pauli restrictions on collective pairs	33
2. Pair and product wavefunctions	34
H. Beyond quantum Hall ferromagnetism	34
I. Graphene SO(8) dynamical symmetries	34
J. Generalized coherent states for graphene	36
1. Another useful generator basis	36
2. SO(8) coherent state energy surfaces	36
3. Physical interpretation of energy surfaces	37
K. Quantum phase transitions	37
L. Universality of Emergent States	38
M. Critical Dynamical Symmetries	40
XVI. Summary and Conclusions	40
A. Resistivity and conductivity tensors	41
B. Anderson localization	41
C. The Gauss–Bonnet and Chern theorems	42
D. U(4) and SU(4) subgroups of SO(8)	43
Acknowledgments	43
References	43

I. INTRODUCTION

Graphene is a crystalline material composed of a single one-atom thick layer of carbon; thus it represents the ideal two-dimensional material. It was first isolated by Geim and Novoselov in 2004, by exfoliating graphite using strips of tape. The common pencil was invented in 1564; it functions because the graphite in its “lead” stacks layers of graphene having strong bonding within layers but weak van der Waals bonding between layers. In writing with a pencil, layers of graphene are sloughed off by breaking the weak bonds between layers and are transferred to the paper; presumably some parts of a line drawn with a pencil consist of a single layer of graphene. Thus, it is likely that graphene has been produced since 1564 by the ordinary practice of writing with pencils, but until 2004 it was thought that the single layer allotrope of carbon atoms perhaps did not exist in its free state. Hence the common view that graphene is easy to produce but difficult to detect, which delayed its discovery for more than 400 years after it was first unknowingly produced.

This paper provides an overview of graphene that emphasizes its role as a laboratory for studying emergent states in pseudo-relativistic matter. There is considerable current interest in samples having two or more layers of graphene, but this review will confine itself to a single layer (*monolayer*

graphene). We will begin by giving a concise overview of graphene as a material, its basic structure at the atomic and crystalline level, and of conventional approaches to studying its emergent states when placed in a strong magnetic field. Then we shall introduce an alternative view of this many-body system that is the primary emphasis of this review: emergent states for monolayer graphene in a strong magnetic field in terms of Lie algebras, Lie groups, and associated fermion dynamical symmetries of the Hamiltonian. Since the Lie algebra and Lie group methodology employed in this discussion may be less familiar than more conventional condensed matter methods for some readers, we will include important details and proofs of various assertions in a supplemental web document [1].

II. SOME MATERIAL PROPERTIES OF GRAPHENE

Graphene has many unusual material properties; let us summarize a few of the more important ones.

- It is planar, with a hexagonal unit cell of area 0.052 nm^2 containing two carbon atoms. Taking the mass of the unit cell to be twice the mass of carbon, the mass density is $\rho = 0.77 \text{ mg m}^{-2}$.
- A single layer of graphene is almost, but not quite, transparent, absorbing $\sim 2.3\%$ of the light passing through it at optical wavelengths. Absorption is additive for multiple layers, so the number of layers in a sample may be inferred by how dark it appears in normal light. This method can be used to distinguish regions of a sample having one, two, three, . . . , layers of graphene after exfoliation with tape, for example.
- The breaking strength of graphene is 42 N m^{-1} , which is ~ 100 times larger than that of a hypothetical film of steel having the same thickness.
- The thermal conductivity of graphene is dominated by phonons and is large, with a measured value of 5000 W/mK that is ten times higher than that of copper.
- The mobility of electrons in graphene is very high. Electric fields can be used to tune charge carriers continuously between electrons and holes, with carrier densities as high as 10^{13} cm^{-2} and carrier mobilities that can exceed $15,000 \text{ cm}^2 \text{ V}^{-1} \text{ s}^{-1}$, even at room temperature and pressure.

As a consequence of such material properties, graphene is of large interest as a basis for new devices and other practical applications. But because of its ideal 2D geometry, non-trivial crystal structure, and unusual electronic properties, it also represents a novel laboratory for fundamental physics, as elaborated in Section III.

III. FUNDAMENTAL PROPERTIES OF GRAPHENE

Because graphene exhibits linear dispersion near the Fermi surface (see Fig. 4), its charge-carrying electrons behave in a manner analogous to that of relativistic electrons described by a Dirac equation, with the fermi velocity v_F (maximum velocity of a fermion in a system) playing a role analogous to that of light speed, where the actual speed of light is $c/v_F \sim 300$ times larger than the graphene fermi velocity. Just as an actual relativistic electron moving very near the speed of light typically has a small rest mass, an electron in graphene near the fermi surface typically displays an effective mass near zero. Thus we may view graphene as *pseudo-relativistic matter* that behaves mathematically as actual Lorentz-invariant, relativistic matter would be expected to behave.

Strongly-correlated, *non-relativistic matter* has been studied extensively in phenomena such as superconductivity. However, before the isolation of graphene it was not easy to observe highly-correlated states for *relativistic fermions* because it was difficult to find them under conditions that could produce the strong particle–particle interactions necessary to form such states. It has been proposed that neutrinos in the hot, dense environs of a core-collapse supernova, or in the early Universe before about one second after the Big Bang, could undergo sufficient interactions to produce a correlated, relativistic, many-body state but no observations yet support this conjecture. As we now discuss, graphene affords a benchtop laboratory for studying strongly-correlated, pseudo-relativistic matter.

In the presence of a magnetic field applied transverse to the sample, a single layer of graphene exhibits both an *integer quantum Hall effect* (IQHE) and a *fractional quantum Hall effect* (FQHE). The integer quantum Hall effect can occur for weakly interacting electrons but FQHE states can exist only because of strong correlations, so observation of a fractional quantum Hall effect for graphene placed in a magnetic field is evidence of strongly-correlated, pseudo-relativistic electronic states. A description of these emergent states will be the overall focus of this review.

IV. STRUCTURE OF GRAPHENE

Let's consider in more detail the electronic and crystal structure of graphene. Since graphene is pure carbon, the obvious point of departure is the chemical bonding tendencies of carbon. In this section we adapt extensively from the presentation of Ref. [2].

A. Electronic structure

Carbon has six electrons in a $1s^2 2s^2 2p^2$ configuration, with the $2s$ and $2p$ orbitals playing the dominant role in chemical bonding. A signature characteristic of carbon is its tendency to hybridize the $2s$ and $2p$ orbitals and form covalent bonds with other atoms. A common hybridization is sp^n , in which the $|2s\rangle$ orbital and n of the $|2p_i\rangle$ orbitals mix. Because graphene

is a planar crystal of carbon atoms bonded to each other, the dominant hybridization is sp^2 , in which the spherically symmetric $2s$ orbital mixes with two of the $2p$ orbitals lying in the same plane (typically chosen to be $2p_x$ and $2p_y$). This gives the orbital geometry illustrated in Fig. 1(a), with three planar bonding orbitals separated by 120° angles. In Fig. 1(b) the schematic structure of benzene is indicated, with the covalent bonding at each vertex between a carbon and two other carbons and a hydrogen corresponding to sp^2 hybridization, with the in-plane bonds termed σ -bonds. The double lines indicate double bonds, with the second bond created by overlap of the non-hybridized $2p_z$ orbitals on adjacent carbons directed perpendicular to the plane of the ring (π -bonds). The π -bonding electrons are delocalized over the ring and the benzene ground state corresponds to a quantum superposition of configurations having the double bonds in alternating positions around the ring.

In Fig. 1(c) we indicate that the planar structure of graphene may be viewed as similar to fitting many benzene rings together geometrically, with the hydrogen stripped off and the bond to hydrogen at each benzene vertex replaced by a covalent bond to a carbon in the adjacent ring. The in-plane σ bonds between the carbon atoms are responsible for the robustness of the lattice structure in all allotropes of carbon; they lead to a σ -band that is completely filled. As in benzene, the p orbital that does not participate in the sp^2 hybridization (typically chosen to be p_z) is perpendicular to the carbon-atom plane and can bind covalently with neighboring carbon atoms, delocalizing and leading to a π -band. In pure graphene each p orbital has one extra electron, so the π -band is half full.

We shall refer to the resulting graphene structure as the *honeycomb lattice*, for obvious geometrical reasons. It is believed that all graphitic compounds (graphite, carbon nanotubes, graphene, and fullerenes) have as their basic building block this honeycomb graphene lattice: *graphite* corresponds to stacks of graphene sheets with strong covalent bonds within the sheets and weak van der Waals forces between the sheets, a *carbon nanotube* corresponds to a graphene sheet rolled into a tube, and a *fullerene* is wrapped-up graphene with pentagons inserted to allow an average spherical shape.

B. Lattice structure

To address the direct (real-space) and reciprocal (momentum-space) graphene lattices it is useful to define the direct lattice vectors illustrated in Fig. 2(a). As described in the figure caption, the graphene lattice may be viewed as bipartite, consisting of two distinct triangular sublattices (labeled A and B in the figure, with the A sublattice indicated by solid blue circles and the B sublattice by open red circles). Alternatively, the lattice may be viewed as triangular, with a two-atom basis. It is common to define a quantum number associated with this distinction between sublattices A and B that takes two values and thus may be described by an $SU(2)$ symmetry that is termed the *sublattice pseudospin*. The lattice vectors are

$$\mathbf{a}_1 = \sqrt{3}a\mathbf{e}_x \quad \mathbf{a}_2 = \frac{\sqrt{3}a}{2}(\mathbf{e}_x + \sqrt{3}\mathbf{e}_y), \quad (1)$$

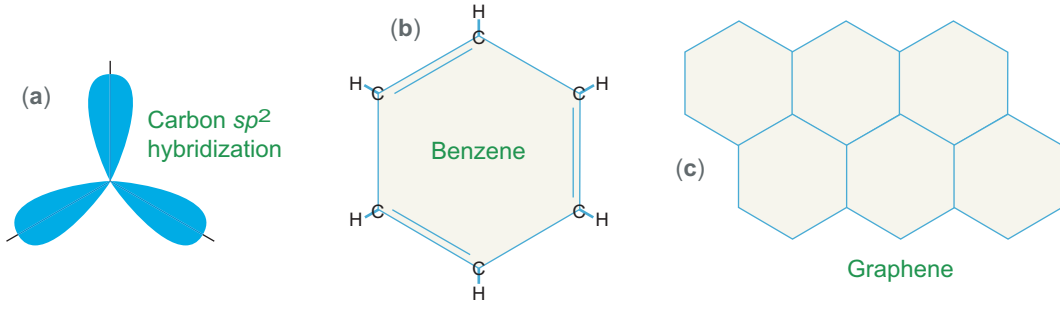


FIG. 1: (a) Carbon sp^2 hybridization. (b) Schematic structure of the ring compound benzene; the actual ground state is a quantum superposition of this configuration and one with the positions of the double and single bonds exchanged. (c) Schematic picture of graphene as an extended set of benzene rings joined together, with each benzene C–H bond replaced by a C–C bond between adjacent rings.

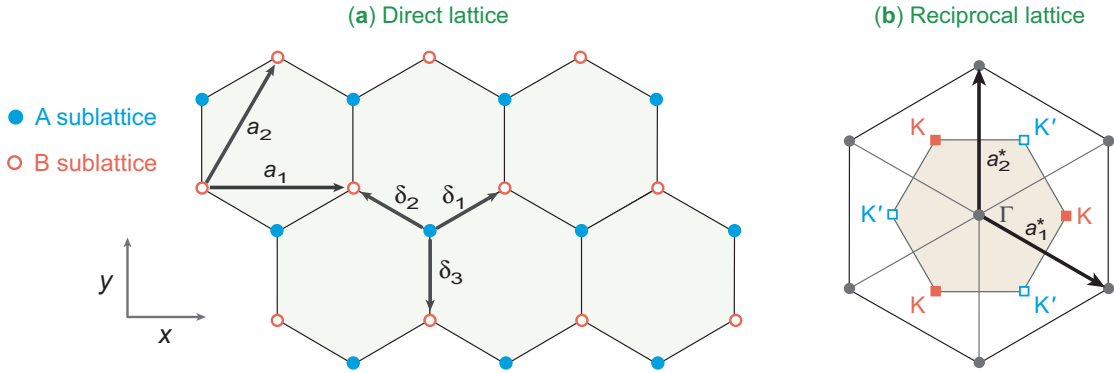


FIG. 2: (a) The direct lattice for graphene. The graphene honeycomb lattice is not a Bravais lattice since from the crystallographic point of view two neighboring sites are inequivalent. It may be viewed as a triangular Bravais lattice with a two-atom basis, A and B, or as bipartite, with interlocking triangular lattices A and B. The vectors \mathbf{a}_1 and \mathbf{a}_2 are the basis vectors of the triangular Bravais lattice. The vectors $\boldsymbol{\delta}_1$, $\boldsymbol{\delta}_2$, and $\boldsymbol{\delta}_3$ connect nearest-neighbor (NN) carbon atoms, with a measured separation of $a = 0.142$ nm. (b) Reciprocal lattice of triangular lattice and first Brillouin zone (shaded). The primitive lattice vectors are \mathbf{a}_1^* and \mathbf{a}_2^* . The center Γ and inequivalent corners K and K' are marked. Adapted from Ref. [2].

where the spacing between carbon atoms is $a \simeq 0.142$ nm. The corresponding reciprocal lattice and Brillouin zone are illustrated in Fig. 2(b). The lattice vectors of the reciprocal lattice are given by

$$\mathbf{a}_1^* = \frac{2\pi}{\sqrt{3}a} \left(\mathbf{e}_x - \frac{\mathbf{e}_y}{\sqrt{3}} \right) \quad \mathbf{a}_2^* = \frac{4\pi}{3a} \mathbf{e}_y, \quad (2)$$

and are illustrated in Fig. 2(b).

C. Band structure

The carbon–carbon bonding in graphene involves in-plane σ -bonds and out-of-plane π -bonds. The σ electrons typically are associated with energy bands far from the Fermi surface while the low-energy electronic properties are primarily associated with the π electrons. Since our primary interest is low-energy states, our focus will be on the π electrons. It is conventional to address the energy bands of the π electrons in graphene using the *tight-binding approximation*, as formulated originally by Wallace in 1947 [3] to study the structure of graphite (then of large practical interest because of the im-

portance of graphite in early nuclear reactors). Our discussion will follow the presentation by Goerbig [2].

1. Tight binding approximation

The honeycomb lattice may be viewed as triangular with two atoms per unit cell, suggesting a trial wavefunction [2]

$$\psi_{\mathbf{k}}(\mathbf{r}) = a_{\mathbf{k}} \psi_{\mathbf{k}}^{(A)}(\mathbf{r}) + b_{\mathbf{k}} \psi_{\mathbf{k}}^{(B)}(\mathbf{r}), \quad (3)$$

where the $\psi_{\mathbf{k}}^{(A)}$ and $\psi_{\mathbf{k}}^{(B)}$ are Bloch functions

$$\psi_{\mathbf{k}}^{(A)}(\mathbf{r}) = \sum_{\mathbf{R}_\ell} \phi^{(A)}(\mathbf{r} + \boldsymbol{\delta}_A - \mathbf{R}_\ell) e^{i\mathbf{k} \cdot \mathbf{R}_\ell}, \quad (4a)$$

$$\psi_{\mathbf{k}}^{(B)}(\mathbf{r}) = \sum_{\mathbf{R}_\ell} \phi^{(B)}(\mathbf{r} + \boldsymbol{\delta}_B - \mathbf{R}_\ell) e^{i\mathbf{k} \cdot \mathbf{R}_\ell}, \quad (4b)$$

for the A and B lattices, respectively, $\boldsymbol{\delta}_A$ and $\boldsymbol{\delta}_B$ are the vectors that connect the sites of the Bravais lattice with the site of the A or B atom, respectively, in the unit cell, and $\phi^{(A)}(\mathbf{r} + \boldsymbol{\delta}_A - \mathbf{R}_\ell)$ and $\phi^{(B)}(\mathbf{r} + \boldsymbol{\delta}_B - \mathbf{R}_\ell)$ are atomic orbital

wavefunctions defined near the A or B atoms, respectively, at the Bravais lattice site \mathbf{R}_ℓ . Utilizing Eq. (3), the Schrödinger equation $H\psi_{\mathbf{k}} = \varepsilon_{\mathbf{k}}\psi_{\mathbf{k}}$ may be written as

$$(a_{\mathbf{k}}^*, b_{\mathbf{k}}^*) H_{\mathbf{k}} \begin{pmatrix} a_{\mathbf{k}} \\ b_{\mathbf{k}} \end{pmatrix} = \varepsilon_{\mathbf{k}} (a_{\mathbf{k}}^*, b_{\mathbf{k}}^*) S_{\mathbf{k}} \begin{pmatrix} a_{\mathbf{k}} \\ b_{\mathbf{k}} \end{pmatrix}, \quad (5)$$

where the *Hamiltonian matrix* $H_{\mathbf{k}}$ is

$$H_{\mathbf{k}} = H_{\mathbf{k}}^\dagger = \begin{pmatrix} \psi_{\mathbf{k}}^{(A)*} H \psi_{\mathbf{k}}^{(A)} & \psi_{\mathbf{k}}^{(A)*} H \psi_{\mathbf{k}}^{(B)} \\ \psi_{\mathbf{k}}^{(B)*} H \psi_{\mathbf{k}}^{(A)} & \psi_{\mathbf{k}}^{(B)*} H \psi_{\mathbf{k}}^{(B)} \end{pmatrix} \quad (6)$$

and the *overlap matrix* $S_{\mathbf{k}}$ reflecting non-orthogonality of the trial wavefunctions is

$$S_{\mathbf{k}} = S_{\mathbf{k}}^\dagger = \begin{pmatrix} \psi_{\mathbf{k}}^{(A)*} \psi_{\mathbf{k}}^{(A)} & \psi_{\mathbf{k}}^{(A)*} \psi_{\mathbf{k}}^{(B)} \\ \psi_{\mathbf{k}}^{(B)*} \psi_{\mathbf{k}}^{(A)} & \psi_{\mathbf{k}}^{(B)*} \psi_{\mathbf{k}}^{(B)} \end{pmatrix}. \quad (7)$$

The Hamiltonian includes an atomic orbital part H^a satisfying

$$H^a \phi^{(j)}(\mathbf{r} + \boldsymbol{\delta}_j - \mathbf{R}_\ell) = \varepsilon^{(j)} \phi^{(j)}(\mathbf{r} + \boldsymbol{\delta}_j - \mathbf{R}_\ell) \quad (8)$$

and a perturbative part ΔV accounting for all other terms not contained in the atomic-orbital Hamiltonian. Then the matrix components of Eq. (6) for N unit cells may be written as

$$H_{\mathbf{k}}^{ij} = N(\varepsilon^{(j)} s_{\mathbf{k}}^{(ij)} + t_{\mathbf{k}}^{(ij)}), \quad (9)$$

where i and j denote A or B, we have utilized Eqs. (4) and defined

$$s_{\mathbf{k}}^{ij} \equiv \sum_{\mathbf{R}_\ell} e^{i\mathbf{k}\cdot\mathbf{R}_\ell} \int d^2r \phi^{(i)*}(\mathbf{r}) \phi^{(j)}(\mathbf{r} + \boldsymbol{\delta}_{ij} - \mathbf{R}_\ell) = \frac{S_{\mathbf{k}}^{ij}}{N} \quad (10)$$

with $\boldsymbol{\delta}_{ij} \equiv \boldsymbol{\delta}_j - \boldsymbol{\delta}_i$, and the *hopping matrix* $t_{\mathbf{k}}^{ij}$ is defined by

$$t_{\mathbf{k}}^{ij} \equiv \sum_{\mathbf{R}_\ell} e^{i\mathbf{k}\cdot\mathbf{R}_\ell} \int d^2r \phi^{(i)*}(\mathbf{r}) \Delta V \phi^{(j)}(\mathbf{r} + \boldsymbol{\delta}_{ij} - \mathbf{R}_\ell). \quad (11)$$

The electronic bands corresponding to eigenvalues of the Schrödinger equation follow from the secular equation

$$\det[H_{\mathbf{k}} - \varepsilon_{\mathbf{k}}^\lambda S_{\mathbf{k}}] = \det \left[t_{\mathbf{k}}^{ij} - (\varepsilon_{\mathbf{k}}^\lambda - \varepsilon^{(j)}) s_{\mathbf{k}}^{ij} \right] = 0, \quad (12)$$

which has two solutions labeled by the band index λ for the case of two atoms per unit cell. For the special case where the atoms on the different sublattices have the same electronic configurations, the onsite energy $\varepsilon^{(i)}$ is a physically irrelevant constant for all i that may be omitted and for graphene

$$\det \left[t_{\mathbf{k}}^{ij} - \varepsilon_{\mathbf{k}}^\lambda s_{\mathbf{k}}^{ij} \right] = 0, \quad (13)$$

determines the bands in the tight-binding approximation.

To solve this equation we may choose the Bravais lattice vectors to correspond to the A sublattice, with the equivalent site on the B sublattice obtained from $\boldsymbol{\delta}_B = \boldsymbol{\delta}_{AB} = \boldsymbol{\delta}_3$, as illustrated in Fig. 3, and include nearest-neighbor (NN) and next-

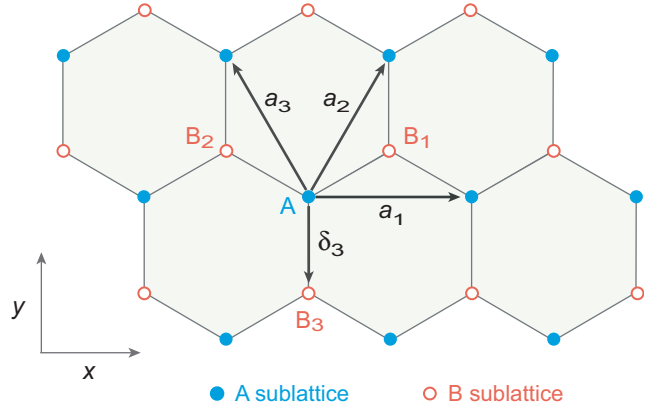


FIG. 3: Vectors for a tight-binding model with nearest-neighbor (NN) and next-nearest-neighbor (NNN) interactions in graphene [2].

nearest-neighbor (NNN) terms. From Fig. 3, the NN hopping amplitude t connects points on *different* sublattices and is given by

$$t \equiv \int d^2r \phi^{A*}(\mathbf{r}) \Delta V \phi^B(\mathbf{r} + \boldsymbol{\delta}_3), \quad (14)$$

while the NNN hopping amplitude connects points on the *same* sublattice and is given by

$$t_{\text{NNN}} \equiv \int d^2r \phi^{A*}(\mathbf{r}) \Delta V \phi^A(\mathbf{r} + \mathbf{a}_1). \quad (15)$$

The atomic orbitals are assumed normalized

$$\int d^2r \phi^{(i)*}(\mathbf{r}) \phi^{(i)}(\mathbf{r}) = 1, \quad (16)$$

the overlap correction for NN site orbitals is

$$s \equiv \int d^2r \phi^{A*}(\mathbf{r}) \phi^B(\mathbf{r} + \boldsymbol{\delta}_3), \quad (17)$$

and the overlap corrections for sites that are not nearest-neighbor are assumed to be small and will be neglected.

For an arbitrary site on the A sublattice the off-diagonal terms of the hopping matrix [$i \neq j$ in Eq. (11), meaning that the hopping is between the A and B sublattices] consist of three terms corresponding to the nearest neighbors B_1 , B_2 , and B_3 , as illustrated in Fig. 3 (since we are neglecting higher than NNN couplings). All of these have the same hopping amplitude but different phases. From Fig. 3 the site B_3 is described by the same lattice vector as the site A (shifted by $\boldsymbol{\delta}_3$), so the phase factor in the hopping matrix Eq. (11) is just 1. But the site B_1 is shifted by the vector \mathbf{a}_2 relative to B_3 and so contributes a phase factor $\exp(i\mathbf{k} \cdot \mathbf{a}_2)$, while the site B_2 is shifted by the vector \mathbf{a}_3 relative to B_3 and so contributes a phase factor $\exp(i\mathbf{k} \cdot \mathbf{a}_3)$. Defining the sum of the NN phase factors at \mathbf{k} by

$$\gamma_{\mathbf{k}} \equiv 1 + e^{i\mathbf{k} \cdot \mathbf{a}_2} + e^{i\mathbf{k} \cdot \mathbf{a}_3}, \quad (18)$$

the off-diagonal elements of the hopping matrix may be written as $t_{\mathbf{k}}^{AB} = (t_{\mathbf{k}}^{BA})^* = t \gamma_{\mathbf{k}}^*$ (with the convention that $t_{\mathbf{k}}^{AB}$ corresponds to hopping from B to A), and the overlap matrix as

$$s_{\mathbf{k}}^{AB} = (s_{\mathbf{k}}^{BA})^* = s \gamma_{\mathbf{k}}^* \quad s_{\mathbf{k}}^{AA} = s_{\mathbf{k}}^{BB} = 1, \quad (19)$$

where the values of the diagonal terms follow from the normalization (16). The NNN hopping amplitudes yield the diagonal elements of the hopping matrix in our approximation, since they connect sites on the same sublattice,

$$t_{\mathbf{k}}^{\text{AA}} = t_{\mathbf{k}}^{\text{BB}} = 2t_{\text{NNN}} \sum_{i=1}^3 \cos(\mathbf{k} \cdot \mathbf{a}_i) = t_{\text{NNN}} (|\gamma_{\mathbf{k}}|^2 - 3). \quad (20)$$

Thus, upon inserting these results in Eq. (13) the secular equation takes the form

$$\det \begin{bmatrix} t_{\mathbf{k}}^{\text{AA}} - \varepsilon_{\mathbf{k}} & (t - s\varepsilon_{\mathbf{k}})\gamma_{\mathbf{k}}^* \\ (t - s\varepsilon_{\mathbf{k}})\gamma_{\mathbf{k}} & t_{\mathbf{k}}^{\text{AA}} - \varepsilon_{\mathbf{k}} \end{bmatrix} = 0, \quad (21)$$

which has two solutions labeled by the band index $\lambda = \pm 1$,

$$\varepsilon_{\mathbf{k}}^{\lambda} = \frac{t_{\mathbf{k}}^{\text{AA}} + \lambda t |\gamma_{\mathbf{k}}|}{1 + \lambda s |\gamma_{\mathbf{k}}|}. \quad (22)$$

As a first approximation, it may be assumed that the overlap s is much less than one and that the NN interaction dominates the NNN interaction so that $t_{\text{NNN}} \ll t$. Expanding Eq. (22) with these assumptions gives

$$\begin{aligned} \varepsilon_{\mathbf{k}}^{\lambda} &\simeq t_{\mathbf{k}}^{\text{AA}} + \lambda t |\gamma_{\mathbf{k}}| - st |\gamma_{\mathbf{k}}|^2 \\ &= \lambda t |\gamma_{\mathbf{k}}| + (t_{\text{NNN}} - st) |\gamma_{\mathbf{k}}|^2, \end{aligned} \quad (23)$$

where a constant $-3t_{\text{NNN}}$ has been omitted. (Thus the effect of the overlap s at the present level of approximation is to renormalize the strength of the next-nearest-neighbor hopping.) Finally, inserting Eq. (18) into Eq. (23) yields the dispersion relation

$$\begin{aligned} \varepsilon_{\mathbf{k}}^{\lambda} &= \lambda t \sqrt{f_{\mathbf{k}}} + (t_{\text{NNN}} - st) f_{\mathbf{k}}, \\ f_{\mathbf{k}} &\equiv 3 + 2 \sum_{i=1}^3 \cos(\mathbf{k} \cdot \mathbf{a}_i). \end{aligned} \quad (24)$$

Comparison with more sophisticated numerical calculations or spectroscopic measurements suggests that reasonable physical choices for the parameters are

$$t \sim 3 \text{ meV} \quad (t_{\text{NNN}} - st) \sim 0.1t \sim 0.3 \text{ meV},$$

which justifies the expansion used in going from Eq. (22) to Eq. (23). From the vectors in Fig. 3, the scalar products $\mathbf{k} \cdot \mathbf{a}_i$ in Eq. (24) may be evaluated to give

$$\begin{aligned} \mathbf{k} \cdot \mathbf{a}_1 &= \sqrt{3}ak_x & \mathbf{k} \cdot \mathbf{a}_2 &= \frac{\sqrt{3}a}{2} (k_x + \sqrt{3}k_y) \\ \mathbf{k} \cdot \mathbf{a}_3 &= \frac{\sqrt{3}a}{2} (-k_x + \sqrt{3}k_y) \end{aligned} \quad (25)$$

and $f_{\mathbf{k}}$ is given explicitly by

$$\begin{aligned} f_{\mathbf{k}} &= 3 + 2 \cos(\sqrt{3}ak_x) + 2 \cos\left(\frac{\sqrt{3}a}{2}(k_x + \sqrt{3}k_y)\right) \\ &\quad + 2 \cos\left(\frac{\sqrt{3}a}{2}(-k_x + \sqrt{3}k_y)\right) \\ &= 3 + 2 \cos(\sqrt{3}ak_x) \\ &\quad + 4 \cos\left(\frac{\sqrt{3}a}{2}k_x\right) \cos\left(\frac{3a}{2}k_y\right), \end{aligned} \quad (26)$$

where $2 \cos \theta \cos \phi = \cos(\theta - \phi) + \cos(\theta + \phi)$ was used in the last step. Figure 4 illustrates the electronic dispersion for graphene calculated using Eqs. (24) and (26). The valley isospin labels in Fig. 4(c) will be discussed further below.

2. Dispersion in graphene

In Fig. 4 the valence band π , corresponding to $\lambda = -1$, and the conduction band π^* , corresponding to $\lambda = +1$, meet at six discrete points that are termed *K points*. As shown in Fig. 4(b), near the K points the dispersion is approximately linear. Since a linear dispersion is characteristic of the Dirac equation for ultrarelativistic massless electrons, these points are also termed the *Dirac points*, and the dispersion in the vicinity of a Dirac point is called a *Dirac cone*. In Fig. 4(d) we show experimental evidence that the effective mass of graphene electrons approaches zero near the Dirac points (where the electron density vanishes). As we shall elaborate further below, the low-energy excitations of graphene are expected to look formally like those of *relativistic, massless fermions*.

Each carbon atom contributes one π electron and in the ground state the lower band is completely full and the upper band is completely empty. Thus, the Fermi surface lies at the Dirac points where the π band and π^* bands just touch, corresponding to $\varepsilon_{\mathbf{k}}^{\lambda} = 0$. From Eq. (23), this condition requires the real and imaginary parts of $\gamma_{\mathbf{k}}$ to vanish. From Eqs. (18) and (25) we require the simultaneous conditions

$$\begin{aligned} \text{Re } \gamma_{\mathbf{k}} &= 1 + \cos\left(\frac{\sqrt{3}a}{2}(k_x + \sqrt{3}k_y)\right) \\ &\quad + \cos\left(\frac{\sqrt{3}a}{2}(-k_x + \sqrt{3}k_y)\right) = 0, \\ \text{Im } \gamma_{\mathbf{k}} &= \sin\left(\frac{\sqrt{3}a}{2}(k_x + \sqrt{3}k_y)\right) \\ &\quad + \sin\left(\frac{\sqrt{3}a}{2}(-k_x + \sqrt{3}k_y)\right) = 0, \end{aligned}$$

where $e^{ix} = \cos x + i \sin x$ has been used. Since sine is an odd function the second of these equations is satisfied if $k_y = 0$. Inserting that into the first of the above equations gives $k_x = \pm 4\pi/(3\sqrt{3}a)$. Thus there are two solutions, K and K', corresponding to

$$\mathbf{K} = +\frac{4\pi}{3\sqrt{3}a} \mathbf{e}_x \quad \mathbf{K}' = -\frac{4\pi}{3\sqrt{3}a} \mathbf{e}_x. \quad (27)$$

As illustrated in Fig. 5, there are two other equivalent points that are connected to the K solution by the reciprocal lattice vectors \mathbf{a}_1^* and \mathbf{a}_2^* defined in Eq. (2) and Fig. 2. Likewise, there are two other equivalent points connected to the K' solution by reciprocal lattice vectors. The sets K and K' are distinct, representing the two independent solutions of Eq. (27). The solutions come in pairs because the band Hamiltonian (6) is time-reversal invariant ($H_{\mathbf{k}} = H_{-\mathbf{k}}^*$). Hence if \mathbf{k} is a solution

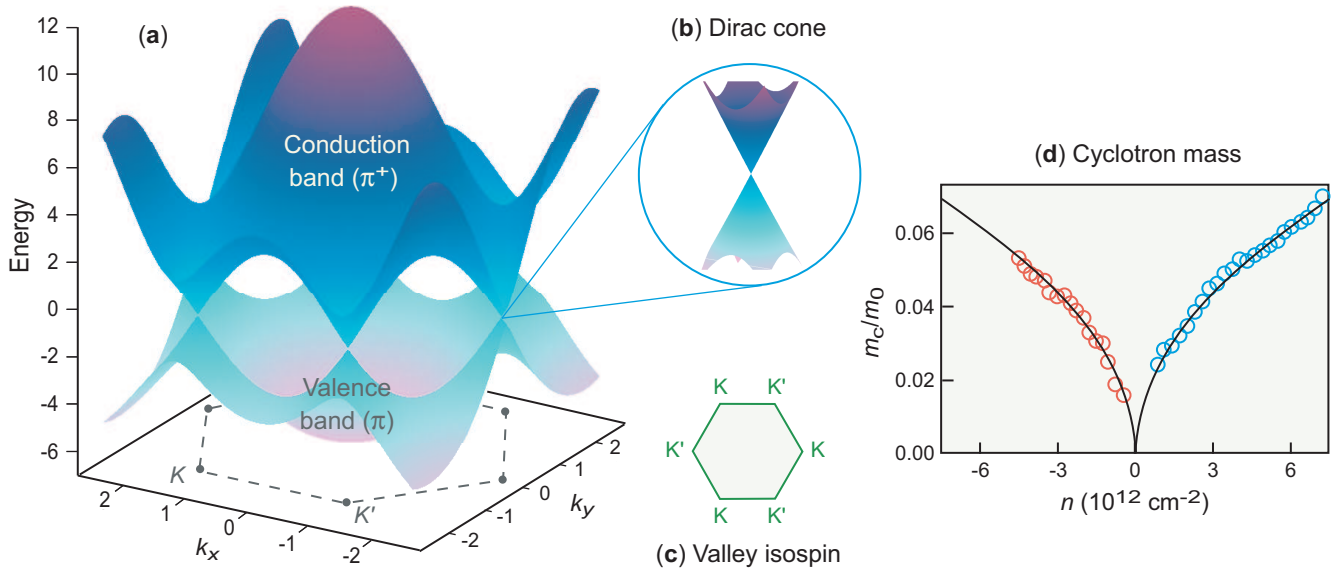


FIG. 4: (a) Electronic dispersion [energy versus momentum (k_x, k_y)] of graphene calculated from Eqs. (24) and (26) in a tight-binding model with no magnetic field; figure adapted from Ref. [4]. Two inequivalent points in the Brillouin zone (points not connected by reciprocal lattice vectors) are labeled K and K' . (b) Near these K -points the dispersion is approximately linear, leading to six Dirac cones, three labeled by K and three labeled by K' . The Fermi surface for undoped graphene lies at zero energy in this diagram (in the plane where the cones just touch), and the level density vanishes there for undoped graphene. This implies that the electrons near the Fermi surface are described by a Dirac equation. (c) The six minima in the conduction band at the Dirac cones are called *valleys*, which are labeled by K or K' . The two possible valley labels K or K' for an electron are termed *valley isospin*. (d) The cyclotron mass of electrons in graphene, adapted from Ref. [5]. Near the Dirac cones of Fig. 4(a) the electronic number density vanishes ($n = 0$), since the level density tends to zero; the data indicate that the electrons become essentially massless there and hence obey a massless Dirac equation.

of $\epsilon_{\mathbf{k}} = 0$, so is $-\mathbf{k}$. Because of the lattice symmetry there is only one such independent (K, K') pair in the Brillouin zone.

Thus, the six Dirac points can be divided into two sets of three, corresponding to the points K and K' in Fig. 2(b). The points K are all equivalent because they are connected by reciprocal lattice vectors; likewise for the points K' . The inequivalent points K and K' constitute a 2-dimensional degree of freedom called the *valley isospin* (or just *isospin* for brevity) $\xi = \pm 1$, so-called because a two-component wavefunction can be treated formally as a “spin” [fundamental rep-

resentation of $SU(2)$], similar to the isotopic spin formalism of nuclear physics]. One says that there is a *two-fold valley degeneracy* in graphene labeled by the quantum number ξ . This degeneracy is expected to survive approximately for excitations having energy much smaller than the bandwidth $\sim |t|$, since they are restricted to the vicinity of a given K -point.

D. Low-energy excitations

Let us now consider the low-energy excitations expected in graphene. The Hamiltonian and dispersion relations derived above are complicated by the non-orthogonality of the atomic wavefunctions, which necessitates the overlap integrals (10). As noted in conjunction with Eq. (23), the primary effect of the overlaps is to renormalize the strengths of next-nearest-neighbor hopping. For low-energy excitations in particular, the overlap effect should be small and it is convenient to absorb it into NNN hopping amplitudes and define an *effective tight-binding Hamiltonian* that takes the form [2]

$$H_{\mathbf{k}} \simeq t \begin{pmatrix} 0 & \gamma_{\mathbf{k}}^* \\ \gamma_{\mathbf{k}} & 0 \end{pmatrix} + t_{\text{NNN}} \begin{pmatrix} |\gamma_{\mathbf{k}}|^2 & 0 \\ 0 & |\gamma_{\mathbf{k}}|^2 \end{pmatrix}. \quad (28)$$

The corresponding eigenvectors are the spinors

$$\psi_{\mathbf{k}}^{\lambda} = \begin{pmatrix} a_{\mathbf{k}}^{\lambda} \\ b_{\mathbf{k}}^{\lambda} \end{pmatrix}, \quad (29)$$

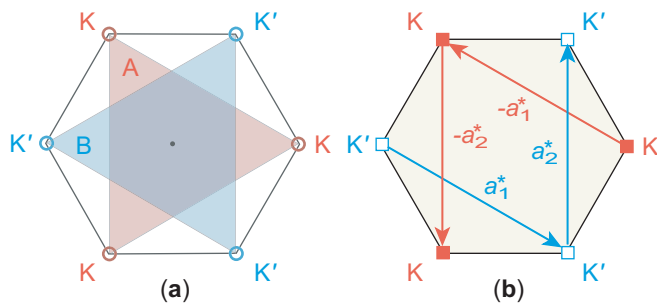


FIG. 5: (a) The graphene A sublattice (red triangle connecting sites labeled by K) and B sublattice (blue triangle connecting points labeled by K') are related by inversion. (b) The points K and K' form inequivalent sets of three connected by reciprocal lattice vectors.

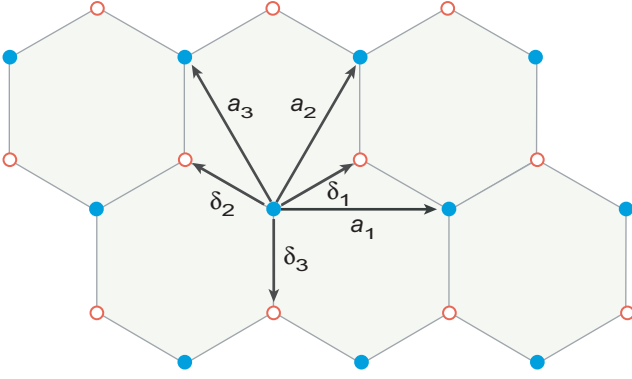


FIG. 6: Relationship among the vectors δ_i and a_i . Adapted from Ref. [2].

with components that are the amplitudes for the Bloch wavefunctions of Eqs. (4a) and (4b) on the two different sublattices A and B.

From Fig. 4, the low-energy excitations in graphene are expected to occur in the vicinity of the Dirac points $\pm\mathbf{K}$. We decompose the wavevector \mathbf{k} as

$$\mathbf{k} = \pm\mathbf{K} + \mathbf{q}, \quad (30)$$

where we assume that $|\mathbf{q}| \ll |\mathbf{K}| \sim a^{-1}$ and expand the energy dispersion around $\pm\mathbf{K}$. The relative phase between the two sublattice components that we used above was an arbitrary choice. As a consequence, the dispersion relation (23) is unaffected by a change $\gamma_{\mathbf{k}} \rightarrow \gamma_{\mathbf{k}} \exp(i g_{\mathbf{k}})$ for any real, nonsingular function $g_{\mathbf{k}}$ and it is convenient to use this freedom to replace Eq. (18) with the more symmetric expression

$$e^{i\mathbf{k}\cdot\delta_3} \gamma_{\mathbf{k}} = e^{i\mathbf{k}\cdot\delta_1} + e^{i\mathbf{k}\cdot\delta_2} + e^{i\mathbf{k}\cdot\delta_3} = \sum_{i=1}^3 e^{\pm i\mathbf{k}\cdot\delta_i}, \quad (31)$$

where the relationship of the vectors δ_i and a_i that is illustrated in Fig. 6 has been used to write $\mathbf{a}_2 + \delta_3 = \delta_1$ and $\mathbf{a}_3 + \delta_3 = \delta_2$ [2, 6]. Thus

$$e^{i\mathbf{k}\cdot\delta_3} \gamma_{\mathbf{k}|_{\mathbf{k}=\pm\mathbf{K}+\mathbf{q}}} = \sum_{i=1}^3 e^{i(\pm\mathbf{K}+\mathbf{q})\cdot\delta_i} = \sum_{i=1}^3 e^{\pm i\mathbf{K}\cdot\delta_i} e^{i\mathbf{q}\cdot\delta_i}. \quad (32)$$

Assuming \mathbf{q} to be a small displacement from \mathbf{K} and expanding the last exponential in the preceding expression to second order gives

$$\begin{aligned} \gamma_{\mathbf{q}}^{\pm} &\equiv e^{i\mathbf{k}\cdot\delta_3} \gamma_{\mathbf{k}|_{\mathbf{k}=\pm\mathbf{K}+\mathbf{q}}} \\ &= \sum_{i=1}^3 e^{\pm i\mathbf{K}\cdot\delta_i} \left(1 + i\mathbf{q}\cdot\delta_i - \frac{1}{2}(\mathbf{q}\cdot\delta_i)^2 \right) \\ &= \sum_{i=1}^3 e^{\pm i\mathbf{K}\cdot\delta_i} + i \sum_{i=1}^3 e^{\pm i\mathbf{K}\cdot\delta_i} (\mathbf{q}\cdot\delta_i) \\ &\quad - \frac{1}{2} \sum_{i=1}^3 e^{\pm i\mathbf{K}\cdot\delta_i} (\mathbf{q}\cdot\delta_i)^2 \\ &\equiv (\gamma_{\mathbf{q}}^{\pm})^{(0)} + (\gamma_{\mathbf{q}}^{\pm})^{(1)} + (\gamma_{\mathbf{q}}^{\pm})^{(2)}. \end{aligned} \quad (33)$$

From the geometry in Fig. 6, the components of the vectors δ_i are

$$\begin{aligned} \delta_1^x &= \frac{\sqrt{3}}{2}a & \delta_2^x &= -\frac{\sqrt{3}}{2}a & \delta_3^x &= 0, \\ \delta_1^y &= \frac{a}{2} & \delta_2^y &= \frac{a}{2} & \delta_3^y &= -a. \end{aligned} \quad (34)$$

The zero-order term in Eq. (33) vanishes:

$$(\gamma_{\mathbf{q}}^{\pm})^{(0)} = \sum_{i=1}^3 e^{\pm i\mathbf{K}\cdot\delta_i} = e^{\pm 2\pi i/3} + e^{\mp 2\pi i/3} + 1 = 0,$$

where Eqs. (27) and (34), and that $e^{ix} + e^{-ix} = 2\cos x$, were used. Thus, if second and higher order terms are neglected,

$$e^{i\mathbf{k}\cdot\delta_3} \gamma_{\mathbf{k}|_{\mathbf{k}=\pm\mathbf{K}+\mathbf{q}}} = (\gamma_{\mathbf{q}}^{\pm})^{(1)} = i \sum_{i=1}^3 e^{\pm i\mathbf{K}\cdot\delta_i} (\mathbf{q}\cdot\delta_i). \quad (35)$$

From Eq. (34)

$$\begin{aligned} \mathbf{q}\cdot\delta_1 &= \frac{\sqrt{3}}{2}aq_x + \frac{a}{2}q_y & \mathbf{q}\cdot\delta_2 &= -\frac{\sqrt{3}}{2}aq_x + \frac{a}{2}q_y, \\ \mathbf{q}\cdot\delta_3 &= -aq_y, \end{aligned}$$

which may be used to evaluate Eq. (35); to this order [2]

$$\gamma_{\mathbf{q}}^{\pm} \simeq \mp \frac{3}{2}a(q_x \pm iq_y). \quad (36)$$

To deal with the \pm and \mp symbols that follow from the two-fold degeneracy of solutions in Eq. (27), it is convenient to employ the *valley isospin quantum number* ξ introduced earlier, with $\xi = +1$ corresponding to the K point at \mathbf{K} and $\xi = -1$ to the K' point at $-\mathbf{K}$ [modulo translations by reciprocal lattice vectors; see Eq. (27) and Fig. 5]. Thus, Eq. (36) becomes

$$\gamma_{\mathbf{q}}^{\xi} = -\frac{3}{2}\xi a(q_x + i\xi q_y). \quad (37)$$

Since we are evaluating only to first order, the t_{NNN} term in Eq. (28) may be dropped and inserting the preceding expression for $\gamma_{\mathbf{k}}$ in Eq. (28) gives

$$H_k^{\xi} \simeq t \begin{pmatrix} 0 & \gamma_k^{\xi} \\ \gamma_k & 0 \end{pmatrix} \simeq -\frac{3}{2}\xi at \begin{pmatrix} 0 & q_x - i\xi q_y \\ q_x + i\xi q_y & 0 \end{pmatrix}$$

as the effective low-energy Hamiltonian. Defining a Fermi velocity

$$v_F \equiv \frac{-3at}{2\hbar} = \frac{3a|t|}{2\hbar} \quad (38)$$

(where t is generally negative), gives for the Hamiltonian

$$H_k^{\xi} = \hbar\xi v_F \begin{pmatrix} 0 & q_x - i\xi q_y \\ q_x + i\xi q_y & 0 \end{pmatrix}, \quad (39)$$

which may be expressed as

$$H_q^{\xi} = \hbar\xi v_F (q_x \sigma^x + \xi q_y \sigma^y), \quad (40)$$

upon utilizing the standard 2×2 representations of the Pauli matrices σ^x and σ^y . The dispersion at this level of approximation is obtained by dropping the term proportional to t_{NNN} from Eq. (23) and inserting $\gamma_{\mathbf{k}}$ from Eq. (37), giving

$$\varepsilon_{\mathbf{k}} = \lambda t |\gamma_{\mathbf{q}}| = \frac{3}{2} a \lambda t |\mathbf{q}| = \hbar v_{\text{F}} \lambda |\mathbf{q}|, \quad (41)$$

where Eq. (38) was used. The energy $\varepsilon_{\mathbf{k}}$ depends on the band index λ but not the valley isospin ξ .

E. Chirality

The sublattice symmetry of graphene (two interlocking triangular sublattices) should be approximately valid for low energy excitations. Since it corresponds to two degrees of freedom, it is convenient to describe it in terms of a pseudospin $\boldsymbol{\sigma}$ that takes two values. To the degree that the sublattice symmetry is respected, there is an associated conserved quantity. For actual relativistic electrons it is convenient to express the spin degree of freedom in terms of helicity, which is the projection of the spin on the direction of motion. Since the solution near the Dirac points (low-energy states) behaves effectively as that for massless relativistic electrons, it is convenient to define the helicity $\eta_{\mathbf{q}}$ operator associated with projection of the sub-lattice pseudospin on the wavevector by [2]

$$\eta_{\mathbf{q}} \equiv \frac{\boldsymbol{\sigma} \cdot \mathbf{q}}{|\mathbf{q}|}, \quad (42)$$

which has eigenvalues $\eta_{\mathbf{q}} |\eta = \pm 1\rangle = \pm |\eta = \pm 1\rangle$. The helicity for *massless particles* commutes with the Dirac Hamiltonian, so it is a conserved quantum number.

For massless particles the helicity is the same as the *chirality* (“handedness”), which is the eigenvalue of the Dirac γ_5 operator. We shall assume electrons near the Dirac points to be exactly massless [see Fig. 4(d)], so that their helicity and chirality may be identified. It is common to refer to these fermions as *massless chiral fermions*, and to the sublattice symmetry as *conservation of chirality*. (Remember that this is a “pseudo-chirality” associated with the sublattice pseudospin, not the actual spin s of the electron.) The band index λ is the product of the sublattice chirality and the valley isospin, $\lambda = \eta \xi$. Conservation of chirality implies that there is no backscattering of electrons upon encountering a slowly-varying barrier, since to rotate the wavevector by π would flip the sign of the chirality. From the tight-binding model, the effective low-energy Hamiltonian at the corners of the Brillouin zone may be written

$$H = \hbar v_{\text{F}} \boldsymbol{\sigma} \cdot \mathbf{p}, \quad (43)$$

which is equivalent to the Dirac equation for massless chiral fermions (also called the *Weyl equation*), but with the speed of light c replaced by the Fermi velocity v_{F} .

V. CLASSICAL AND QUANTUM HALL EFFECTS

The integer and fractional quantum Hall effects represent remarkable physics that appears when a strong magnetic field

is applied to a low-density electron gas confined to two dimensions at very low temperature. These effects were first observed in the early 1980s for 2D electron gases created in semiconductor devices. To understand the quantum Hall effect in graphene it is important to understand the basics of this extensive earlier work. This section gives a general introduction to the quantization of non-relativistic electrons in a magnetic field that is the basis of the quantum Hall effect, and the following two sections give a general introduction to the integer and fractional quantum Hall effects, respectively. Then we shall be prepared to address the issue of quantum Hall effects in graphene.

A. The classical Hall effect

Let’s begin by recalling the basics of the classical Hall effect. In Fig. 7(a), an electric field E_x causes a current j_x to flow through a thin rectangular sample in the x direction. In Fig. 7(b) a uniform magnetic field B_z is placed on the sample in the positive z direction, which causes a deflection of the electrons in the y direction (Lorentz force). As indicated in Fig. 7(c), electrons accumulate on one edge and a positive ion excess accumulates on the opposite edge, producing a transverse electric field E_y (the *Hall field*) that in steady state just cancels the Lorentz force produced by the magnetic field. As a result, the current is entirely in the x direction and for uniform samples the Hall field is perpendicular to the current, in the direction $\mathbf{j} \times \mathbf{B}$. Typically the transverse voltage V_{H} and the longitudinal voltage V_{L} are measured in the experiment, as indicated in Fig. 7(d).

The situation may be analyzed quantitatively in terms of the classical Lorentz force \mathbf{F} acting on the electrons in the magnetic field,

$$\mathbf{F} = -e \left(\mathbf{E} + \frac{1}{c} \mathbf{v} \times \mathbf{B} \right), \quad (44)$$

where \mathbf{B} is a magnetic field oriented in the $+z$ direction, \mathbf{E} is the electric field, and \mathbf{v} is the electron velocity (taken to be in the x direction). Requiring forces in the y direction to cancel,

$$F_y = -e \left(E_y - \frac{1}{c} v_x B_z \right) = 0,$$

implies that the transverse electric field and the perpendicular magnetic field are related by

$$E_y = \frac{1}{c} v_x B_z. \quad (45)$$

The velocity \mathbf{v} can be estimated using a force derived from the Drude model [7–9],

$$\mathbf{F} = m \left(\frac{d\mathbf{v}}{dt} + \frac{\mathbf{v}}{\tau} \right) = -e \left(\mathbf{E} + \frac{1}{c} \mathbf{v} \times \mathbf{B} \right), \quad (46)$$

where m is the effective mass of an electron and τ is the mean time between electron collisions. In steady state, $d\mathbf{v}/dt = 0$

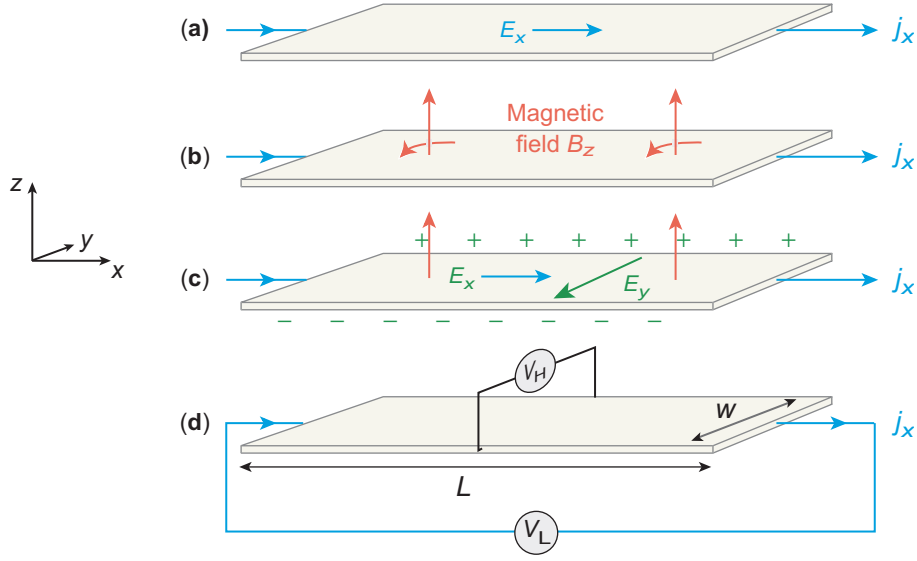


FIG. 7: The classical Hall effect. (a) An electric field E_x causes a current j_x to flow through a thin rectangular sample in the x direction. (b) A uniform magnetic field B_z is placed on the sample in the positive z direction. The curved arrows indicate the Lorentz-force response of the electrons to the magnetic field, causing a deflection in the y direction. (c) This causes electrons to accumulate on one edge and a positive ion excess on the opposite edge, producing a transverse electric field E_y (the Hall field) that just cancels the force produced by the magnetic field. Adapted from Ref. [4]

and the equations of motion are

$$\begin{aligned} v_x &= -\frac{e\tau}{m}E_x - \omega_c\tau v_y, & v_y &= -\frac{e\tau}{m}E_y + \omega_c\tau v_x, \\ v_z &= -\frac{e\tau}{m}E_z, \end{aligned} \quad (47)$$

where $B \equiv B_z = |\mathbf{B}|$ and the *cyclotron frequency* ω_c is defined by

$$\omega_c \equiv \frac{eB}{mc}. \quad (48)$$

Inserting the first of Eqs. (47) into Eq. (45) gives a relationship between the transverse electric field E_y and longitudinal electric field E_x ,

$$E_y = \frac{B}{c}v_x = \frac{B}{c}\left(-\frac{e\tau}{m}E_x - \omega_c\tau v_y\right) = -\frac{eB\tau}{mc}E_x, \quad (49)$$

where at equilibrium $v_y = 0$ has been required. If τ is the mean collision time for an electron, the current density may be approximated in the Drude model as

$$\mathbf{j} = \frac{e^2n_e}{m}\tau\mathbf{E} = \sigma\mathbf{E} \quad \sigma \equiv \frac{ne^2\tau}{m}, \quad (50)$$

where n_e is the electron number density and σ is the conductance.

In a Hall effect experiment, one typically measures the transverse voltage V_H and the longitudinal voltage $V_L = E_x\ell$, where ℓ is the distance over which the voltage changes by V_L . If the sample is approximated as 2D with transverse width w [see Fig. 7(a)], the relationship between the Hall voltage V_H , Hall field E_y , and total current I is given by

$$E_y = \frac{V_H}{w} \quad I = wj_x. \quad (51)$$

The *Hall resistance* R_H is then defined by [see Appendix A]

$$R_H = \frac{V_H}{I} = \frac{wE_y}{wj_x} = \frac{E_y}{j_x} = -\frac{B}{ecn_e}, \quad (52)$$

where Eqs. (49)–(51) were used. Likewise, the longitudinal resistance R_L is given by

$$R_L = \frac{V_L}{I} = \frac{LE_x}{wj_x} = \frac{\ell}{w\sigma}, \quad (53)$$

where (50) was used. Now let us see how this classical picture is modified by quantum effects, guided by the presentation in Ref. [4].

B. Quantum Hall effects

A much richer set of possibilities is found when Hall effect experiments are performed at low temperatures and high magnetic fields. These *quantum Hall effects (QHE)* can be separated into two sets of phenomena:

1. the *integer quantum Hall effect (IQHE)*, and
2. the *fractional quantum Hall effect (FQHE)*.

To understand these quantum Hall effects we must first examine the quantization of electrons confined to two dimensions in a strong magnetic field.

VI. NON-RELATIVISTIC LANDAU LEVELS

Consider the quantum description of non-relativistic electrons in a 2D gas with a strong magnetic field transverse to the 2D

plane. The magnetic field will lead to substantial spin polarization, so we assume states to have a single electron spin polarization and neglect the constant Zeeman energy for each polarized spin. This is not strictly justified since some spin effects are observable even at high magnetic field, but it should not change substantially the general features that we shall emphasize. Initially the Coulomb interaction also will be neglected relative to the effect of the strong magnetic field, but we will return to its effect later.

A. Schrödinger equation and solution

This section follows the presentation by Phillips [9]. By the usual minimal prescription to ensure gauge invariance, the effect of an electromagnetic field may be included by adding to the momentum operator $\mathbf{p} = (p_x, p_y)$ a term depending on the vector potential and the Hamiltonian may be written

$$H = \frac{1}{2m} \left(\frac{\hbar}{i} \nabla + \frac{e}{c} \mathbf{A} \right)^2, \quad (54)$$

where \mathbf{A} is a 3-vector potential having a curl equal to the magnetic field \mathbf{B} :

$$\mathbf{B} = \nabla \times \mathbf{A} \quad \mathbf{B} \equiv (B_x, B_y, B_z) = (0, 0, B). \quad (55)$$

Various gauge choices give this magnetic field. Two common ones are the *Landau gauge* and the *symmetric gauge*, which are defined by

$$\mathbf{A} = (0, Bx, 0) \quad (\text{Landau gauge}), \quad (56a)$$

$$\mathbf{A} = \frac{B}{2}(-y, x, 0) \quad (\text{symmetric gauge}). \quad (56b)$$

The electromagnetic field is unchanged by gauge transformations, so *no physical quantities depend on the gauge choice*, but the forms of the vector potential \mathbf{A} and wavefunction ψ do. That is not an ambiguity because \mathbf{A} and ψ are *not observables* in this context.

It will prove convenient for the initial discussion to work in the Landau gauge, $\mathbf{A} = (0, Bx, 0)$, so that $A_y = Bx$ and $A_x = 0$ (with the z dimension neglected, since we are concerned with 2D electron gases). The Schrödinger equation is then

$$-\frac{\hbar^2}{2m} \left[\partial_x^2 + \left(\partial_y - \frac{ieBx}{\hbar c} \right)^2 \right] \psi(x, y) = E\psi(x, y), \quad (57)$$

with m the effective mass, $\partial_y \equiv \partial/\partial y$, and $\partial_x^2 \equiv \partial^2/\partial x^2$. Since the Hamiltonian does not depend on y in the chosen gauge, it is convenient to write the wavefunction in the separable form $\psi(x, y) = \phi(x)e^{iky}$. Inserting this into Eq. (57) indicates that $\phi(x)$ obeys

$$\frac{\hbar\omega_c}{2} \left[-\Lambda^2 \partial_x^2 + \left(\frac{x}{\Lambda} - \Lambda k \right)^2 \right] \phi(x) = E\phi(x), \quad (58)$$

where $\omega_c = eB/mc$ is the cyclotron frequency of Eq. (48) and the *magnetic length* Λ is

$$\Lambda \equiv \sqrt{\frac{\hbar c}{eB}}. \quad (59)$$

But Eq. (58) is just the harmonic-oscillator Schrödinger equation, so the wavefunction is of harmonic oscillator form

$$\psi_{nk}(x, y) = H_n \left(\frac{x}{\Lambda} - \Lambda k \right) e^{-(x-x_k)^2/2\Lambda^2} e^{iky}, \quad (60)$$

where H_n is a Hermite polynomial and $x_k = \Lambda^2 k$. The corresponding energy is

$$\varepsilon_n = \hbar\omega_c \left(n + \frac{1}{2} \right), \quad (61)$$

which depends on the principle Landau quantum number $n = 0, 1, 2, \dots$, but not on k .

B. Properties of Landau levels

From Eq. (60) the wavefunction is extended in y but localized in x near $x_k = \Lambda^2 k$. This is specific to our gauge choice: under a local gauge transformation the vector potential $A(\mathbf{r}, t)$ and the wavefunction $\psi(\mathbf{r}, t)$ are changed simultaneously according to

$$A(\mathbf{r}, t) \rightarrow A(\mathbf{r}, t) + \nabla\chi(\mathbf{r}, t), \quad (62a)$$

$$\psi(\mathbf{r}, t) \rightarrow \psi(\mathbf{r}, t) e^{i\hbar c\chi(\mathbf{r}, t)/e}, \quad (62b)$$

where $\mathbf{r} \equiv (x, y)$ and $\chi(\mathbf{r}, t)$ is some scalar function, so the forms of both \mathbf{A} and ψ (but *no observable quantities*) depend on the gauge chosen. If L is the spatial extent in the y direction, $k_m = 2\pi m/L$, with m an integer. Therefore the spacing in k is given by

$$k_{m+1} - k_m = \frac{2\pi}{L}. \quad (63)$$

Energy levels labeled by n in Eq. (61) are termed *Landau levels*. Semiclassically, they correspond to electrons moving in circles of quantized radius specified by the quantum number n , with quantization arising from requiring an integer number of electron de Broglie wavelengths to fit around the cyclotron orbit. For a given Landau orbit the radius of the circle is termed the *cyclotron radius* and the center of the circle is termed the *guiding center* [see Fig. 16(b)]. Landau levels are highly degenerate in strong magnetic fields because there are many possible locations for the center of the circle of some radius defining a cyclotron orbit.

C. Degeneracy and level densities

The degeneracy for a Landau level labeled by n is equal to the number of k values associated with that n . If electronic interactions are neglected, the level density $g(\varepsilon)$ is a series of δ -functions at energies corresponding to discrete values of n , weighted by a degeneracy factor N equal to the number of electrons that can occupy the Landau level,

$$g(\varepsilon) = N \sum_n \delta \left[\varepsilon - \hbar\omega_c \left(n + \frac{1}{2} \right) \right]. \quad (64)$$

For a 2D sample of monolayer graphene having width w , length ℓ , and magnetic length Λ ,

$$N = \frac{B\ell w}{hc/e} = \frac{\ell w}{2\pi\Lambda^2}. \quad (65)$$

Equation (65) has a simple physical interpretation. The magnetic flux through a 2D sample of area $A = \ell w$ is $B\ell w$, so N is the magnetic flux in units of the quantum of magnetic flux, hc/e , where h is Planck's constant, e is the electronic charge, and c is the speed of light. From Eq. (65), the number of states per unit area in each Landau level is

$$n_B = \frac{B}{hc/e} = \frac{1}{2\pi\Lambda^2}, \quad (66)$$

which does not depend on the Landau level but scales linearly with the strength of the magnetic field. Thus, *large magnetic fields imply large degeneracies*. If the actual number density of electrons is n_e , a *filling factor* ν may be defined by

$$\nu \equiv \frac{n_e}{n_B} = \frac{n_e hc}{eB}. \quad (67)$$

If ν is an integer, the lowest ν Landau levels will be filled completely and all other Landau levels will be empty, while if ν is not integer a Landau level will be partially filled. For ν equal to an integer m there will be m completely-filled Landau levels and there will be an energy gap between the $n = m$ and $n = m + 1$ Landau levels. Thus, at $T = 0$ the flow of charge is suppressed because electronic excitation is inhibited by the gap.

VII. THE INTEGER QUANTUM HALL EFFECT

What happens to the classical Hall effect for a dilute 2D electron gas at very low temperature and very strong magnetic field? If the filling factor ν given by Eq. (67) is an integer the Hall conductance $\sigma_H = 1/R_H$ becomes quantized, since

$$\sigma_H = \frac{1}{R_H} = -\frac{ecn_e}{B} = -\frac{ec\nu n_B}{B} = \nu \frac{-e^2}{h} \quad (68)$$

As electrons are added beyond ν completely filled Landau levels, they will go into the next level. One might expect that the longitudinal conductance σ_L would at first increase with added electrons until the level becomes half full, and then decrease with addition of further electrons until the level becomes completely full, as illustrated by the dashed curves in Fig. 8(a). However, that is not what is found. Instead,

1. the longitudinal conductance is finite only in narrow ranges [solid blue peaks in Fig. 8(a)], and
2. the Hall conductance σ_H has very flat plateaus in the regions around integer filling factor ν that coincide with regions of very small longitudinal conductance, as illustrated in Fig. 8(b).

The next section will describe these quantum Hall experiments and attempt to understand these properties.

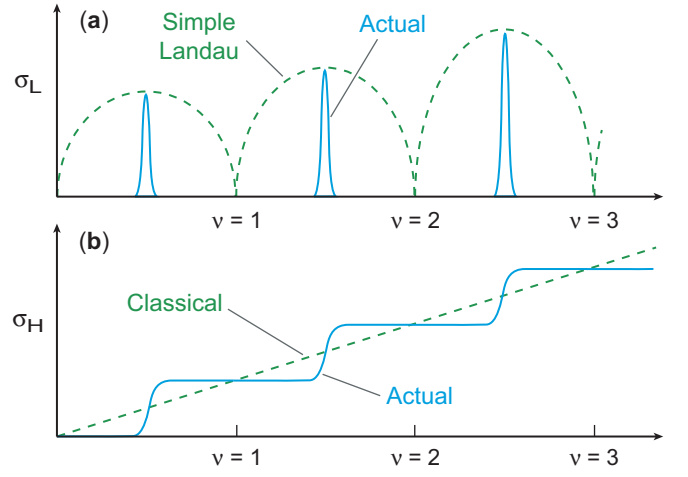


FIG. 8: Conductance as a function of Landau-level filling factors ν . (a) Longitudinal conductance σ_L . (b) Hall conductance σ_H . Dashed green curves indicate the expectation from simple considerations. Solid blue curves suggest what is actually observed (compare experimental data in Fig. 9).

A. Discovery of the integer quantum Hall effect

The integer quantum Hall effect (IQHE) was discovered in 1980 by von Klitzing, Dorda, and Pepper [10]. Experimental data exhibiting the IQHE are shown in Fig. 9 and a schematic experimental apparatus is illustrated in Fig. 10. In the classical Hall effect the Hall resistance R_H should increase linearly with field strength, according to Eq. (52), while the longitudinal resistance R_L should be independent of the magnetic field, according to Eq. (53). This is approximately true for magnetic fields with strength less than about 1 tesla in Fig. 9, but for stronger fields the Hall resistance R_H develops plateaus where it remains constant with increasing magnetic field at values

$$R_H = \rho_{yx} = \frac{V_y}{I_x} = \frac{h}{ne^2} \quad (69)$$

(see Appendix A for the definition of the resistivity tensor ρ_{ij}), where n is an integer, and in the center of regions where R_H is constant the longitudinal resistance R_L behaves as $R_L \simeq \exp(-\Delta/2k_B T)$, which tends to zero as $T \rightarrow 0$, indicating the onset of charge transport without dissipation. This is suggestive of an energy gap of magnitude Δ suppressing the scattering at low temperature. The plateaus in R_H are associated with quantization of the Hall conductance, with the precision of the quantization being remarkably high (of order one part in a billion). This behavior constitutes the *integer quantum Hall effect* (IQHE). The IQHE diverges from classical behavior at larger magnetic fields; let's see if we can understand this using the quantum Landau-level theory of Section VI.

B. Understanding the integer quantum Hall effect

The integer quantum Hall effect does not require electron–electron or electron–phonon correlations for its explanation.

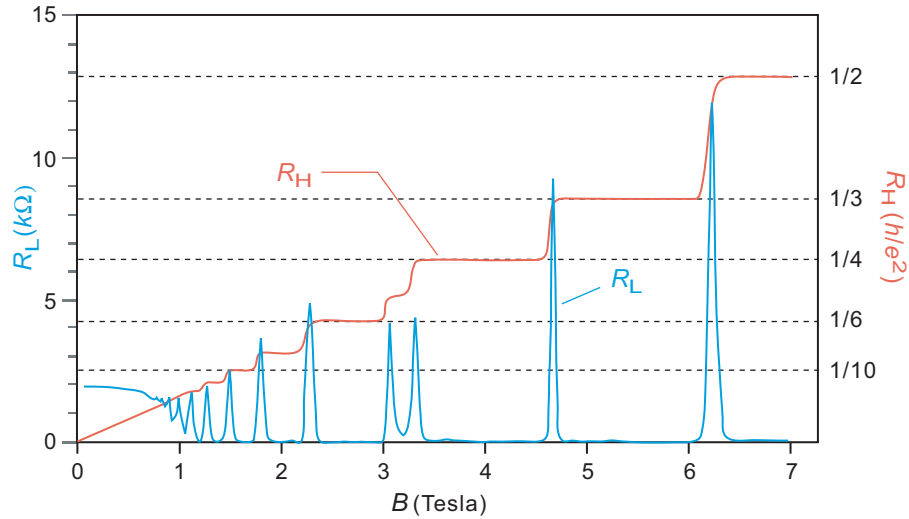


FIG. 9: Data showing the integer quantum Hall effect [10]. The Hall resistance R_H varies stepwise between plateaus with changes in magnetic field B (upper curve). Step height is given by the physical constant h/e^2 divided by an integer i . The figure shows steps for $i = 2, 3, 4, 5, 6, 8$ and 10. The lower curve with multiple peaks represents the ohmic (longitudinal) resistance R_L , which is finite at transitions between plateaus, but drops to almost zero over each plateau.

It related solely to the filling of Landau levels with non-interacting electrons and our discussion of quantized Landau levels in Section VI, supplemented by impurity scattering effects and topological constraints to be discussed below, provides an understanding of its essential features. As implied by Eq. (65), the number of electrons that can be accommodated by each Landau level is governed by the magnetic field strength B . At certain special values of the field strength B a match between the number of electrons and the capacity of

the Landau levels causes an integer number of Landau levels to become exactly filled, producing (in outline) the integer quantum Hall effect. At these special values of B the ratio of the number of electrons per unit area to the number of units of flux h/e^2 , which is the filling factor ν defined in Eq. (67), takes integer values. However, this simple Landau-level picture is not sufficient to understand all features of Fig. 9. Level filling and the associated “shell closures” suggest the broad outlines of the IQHE, but there are two essential details of Fig. 9 that remain unexplained.

1. The longitudinal resistance is very near zero over the entire filling-factor range of a plateau in the Hall resistance.
2. The individual plateaus of Fig. 9 have heights quantized with a precision as high as one part in 10^9 for broad ranges of filling factors.

The first suggests that only some states in a Landau level contribute to longitudinal conductance. The second hints at a fundamental principle responsible for quantizing the Hall resistance that renders it insensitive to details. As will now be shown, the first is explained by the effect of impurities on the transport properties of the electron gas, and the second by a conserved topological quantum number that protects quantization of the Hall resistance.

1. Impurity scattering and mobility gaps

The integer quantum Hall effect is observed for impure samples and the effect increases up to a point with increased impurity concentration. Let us try to understand that. Impurities break translational invariance and increase resistance by scattering charge carriers, so we must consider the influence of

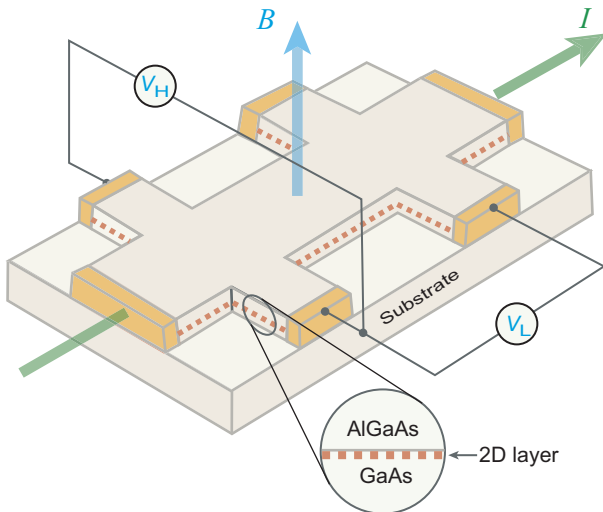


FIG. 10: Schematic diagram of a Hall bar experimental apparatus employing a gallium arsenide heterostructure. The dotted red line indicates the 2D electron gas at the interface between the gallium arsenide (GaAs) and aluminum gallium arsenide (AlGaAs) layers. The magnetic field is B , the electrical current is I , the Hall voltage is V_H , and the longitudinal voltage is V_L . Adapted from Ref. [11].

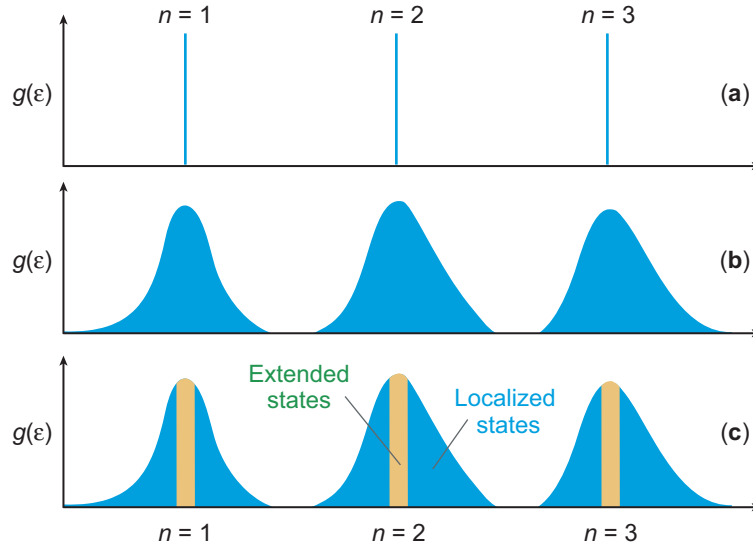


FIG. 11: Level densities $g(\epsilon)$ for a 2D electron gas in a strong magnetic field. (a) In the clean limit, Landau level densities correspond to δ -functions, as in Eq. (64). (b) Interactions with impurities lead to a broadening of the δ -function distributions. (c) The broadened peaks consist of extended states near the centroids and localized states in the wings. Adapted from a figure in Ref. [4].

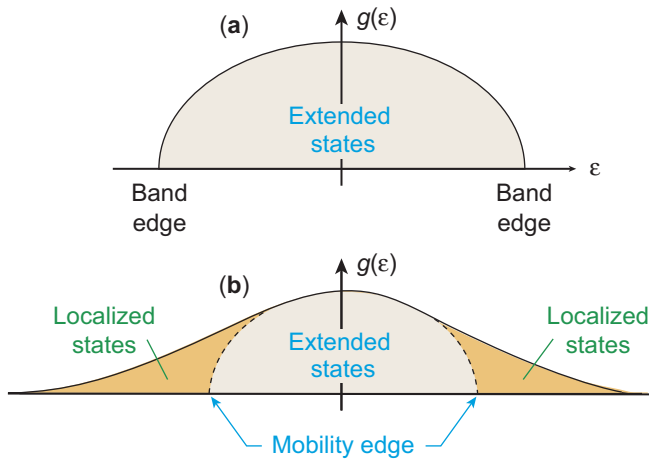


FIG. 12: Density of states (a) for a band in the clean limit and (b) for a band in a disordered system. The mobility edges mark the boundary between localized and extended states.

disorder and impurity scattering on the results of Fig. 9. First note that the electronic states in a sample may be separated broadly into two categories.

1. Some states are *extended (metallic) states*, with wavefunctions that fall off slowly with distance; such states facilitate charge transport and *increase the conductance*.
2. Some states are *localized (insulating) states*, with wavefunctions that are finite only in a small region; such states suppress charge transport and *increase the resistance*.

The effect of impurities on charge transport is often framed in

terms of *Anderson localization*, which is described briefly in Appendix B. The Anderson model of localization is difficult to solve exactly but qualitative insight from it will suffice for our discussion.

Figure 11(a) illustrates the density of states implied by Eq. (64) for a clean system, which corresponds to δ -functions for each Landau level n , weighted by a degeneracy factor N depending on the magnetic field strength. For disordered samples the δ -functions are broadened into peaks of finite width by impurity scattering, as illustrated in Fig. 11(b). Intuitively, impurity scattering tends to localize a state and impede charge transport, with stronger impurity scattering implying greater deviation of the energy from the clean limit. Thus, as suggested in Fig. 11(c), only states near the centers of the broadened peaks in Fig. 11(b) are extended spatially and can carry a current, with the states in the wings of the peaks localized by impurity scattering so that they are insulating.

The general idea is illustrated in Fig. 11(c) and Fig. 12. In Fig. 12(a) the density of states expected as a function of energy for a band in a clean system is illustrated. Figure 12(b) indicates that the effect of impurity scattering is to spread those states in energy, with states near the center of the resulting distribution being spatially extended and those on the wings being spatially localized, with a *mobility edge* characterizing the boundary between the two regions. This leads to *mobility gaps*, corresponding to ranges of energies having localized states that do not support charge transport.

The influence of the magnetic field is crucial for the present argument. Normally in a 2D system all current-carrying states are destroyed by even a tiny amount of impurity scattering. However, *this conclusion can be invalidated by the presence of a magnetic field*, which breaks time-reversal symmetry and interferes with scattering processes that promote localization. Thus, *2D systems subject to a magnetic field can carry cur-*

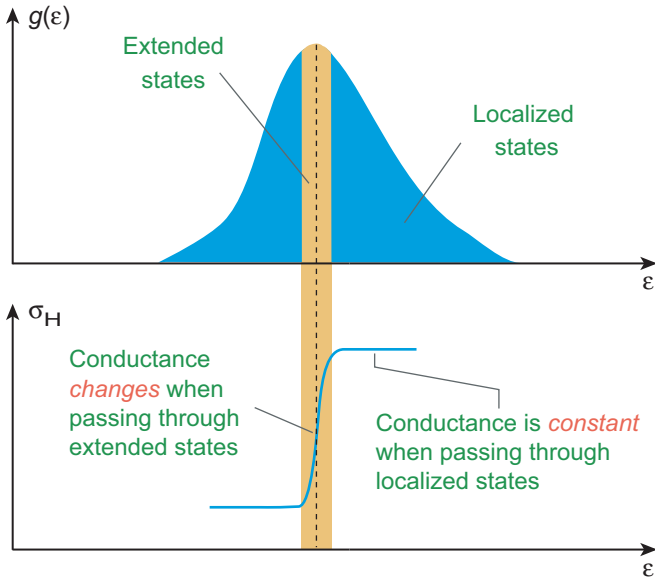


FIG. 13: Origin of Hall plateaus. Extended states (near the centroid of the peak) can carry current; localized states (in the wings of the peak) cannot. Thus conductance σ_H changes only when the energy ϵ is near the centroid of a Landau peak.

rent, even in the presence of impurities. More detailed studies than our simple discussion here confirm that in 2D systems current-carrying states near the energy of the unperturbed Landau level survive in the presence of a magnetic field, as illustrated schematically in Fig. 11(c).

Figure 11(c) explains the Hall plateaus of Fig. 9. Only states near the unperturbed Landau-level energy are delocalized and carry current, which causes R_H to jump discontinuously as the chemical potential is tuned through those states, but R_H remains constant as the chemical potential is tuned through localized states in the wings of the peak, as illustrated in Fig. 13. Thus the Hall plateaus of Fig. 9 correspond to ranges of magnetic field strength where the population of extended states is constant because the chemical potential is not near the center of the broadened Landau level. In effect, when the Fermi level of a disordered sample lies in a mobility gap between Landau levels n and $n + 1$, the transport characteristics mimic those of a pure sample with $\nu = n$. The plateaus in Fig. 9 are broad so the ranges of extended states must be narrow. Note that thermal excitation invalidates the preceding argument by scattering electrons between localized and extended states. Thus, quantum Hall experiments require very low temperatures, typically less than several kelvin.

2. Edge states and conduction

For an electron gas confined to two dimensions with a magnetic field orthogonal to the 2D plane, the classical Lorentz force causes electrons to move in circular (cyclotron) orbits. But as suggested by Fig. 14(a), no net current flows in the central region because the motion in one cyclotron orbit is offset

by the opposite motion in the adjacent cyclotron orbit. Thus, for the 2D electron gas in a magnetic field the *current vanishes in the bulk*. However, because of the confinement provided by the edge of the sample, states near the edge do not suffer this cancellation. Thus boundary electrons can “skip” along the edges and in confined 2D electron gases subject to a transverse magnetic field the *current is carried entirely by edge states*. This edge current is *chiral*: it is right-going along the upper edge and left-going along the lower edge in Fig. 14(a).

The preceding argument is basically correct, even though it is classical and Fig. 14 is just a cartoon. Solution of the Schrödinger equation with an edge confining potential leads to a delocalization of the wavefunction parallel to the edge and currents that are chiral because they flow in a single direction along each edge. Energy levels in the first few Landau levels are illustrated in Fig. 14(b) for a confining potential along one edge [12]. States are *gapped* by $\Delta E = \hbar\omega_c$ in the bulk, but are *gapless near the edge*, where energy between states tends to zero in the thermodynamic limit of many particles.

The *chiral nature of the edge states* protects their extended character, even if there is impurity scattering (Figs. 14 and 11). Normally, scattering between time-reversed states of opposite momentum in low-dimensional systems leads to Anderson localization and insulating character (Appendix B). But if all states are of a single chirality, scattering of a particle of definite chirality into a time-reversed state would change the chirality, which is forbidden if no states of opposite chirality are accessible. Thus, if tunneling across the device is negligible, impurity scattering is ineffective in localizing edge states.

3. Topology of the 2D Brillouin Zone

Let us now understand why quantization of conductance in integer multiples of e^2/h is so precise across varying experimental conditions, with samples having different geometries, electron densities, and impurity concentrations. The independent variables are momenta \mathbf{k} in the Brillouin zone (BZ), but these are turned into angular variables by the constraint $k(0) = k(2\pi)$ arising from the periodicity of Bloch waves on the lattice. Taking the Brillouin zone for a 1D crystal to range from $k = -\pi/a$ to $+\pi/a$ for lattice spacing a , the momentum dependence of a band energy can be displayed as in Fig. 15(a). But this doesn’t indicate clearly the *equivalence* of the right and left sides of the BZ at $k = \pm\pi/a$. We can improve things by identifying $k = +\pi/a$ and $k = -\pi/a$, which maps the 1D BZ from an interval on the real number line to a circle and the band-energy plot to a cylindrical, as in Fig. 15(b).

The Brillouin zone for a 2D crystal is displayed in Fig. 15(c). Periodicity in k_y identifies top and bottom edges, converting the square to a cylinder, and periodicity in k_x identifies left and right edges, joining the ends of the cylinder to form the 2-torus of Fig. 15(d). The toroidal geometry of the 2D Brillouin zone implies different classes of closed paths on the manifold, as illustrated in Fig. 15(e). Loops C and D can be shrunk continuously to a point (D is closed because of the periodic boundary condition); loops A and B cannot. Thus the loops A, B, and C lie in distinct topological sectors that cannot

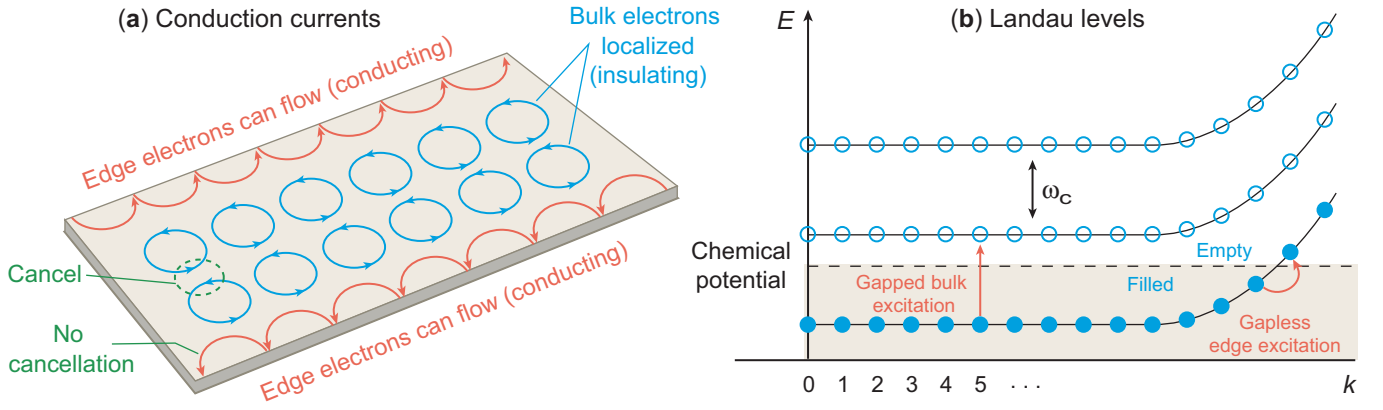


FIG. 14: (a) Conduction by edge states for a 2D electron gas in a perpendicular magnetic field. (b) First three Landau levels with a smooth confining potential on the right [12]. States in each level are labeled by k and indicated by circles. Filled states are shaded, empty states are unshaded, and the chemical potential is indicated by the dashed horizontal line. Bulk excitations are inhibited by a gap $\Delta E = \hbar\omega_c$ (where ω_c is the cyclotron frequency), but the gap for edge excitations tends to zero in the thermodynamic limit, implying gapless edge excitations.

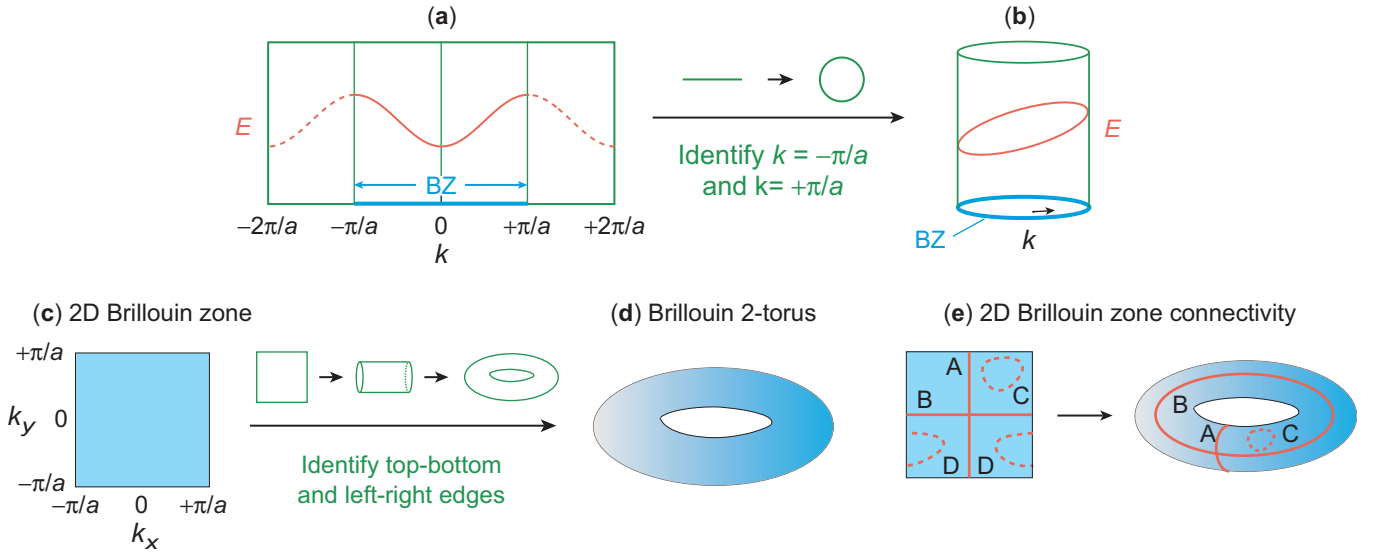


FIG. 15: Topology of the Brillouin zone. (a) Momentum dependence of a single band in a 1D crystal. (b) The periodicity of the crystal requires that $k = -\pi/a$ and $k = +\pi/a$ be identified, which converts the Brillouin zone to a circle and the band-energy plot to a cylinder. (c) The 2D Brillouin zone. (d) Because of crystal periodicity in the x and y directions, the top and bottom edges, as well as the left and right edges, of the 2D BZ must be identified, giving the geometry of a (closed) 2-torus for the Brillouin zone. (e) Different closed paths in the toroidal 2D Brillouin zone, implying non-trivial topology. Adapted from Refs. [4, 13].

be deformed continuously into one another. The non-trivial connectivity of the 2D Brillouin zone in Fig. 15 implies states characterized by topological quantum numbers that cannot be deformed smoothly into each other. Thus the Hilbert space for the integer quantum Hall effect is defined on a momentum-space torus and this leads to inequivalent topological sectors labeled by Chern numbers, as we now discuss.

4. Topological Protection of Hall Plateaus

Topological protection accounts for the remarkable flatness of the plateaus in Fig. 9, because it can be shown that, as a

consequence of the non-trivial topology of the Brillouin zone and the *Chern theorem* (Appendix C), the Hall conductance $\sigma_H = 1/R_H$ contributed by a single non-degenerate band is given by [14]

$$\sigma_H = \frac{e^2}{2\pi h} \int_S \Omega dS = C_1 \frac{e^2}{h}, \quad (70)$$

where e is electrical charge, h is Planck's constant, S is a closed surface in the manifold of quantum states, Ω is local Berry curvature in that manifold, and C_1 is a topological Chern number that takes integer values. Thus the exquisite flatness of the plateaus for R_H in Fig. 9 follows from topological protection within a particular quantum topological phase ensured

by Eq. (70), and the vertical jumps between plateaus correspond to quantum phase transitions between topological states characterized by different Chern numbers (see Appendix C).

5. Bulk–Boundary Correspondence

In the quantum Hall effect, and more generally in topological matter (material characterized by topological quantum numbers), it is important to distinguish the *bulk* (interior) of a sample and the *boundary* (surface in 3D, edges in 2D, and ends in 1D). In the quantum Hall effect the strong magnetic field localizes electrons in the bulk, while forcing boundary electrons into delocalized chiral edge states [Fig. 14(a)]. Thus the bulk states are insulating but the boundary states are conducting (metallic). This relationship between the bulk states and the boundary states for the IQHE is an example of *bulk–boundary correspondence*, which is a characteristic feature of topological matter and implies that topological quantum numbers characterizing the bulk also predict boundary properties.

6. Incompressible States

When N electrons exactly fill an integer number ν of Landau levels there is an energy gap $\hbar\omega_c$ between filled and empty states. Now a decrease in the area A of the system at constant magnetic field and electron density will decrease the number of flux quanta N_ϕ piercing the sample. By Eq. (66), this reduces the capacity of the Landau levels and requires that electrons be promoted to higher Landau levels. There is an energy cost $\hbar\omega_c$ for each promoted electron, so the system resists compression and is said to be *incompressible*. Thus, a quantum Hall system is an *incompressible quantum fluid*.

C. Summary: Integer Quantum Hall Effect

In summary, for the integer quantum Hall effect the crucial points are (1) Landau-level quantization in the magnetic field, (2) a random scattering potential caused by impurities, and that (3) each Landau level contributes a fixed value to the Hall conductance as a consequence of mobility gaps created by the impurity scattering. Thus conductance is quantized because effectively it counts the number of filled Landau levels. The robustness of this quantization derives from the non-trivial Brillouin zone topology and the Chern theorem, as described in Sections VII B 3 and VII B 4, and Appendix C.

VIII. THE FRACTIONAL QUANTUM HALL EFFECT

Tsui, Stormer, and Gossard [15] discovered the fractional quantum Hall effect (FQHE) in 1982 when they found that at higher magnetic fields and lower temperatures the quantum Hall effect can occur for the fractional value of $\frac{1}{3}(e^2/h)$, corresponding to a filling fraction $\nu = 1/3$, unlike the integer quantum Hall effect (IQHE), which occurs only at integer multiples

of e^2/h . Laughlin [16] proposed that the FQHE corresponds to a new state of matter formed by strong electron–electron correlations within a single Landau level. It was shown in later work that the FQHE could occur for whole series of fractional values $\frac{1}{m}(e^2/h)$, with m an even or odd integer.

A. Properties of the fractional quantum Hall state

Let us consider a theoretical understanding of this fractional quantum Hall effect. First, note that fractional filling factors in themselves are not unusual. The conductance is expected to be $\nu e^2/h$ if we add non-interacting electrons to the lowest Landau level up to a fractional occupation ν . But in the absence of interactions there will be no gap at the Fermi surface and adding electrons will cost almost no energy, destroying the plateau structure of the Hall resistance in Fig. 9. If we assume interacting electrons instead, they will scatter into empty Landau states, leading to a finite longitudinal resistance, which contradicts experiments. Thus, explanation of the fractional quantum Hall effect requires a ground state that

1. has a *fractionally-filled Landau level* and
2. has an *energy gap* with respect to excitation at that fractional filling.

As noted above, a state with an energy gap resists compression, so we may also term such a state *incompressible*. Ground states with a gap and small resistance were known when the fractional quantum Hall effect was discovered, but none had the right properties to explain the FQHE. A fundamentally new kind of state is required for which strong electronic correlations in a partially-filled Landau level produce a ground state corresponding to an incompressible electronic liquid, with a fractional filling factor and an energy gap for all excitations.

Both the IQHE and the FQHE result from quantizing electronic motion for 2D electron gases in strong magnetic fields, but their mechanisms are fundamentally different. The IQHE involves weakly-interacting electrons and depends on impurity scattering for its plateau structure indicating quantization of conductance, but the FQHE requires very pure samples because it is a consequence of strong Coulomb interactions between the degenerate electrons in Landau levels. Strongly-correlated electrons in a magnetic field represent an inherently difficult problem; it was solved only by an educated guess for the form of the wavefunction. The difficulty of solving this problem derives from some features of the FQHE that distinguish it from most other problems in many-body physics [17].

(1) It is generally assumed that the FQHE corresponds to partial filling of the lowest Landau level (LLL). Absent interactions there are many ways to fill the LLL partially that give the same energy. What principle should guide us to choose the linear combination of these states that will define the physical ground state when the interactions are turned on?

(2) In the very high magnetic fields that characterize FQHE experiments the problem reduces approximately to Coulomb interactions between electrons in the lowest Landau level. The

strength of the Coulomb interaction just sets an energy scale, so the fractional quantum Hall problem contains no obvious parameters to adjust in order to gain intuition about the physics responsible for the solution.

(3) In many-body physics it is common to view an emergent state as resulting from an instability of a parent “normal state” that would be favored in the absence of interactions. But turning off the interactions for the FQHE state does not lead to a normal state that is the obvious parent of the FQHE state.

For these reasons the solution of the FQHE problem cannot be obtained by successive small steps or other standard approximations and we are reduced to *making an educated guess* for a wavefunction that leads to the observed FQHE. The best such educated guess to date is the *Laughlin wavefunction*.

B. The Laughlin wavefunction

Let us consider a wavefunction to describe the fractional quantum Hall state, guided by the discussion in Phillips [9]. We assume the magnetic field to be large and as a first approximation ignore the Coulomb interactions between electrons, and assume the electron spins to be completely polarized by the field and drop the corresponding (constant) spin term. This gives again the Hamiltonian (54), but now let’s work in the symmetric gauge defined in Eq. (56b). It is convenient to introduce the complex coordinate $z_i = x_i + iy_i = re^{i\phi}$ for the i th particle, in which case the solution of the Schrödinger equation in symmetric gauge gives the N -body wavefunctions

$$\Psi_N = \prod_{j<k}^N f(z_j - z_k) e^{-\sum_{j=1}^N |z_j|^2 / 4\Lambda^2}, \quad (71)$$

where $f(z_j, z_k)$ is a polynomial in the electron coordinates z_i and Λ is the magnetic length defined in Eq. (59). Analysis of this wavefunction for two and three electrons led Laughlin to propose what is now termed the *Laughlin wavefunction*,

$$\Psi_{1/m} = \prod_{j<k}^N (z_j - z_k)^m e^{-\sum_{j=1}^N |z_j|^2 / 4\Lambda^2}, \quad (72)$$

which specifies the FQHE states at filling factors $\nu = 1/m$, with the integer m required to be odd to ensure antisymmetry of the fermionic wavefunction. Thus, the first FQHE state discovered with filling factor $\nu = \frac{1}{3}$ corresponds to the wavefunction (72) with $m = 3$.

The exponent m was introduced originally as a variational parameter but $\Psi_{1/m}$ is an eigenstate of the angular momentum operator with angular momentum M given by

$$M = \frac{1}{2}N(N-1)m \quad (73)$$

for N particles. Thus m is related directly to the angular momentum content of the Laughlin wavefunction (72), which may be viewed as a superposition of states from the lowest Landau level having the same angular momentum.

The Laughlin wavefunction given by Eq. (72) has several features that make it a plausible candidate for a FQHE wavefunction.

1. It minimizes the kinetic energy by placing all electrons in the lowest Landau level.
2. It vanishes if the coordinates of any two electrons are the same because of the $(z_k - z_\ell)^m$ factor, which is desirable for a wavefunction in a strongly-correlated system with repulsive interactions because it reduces the total potential energy.
3. It is antisymmetric under the exchange of any pair of particles if m is odd.
4. It can be shown to describe a circular droplet with $\nu = \frac{1}{3}$ and an approximately uniform density.
5. Simple models and numerical simulations suggest that it describes an incompressible state that has an energy gap to all excitations.

The wavefunction (72) is now accepted broadly as a valid description of the first $\nu = \frac{1}{3}$ FQHE state, and by inference of other fractional quantum Hall states discovered later.

The Laughlin wavefunction provides only limited fundamental insight into the underlying microscopic physics responsible for the FQHE state since it is in essence a highly-educated guess at the many-body wavefunction (similar in spirit to the “guess” by Bardeen, Cooper, and Schrieffer for the form of the BCS wavefunction that led to comprehensive understanding of the superconducting problem). However, the influence of the Laughlin wavefunction on understanding the fractional quantum Hall effect has been seminal.

IX. GRAPHENE IN STRONG MAGNETIC FIELDS

As we have seen, rather remarkable quantum Hall physics is observed when a cold 2D electron gas is subject to a strong magnetic field. Since a single layer of graphene is the ideal 2D material, it is of interest whether similar quantum Hall effects could be observed in graphene. To begin addressing that question we consider in this section the quantum states of electrons confined in 2D and governed by a massless Dirac single-particle Hamiltonian, with a strong magnetic field placed perpendicular to the 2D plane. Our discussion will have some overlap with the earlier treatment of a similar system with electrons governed by a Schrödinger equation, but there will be substantial differences associated with the Dirac rather than Schrödinger physics appropriate for graphene. We shall use the review by Goerbig [2] for guidance, and often use $c = 1$ and $\hbar = 1$ units.

A. Quantization of Dirac Landau levels

By the usual minimal substitution, electromagnetism may be included in a Hamiltonian by replacing the canonical momen-

tum \mathbf{p} with the gauge-invariant kinetic momentum $\mathbf{\Pi}$,

$$\mathbf{\Pi} = \mathbf{p} + e\mathbf{A}(\mathbf{r}), \quad (74)$$

where the magnetic field \mathbf{B} is related to the vector potential \mathbf{A} by

$$\mathbf{B} = \nabla \times \mathbf{A}. \quad (75)$$

From Eq. (40), to lowest order in $|\mathbf{q}|a$ the Hamiltonian with the minimal substitution is

$$H = \xi v_F (\Pi_x \sigma^x + \Pi_y \sigma^y). \quad (76)$$

The electron energies will also split into two branches according to the Zeeman energy in the magnetic field $\Delta_z = g\mu_B B$, where $g \sim 2$ for graphene. In this initial discussion we ignore Δ_z , but will return to the role of spin later.

The canonical method may be used to quantize this system. In the absence of the vector potential the coordinates and momenta would obey the commutation relations

$$\begin{aligned} [x, p_x] &= [y, p_y] = i\hbar \\ [x, y] &= [p_x, p_y] = [x, p_y] = [y, p_x] = 0. \end{aligned} \quad (77)$$

From Eqs. (74) and (77), the commutator of Π_x and Π_y is [2]

$$[\Pi_x, \Pi_y] = -ie\hbar \left(\frac{\partial A_y}{\partial x} - \frac{\partial A_x}{\partial y} \right). \quad (78)$$

But the magnetic field is assumed aligned along the z -axis, $\mathbf{B}(B_x, B_y, B_z) = (0, 0, B)$ and from Eq. (75),

$$\frac{\partial A_y}{\partial x} - \frac{\partial A_x}{\partial y} = B_z \equiv B,$$

and therefore Eq. (78) becomes

$$[\Pi_x, \Pi_y] = -ie\hbar B = -i\hbar^2 \frac{eB}{\hbar} = -i \frac{\hbar^2}{\Lambda^2}, \quad (79)$$

with the magnetic length Λ introduced in Eq. (59) given by $\Lambda = \sqrt{\hbar/eB}$ in $c = 1$ units. It will be convenient to introduce the raising and lowering operators

$$a^\dagger = \frac{\Lambda}{\sqrt{2}\hbar} (\Pi_x + i\Pi_y) \quad a = \frac{\Lambda}{\sqrt{2}\hbar} (\Pi_x - i\Pi_y), \quad (80)$$

where the normalization factor is chosen so that

$$[a, a^\dagger] = 1. \quad (81)$$

Adding and subtracting Eqs. (80) gives the inverse relations

$$\Pi_x = \frac{\hbar}{\sqrt{2}\Lambda} (a^\dagger + a) \quad \Pi_y = \frac{\hbar}{\sqrt{2}\Lambda i} (a^\dagger - a), \quad (82)$$

and inserting this result into the Hamiltonian (76) gives

$$\begin{aligned} H &= \xi v_F (\Pi_x \sigma^x + \Pi_y \sigma^y) \\ &= \xi v_F \left[\Pi_x \begin{pmatrix} 0 & 1 \\ 1 & 0 \end{pmatrix} + \Pi_y \begin{pmatrix} 0 & -i \\ i & 0 \end{pmatrix} \right] \\ &= \xi v_F \begin{pmatrix} 0 & \Pi_x - i\Pi_y \\ \Pi_x + i\Pi_y & 0 \end{pmatrix} \\ &= \frac{\sqrt{2}\hbar}{\Lambda} \xi v_F \begin{pmatrix} 0 & a \\ a^\dagger & 0 \end{pmatrix} \\ &= \hbar \xi \omega \begin{pmatrix} 0 & a \\ a^\dagger & 0 \end{pmatrix}, \end{aligned} \quad (83)$$

where Eqs. (80) were used and $\omega \equiv \sqrt{2}v_F/\Lambda$ is the analog of the cyclotron frequency (48) for the present relativistic problem. Introducing the 2-component spinor

$$\psi_n = \begin{pmatrix} u_n \\ v_n \end{pmatrix}, \quad (84)$$

we must then solve the eigenvalue equation $H\psi_n = \varepsilon_n \psi_n$, which takes the form

$$\hbar \xi \omega \begin{pmatrix} 0 & a \\ a^\dagger & 0 \end{pmatrix} \begin{pmatrix} u_n \\ v_n \end{pmatrix} = \varepsilon_n \begin{pmatrix} u_n \\ v_n \end{pmatrix}, \quad (85)$$

implying the simultaneous equations

$$\hbar \xi \omega a v_n = \varepsilon_n u_n, \quad (86a)$$

$$\hbar \xi \omega a^\dagger u_n = \varepsilon_n v_n. \quad (86b)$$

Solving Eq. (86a) for u_n and substituting into Eq. (86b) gives $a^\dagger a v_n = (\varepsilon_n/\hbar\omega)^2 v_n$. But because of Eq. (81) this is just the usual harmonic oscillator number equation $a^\dagger a |\psi\rangle = n |\psi\rangle$ with $n = (\varepsilon_n/\hbar\omega)^2$, and up to numerical factors the state $|v_n\rangle$ may be identified with a number eigenstate $|n\rangle$. Solving for ε_n in terms of n gives $\varepsilon_n = \pm \hbar\omega\sqrt{n}$, which may be written

$$\varepsilon_n = \lambda \hbar\omega\sqrt{n} = \lambda \frac{\hbar v_F}{\Lambda} \sqrt{2n} \propto \lambda \sqrt{nB}, \quad (87)$$

where the quantum number $\lambda = \pm 1$ has been introduced to distinguish the positive and negative square roots; it plays the same role as the band index in the zero-field case [see Eq. (12)], corresponding to the graphene two-fold valley degeneracy for $B = 0$. Thus, the energy disperses as $\varepsilon_n \sim \pm (nB)^{1/2}$ with magnetic field strength, as illustrated in Fig. 16(a).

From Eq. (87) and Fig. 16(a) the $n = 0$ state is not split into positive and negative branches, as is the case for all other values of n . From Eq. (86a) we have $u_n \propto a v_n \sim a |n\rangle \sim |n-1\rangle$, because of the usual oscillator operator requirements that

$$\begin{aligned} a^\dagger |n\rangle &= \sqrt{n+1} |n+1\rangle & a |n > 0\rangle &= \sqrt{n} |n-1\rangle \\ a |n = 0\rangle &= 0. \end{aligned}$$

Thus, for $n = 0$ the eigenspinor (84) has only a single component,

$$\psi_n = \begin{pmatrix} u_n \\ v_n \end{pmatrix} = \begin{pmatrix} 0 \\ |n = 0\rangle \end{pmatrix}, \quad (88)$$

with the non-zero component corresponding to the B sublattice in the K valley ($\xi = +1$) and the A sublattice in the K' valley ($\xi = -1$). This implies that the valley pseudospin and the sublattice pseudospin coincide for $n = 0$. For all other values of n , there are two spinor components and positive and negative energy solutions.

B. Degeneracy of Landau levels

Just as for the non-relativistic case, Landau levels for relativistic fermions in a strong magnetic field become *highly degenerate*. In both the non-relativistic and relativistic cases the

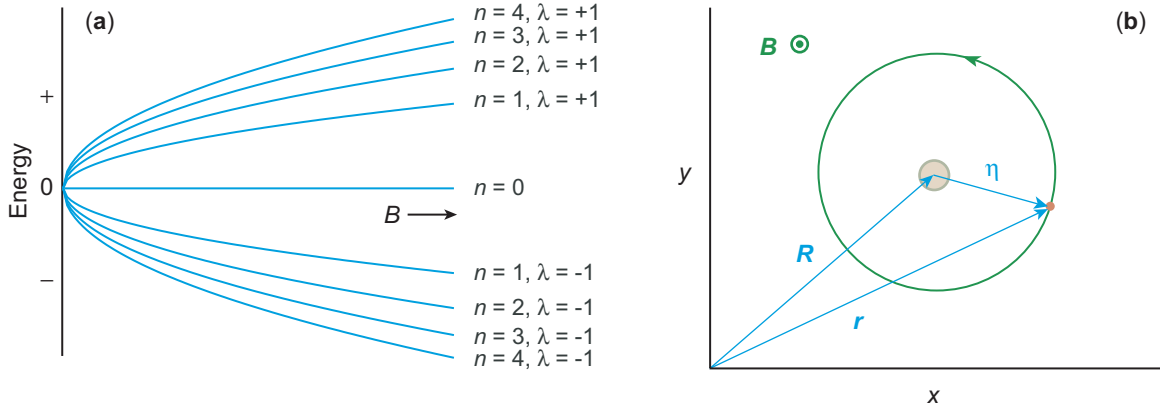


FIG. 16: (a) Relativistic Landau energy levels as a function of magnetic field strength B . (b) Guiding center coordinates \mathbf{R} and cyclotron coordinates \mathbf{r} . Classically the guiding center coordinates define the center of the cyclotron orbit and the cyclotron coordinates describe the motion of the electron relative to the guiding center. The shaded area in the center of the circle represents the uncertainty in the position of the guiding center implied by Eq. (95). Figure adapted from Ref. [2].

degeneracy N_B is equal to the number of flux quanta threading the 2D electron gas,

$$N_B = \frac{B}{(h/e)} S, \quad (89)$$

where S is the area of the 2D sample, BS is the total flux, and h/e is the flux quantum (in $c = 1$ units); see Eq. (65) and the discussion following it. Let's investigate this degeneracy in more detail for the relativistic case appropriate for graphene.

It is convenient to separate the relativistic cyclotron motion of the electrons into *guiding center coordinates* $\mathbf{R} = (X, Y)$ that commute with the Hamiltonian, and relative coordinates termed *cyclotron variables* $\boldsymbol{\eta} = (\eta_1, \eta_2)$, according to

$$\mathbf{r} = \mathbf{R} + \boldsymbol{\eta}, \quad (90)$$

as illustrated in Fig. 16(b). Classically, the guiding center coordinates represent the center of the cyclotron motion for an electron and the cyclotron coordinates describe the time-dependent (dynamical) component of motion. From Fig. 16(b) the cyclotron variable $\boldsymbol{\eta}$ is orthogonal to the electron velocity and hence is related to the kinetic momentum $\boldsymbol{\Pi}$ defined in Eq. (74) by

$$\eta_x = \frac{\Pi_y}{eB} \quad \eta_y = -\frac{\Pi_x}{eB}. \quad (91)$$

From this relation and Eq. (79), the commutator of the cyclotron variables is

$$[\eta_x, \eta_y] = \frac{[\Pi_x, \Pi_y]}{(eB)^2} = -i\Lambda^2. \quad (92)$$

This can be used to find the commutation relation for the guiding center coordinates (X, Y) . From Eq. (90) with $\mathbf{r} = (x, y)$ we have $x = X + \eta_x$ and $y = Y + \eta_y$, and since $[x, y] = 0$,

$$\begin{aligned} [x, y] &= [X + \eta_x, Y + \eta_y] \\ &= [X, Y] + [X, \eta_y] + [\eta_x, Y] + [\eta_x, \eta_y] = 0. \end{aligned}$$

Assuming the guiding center and cyclotron coordinates to commute, this yields

$$[X, Y] = -[\eta_x, \eta_y] = i\Lambda^2, \quad (93)$$

where Eq. (92) was used. Thus X and Y are conjugate variables and Eq. (93) is an uncertainty relation associated with simultaneous specification of X and Y . Introduce

$$b = \frac{1}{\sqrt{2}\Lambda}(X + iY) \quad b^\dagger = \frac{1}{\sqrt{2}\Lambda}(X - iY), \quad (94)$$

which satisfy the commutation relation $[b, b^\dagger] = 1$ and commute with the Hamiltonian (since X and Y do). Because of this commutation relation this is a second set of harmonic-oscillator operators, so we expect $b^\dagger b$ to be a number operator with $b^\dagger b |m_k\rangle = m_k |m_k\rangle$, where the integer $m_k \geq 0$ (separate from n) counts the states created by operating repeatedly on the vacuum with b^\dagger . Since b and b^\dagger commute with the Hamiltonian, m_k is an additional quantum number that labels electronic states in the magnetic field and we conclude that the states on a given branch of Fig. 16(a) may be labeled by the quantum numbers n and m_k .

As noted above, Eq. (93) is an uncertainty relation indicating that we cannot measure the X and Y coordinates of the guiding center for an electron simultaneously with arbitrary precision. The location of the guiding center is found to be uncertain according to [2]

$$\Delta X \Delta Y = 2\pi\Lambda^2, \quad (95)$$

which is represented by the shaded area in the center of Fig. 16(b). Let the total area of the 2D gas be S and introduce the flux density n_B measured in units of the flux quantum h/e through

$$n_B = \frac{N_B}{S} = \frac{B}{(h/e)}, \quad (96)$$

where Eq. (89) was used. The number of quantum electronic states found in the area S is

$$N_B = \frac{S}{\Delta X \Delta Y} = \frac{S}{2\pi\Lambda^2} = n_B S, \quad (97)$$

and so

$$n_B = \frac{B}{(h/e)} = \frac{1}{2\pi\Lambda^2}. \quad (98)$$

Thus, the flux density and the density of possible electronic states in a magnetic field coincide for the 2D gas. The filling factor ν can then be defined by the ratio of the electron number density n_e and the flux density n_B ,

$$\nu \equiv \frac{n_e}{n_B} = \frac{\hbar n_e}{eB}. \quad (99)$$

This treatment assumes the only degeneracies to be those of the Landau levels for massless Dirac electrons. In the following sections we shall see how this is modified by additional degeneracies associated with sublattice and valley degrees of freedom in graphene.

X. QUANTUM HALL EFFECTS IN GRAPHENE

The quantum Hall effect occurs for 2D electron gases in strong magnetic fields. Because of degrees of freedom associated with the honeycomb lattice structure, we may expect that quantum Hall effects in graphene could be richer than those in the usual 2D electron gas. From the preceding discussion we may expect that analogs of the integer quantum Hall states might occur for weakly-interacting electrons in graphene, but the fractional quantum Hall state can be produced only by strongly-correlated electrons. Most of the low-energy properties of graphene are described well assuming weakly interacting massless Dirac fermions in two dimensions, but we may ask whether there are particular situations in which monolayer graphene might exhibit strong electron–electron correlations. The relative effectiveness of correlations are expected to depend on (1) the intrinsic strength of the electronic interactions, and (2) the density of states at the Fermi surface.

A. Strength of correlations in graphene

For the Coulomb gas of electrons characterizing a layer of graphene, the average interaction energy at a characteristic length scale k_F^{-1} is $E_{\text{int}} \sim e^2 k_F / \epsilon$, where e is the electronic charge, ϵ is the effective dielectric constant of the environment, and k_F is the Fermi momentum. The average kinetic energy at the same length scale is $E_{\text{kin}} \sim \hbar \epsilon v_F$, where v_F is the Fermi velocity. The ratio of interaction energy and kinetic energy at this characteristic length scale defines a coupling constant for graphene[2, 18],

$$\alpha_G \equiv \frac{E_{\text{int}}}{E_{\text{kin}}} = \frac{e^2 k_F / \epsilon}{\hbar \epsilon v_F k_F} = \frac{e^2}{\hbar \epsilon v_F}. \quad (100)$$

This has the same form as the fine-structure constant α of quantum electrodynamics (QED) if the speed of light c is exchanged for the Fermi velocity v_F . The “fine structure constant” α_G of graphene is $c/v_F \sim 300$ times that for QED ($\alpha \sim 1/137$) at comparable energies, implying a relatively large Coulomb interaction. However, the low-energy excitations in graphene obey an approximately linear dispersion relationship and in the undoped compound the density of states vanishes as the Fermi surface [at the apex of the Dirac cones in Fig. 4(b)] is approached. This low density of states near the Fermi surface suppresses electron–electron correlations and much of low-energy physics for monolayer graphene is dominated by weakly-correlated particles. If we wish to search for strongly-correlated physics in graphene, it is necessary to find circumstances that correspond to increased level density near the Fermi surface [18].

One way to attain higher local level density is to place a strong magnetic field B perpendicular to the sample. Then the electronic levels become quantized into Landau levels that are highly degenerate, with a strongly-peaked density of states

$$\rho(E) = g n_B \sum_n f(E - E_n), \quad (101)$$

where g is a degeneracy factor for internal degrees of freedom (in graphene, $g = 4$ because of the four-fold spin–valley degeneracy), $n_B = eB/h$ is the flux density in units of the flux quantum h/e , and $f(E - E_n)$ is strongly peaked, tending to a δ -function in the clean limit. In this limit, each LL may then be approximated as an infinitely flat (dispersionless, because kinetic energy is negligible) energy band in which the state density grows linearly with the magnetic field strength [18]. The effect of Fermi surface position relative to the Landau levels may be studied by fixing the magnetic field and sweeping a gate voltage applied to the sample, or by fixing the gate voltage and sweeping the magnetic field.

B. The graphene integer quantum Hall effect

Electron spin has largely been ignored in the discussion of the quantum Hall effect to this point, but if it is not neglected IQHE conditions are satisfied when both spin branches (split by the Zeeman term) of the last Landau level (LLL) are completely filled. Thus $\nu_{\text{IQHE}} = 2n$, where n is an integer and filling factors are even integers in the usual IQHE. The graphene IQHE is expected to resemble the usual IQHE, except for two key points.

1. In addition to the 2-fold spin degeneracy (if Zeeman splitting is neglected), there is a 2-fold K and K' valley degeneracy for graphene. Thus the filling factor changes in steps of four between plateaus in the Hall resistance for graphene.
2. For graphene the filling factor

$$\nu = \frac{n_e}{n_B} = \frac{\hbar n_e}{eB} \quad (102)$$

vanishes at the Dirac point for particle–hole symmetric half filling of the graphene lattice, because the electron density n_e tends to zero at the Dirac point. Therefore, absent a Zeeman effect or electron correlations, one expects no integer quantum Hall effect in graphene for $\nu = 0$.

Thus the signature of a graphene IQHE is Hall resistance quantization for filling factors

$$\nu = \pm 4 \left(n + \frac{1}{2} \right) = \pm(4n + 2) = \pm 2, \pm 6, \pm 10, \dots \quad (103)$$

where n is an integer, the factor of 4 is because of the 4-fold valley and spin degeneracy, and the added $\frac{1}{2}$ (not present in non-relativistic 2D systems) is because of the special status of the $n = 0$ state for massless Dirac fermions in graphene.

Evidence for an integer quantum Hall effect in graphene was reported in Refs. [5, 19], and is illustrated in Fig. 17(a). These experiments confirmed the predicted anomalous spacing of Eq. (103) for a graphene integer quantum Hall effect. Later experiments observed fragile IQHE states at filling factors 0, ± 1 , ± 4 , that are thought to be caused by Zeeman splitting and electron interactions breaking degeneracies of the $n = 0$ Landau level.

C. The effect of strong correlations in graphene

Graphene is a unique environment because of two aspects not found in non-relativistic quantum Hall experiments: (1) its charge carriers are effectively massless chiral fermions, and (2) the symmetries associated with the four-fold spin and valley degrees of freedom introduce new features for states and correlations. As we have seen in Section X A, low-energy excitations in normal monolayer graphene occur in regions of reduced electron density, which disfavors electron correlations. But by applying a strong magnetic field the resulting Landau quantization leads to a bunching of levels into regions of high degeneracy, giving conditions more amenable to the development of strong electronic correlations if the Fermi surface lies in one of those regions.

Landau levels (LL) become strongly correlated when inter-LL excitations may be neglected and the low-energy excitations involve only the same level. Then the kinetic energy is a constant that can be ignored. This limit of strong electronic correlations leads to two important physical effects [18].

1. The 4-fold approximate spin–valley degeneracy of the graphene Landau levels leads to *quantum Hall ferromagnetic states*.
2. The strong correlations can lead to a *fractional quantum Hall effects (FQHE)*.

Because of the approximate 4-fold degeneracy, these effects can be discussed within the framework of an SU(4) symmetry that we shall elaborate in Section XI. Let us now consider the fractional quantum Hall effect in graphene, which is a clear signal of a strongly-correlated state.

D. The graphene fractional quantum Hall effect

The fractional quantum Hall effect in graphene can be observed only in samples extremely free of impurities. Strong electron–electron correlations in general, and the FQHE in particular, were initially very difficult to observe in graphene because of samples that were not sufficiently clean to suppress impurity scattering. The fractional quantum Hall effect in graphene was discovered in 2009 [20, 22], when it became possible to make measurements on suspended graphene sheets, thus avoiding impurities and scattering associated with substrate contact. Evidence for a fractional quantum Hall effect in graphene from those experiments is presented in Fig. 17(b)–(c). A plateau labeled A at a density dependent on the magnetic field emerges for $B > 11$ T. The inset to Fig. 17(c) plots this feature as a function of filling factor. The different traces for different magnetic field strength collapse into a single universal feature, suggesting that A be identified with a $\nu = \frac{1}{3}$ fractional quantum Hall state.

In Fig. 17(d), further evidence for incompressible states at fractional filling in graphene is shown [21]. The inverse compressibility is defined by $\kappa^{-1} = d\mu/dn$, where n is the local carrier density and μ is the chemical potential. In Fig. 17(d) a scanning single-electron transistor was used to measure the local incompressibility of electrons in a suspended graphene sample and the derivative $d\mu/dn$ was plotted versus density and magnetic field strength. High incompressibility is indicated by vertical red bands. Localized states are broad and curve as the magnetic field is varied but the fractional quantum Hall states are narrow and vertical, and are labeled by fractional filling numbers. The states that are observed follow the standard sequence for filling factors $\nu = 0 - 1$, but only even-numerator fractions are seen for $\nu = 1 - 2$. It is thought that these sequences and the corresponding energy gaps for the incompressible states reflect the interplay of strong electron correlations and the characteristic symmetries of graphene that will be discussed further in Section XI [21].

XI. SU(4) QUANTUM HALL FERROMAGNETISM

Graphene FQHE states can exhibit various symmetries because of possible degeneracies associated with the pseudospin and valley degrees of freedom. In the normal two-dimensional electron gas (2DEG) produced in semiconductor devices the Landau levels (LL) can contain eB/h states, where e is the electronic charge, B is the magnetic field strength, and h is Planck’s constant. In graphene, there is an additional 4-fold degeneracy associated with the spin and valley degrees of freedom. It is common to unite these four degrees of freedom (often termed *flavors*) in terms of an SU(4) symmetry called *quantum Hall ferromagnetism (QHF)*.

A. Degeneracies and filling of Landau levels

Single-particle states within a Landau level may be labeled by quantum numbers (n, m_k) , with n indicating the Lan-

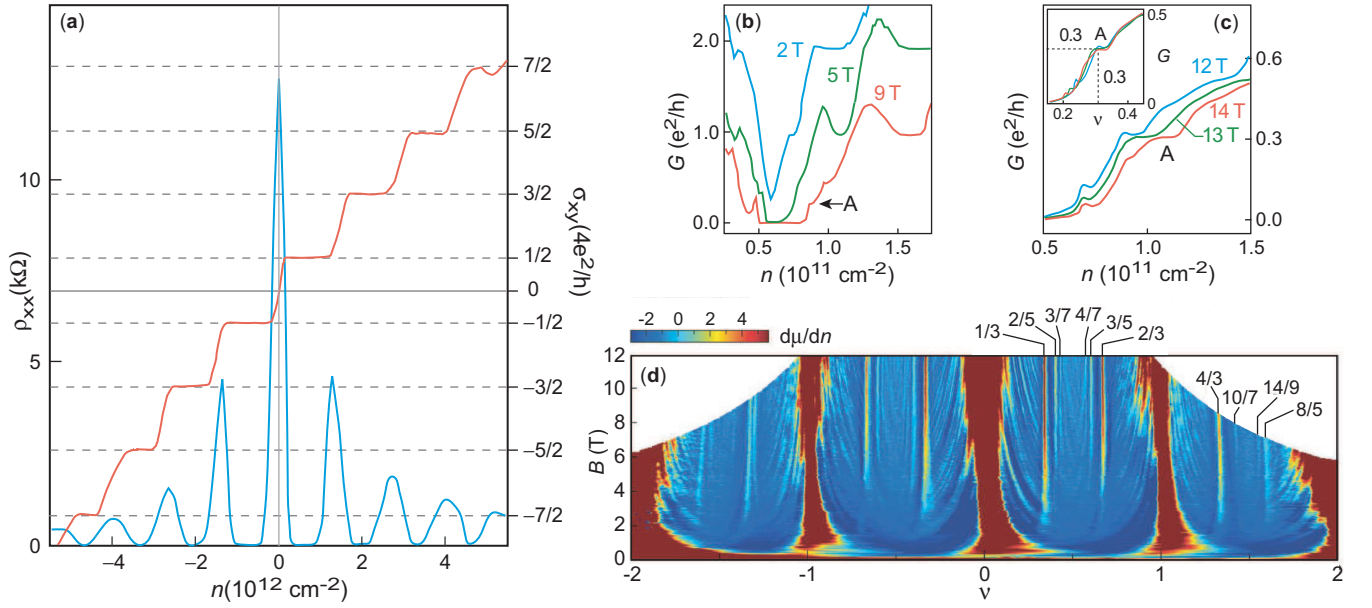


FIG. 17: Evidence for integer and fractional quantum Hall effects in monolayer graphene [5, 19–21]. (a) Integer quantum Hall effect [5]. The filling factors are anomalous, as described in the text. (b) Fractional quantum Hall effect; lower fields [20]. (c) Fractional quantum Hall effect; higher fields [20]. The plateau labeled A has features expected for a $\nu = 1/3$ fractional quantum Hall state. (d) Incompressible states with fractional filling numbers (marked), as a function of magnetic field B and carrier density n [21]; contours of $d\mu/dn$ in units of 10^{-10} meV cm^2 are displayed.

dau level and m_k labeling degenerate states associated with that level. These Landau states (n, m_k) hold a maximum of $2\Omega_k = BS/(h/e)$ electrons if spin and valley degrees of freedom are neglected, where B is the strength of the magnetic field, S is the area of the two-dimensional sample, and $h/e = 4.136 \times 10^{-15}$ Wb is the magnetic flux quantum. But the 4-fold degenerate internal $|\text{spin}\rangle \otimes |\text{isospin}\rangle$ space for graphene implies that there are four copies of each Landau level (n, m_k) and the total electron degeneracy 2Ω for graphene is given by

$$2\Omega = 4(2\Omega_k) = \frac{4BS}{(h/e)}. \quad (104)$$

For a single Landau level the *fractional occupation* f of the single Landau level is

$$f \equiv \frac{n}{2\Omega} = \frac{N}{\Omega}, \quad (105)$$

where n is the electron number and $N = \frac{1}{2}n$ is the electron pair number. Note that the fractional occupation f and the quantum Hall filling factor ν defined in Eq. (67) are related by [23]

$$\nu = 4 \left(f - \frac{1}{2} \right). \quad (106)$$

For the ground state of undoped graphene the $n = 0$ Landau level located at the Fermi surface is half filled and the electron number n_{gs} is then

$$n_{\text{gs}} = \Omega = \frac{2BS}{(h/e)}. \quad (107)$$

These degeneracies and occupation numbers are standard results for relativistic Landau electrons in a 2D electron gas, but now modified by the intrinsic graphene degrees of freedom.

B. SU(4) quantum Hall states in graphene

The graphene honeycomb lattice is bipartite, corresponding to the interlocking A and B sublattices shown in Fig. 18. The A and B sublattices are related by inversion, as illustrated in Fig. 5(a). The $n = 0$ LL is located exactly at the Dirac point corresponding to $\varepsilon = 0$. For low-energy excitations in each K or K' valley the inter-valley tunneling may be ignored and the wavefunctions in the valley reside entirely on either the A or B sublattice, as in Fig. 19. For the $n = 0$ LL, the valley isospin (labeling whether the electron is in a K or K' valley) is identical to the sublattice pseudospin (labeling whether the electron is on the A or B sublattice). Thus, this is analogous to a Néel antiferromagnetic state with spins on two different sublattices, with a Néel order defined by the difference in spins on the A and B sublattices.

1. Effective Hamiltonian

The two largest energy scales for monolayer graphene in a strong magnetic field are

1. the Landau-level separation, $H_\Delta = \sqrt{2}\hbar v_F/\Lambda$, and
2. the Coulomb energy H_C .

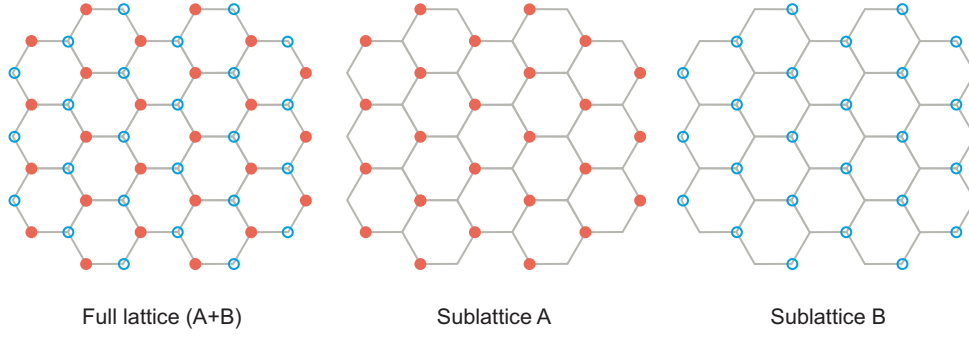


FIG. 18: The full bipartite lattice for graphene and the A (solid red circles) and B (open blue circles) sublattices.

The separation of Landau levels is typically several times larger than the Coulomb energy, which is in turn considerably larger than any other terms in the interaction. Therefore, we adopt a strategy of ignoring excitations between Landau levels and projecting onto the $n = 0$ LL. Such an approximation gives the correct qualitative physics, which will be sufficient for our discussion. Within this single LL we assume that the Hamiltonian is dominated by an SU(4)-symmetric, long-range Coulomb interaction, with shorter-range spin and valley isospin interactions originating in electron–electron interactions and electron–phonon interactions that break SU(4) symmetry. We shall use an approximate graphene Hamiltonian for the $n = 0$ Landau level that was proposed in Ref. [24] and employed in Ref. [25],

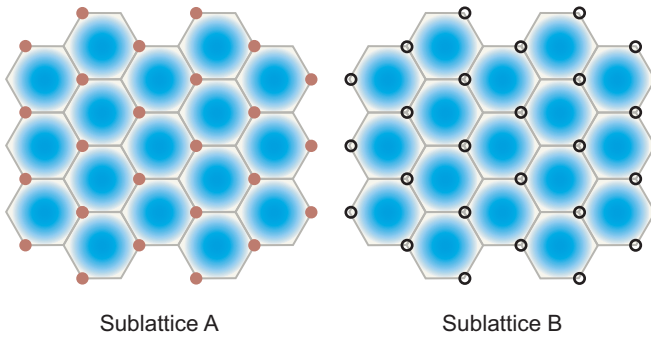
$$H = H_C + H_v + H_Z, \quad (108)$$

with the valley-independent Coulomb interaction H_C , the Zeeman energy H_Z , and the short-range, valley-dependent interaction H_v given respectively by

$$H_C = \frac{1}{2} \sum_{i \neq j} \frac{e^2}{\epsilon |\mathbf{r}_i - \mathbf{r}_j|} \quad H_Z = -\mu_B B \sum_i \sigma_z^i, \quad (109)$$

$$H_v = \frac{1}{2} \sum_{i \neq j} [g_z \tau_z^i \tau_z^j + g_\perp (\tau_x^i \tau_x^j + \tau_y^i \tau_y^j)] \delta(\mathbf{r}_i - \mathbf{r}_j),$$

where g_z and g_\perp are coupling constants, μ_B is the Bohr magneton, B is magnetic field strength, the Pauli matrices τ_α and

FIG. 19: Localization of valley wavefunctions in the $n = 0$ LL. In each valley K or K' , the wavefunction resides on only one sublattice, either A (solid red circles on left) or B (open black circles on right).

σ_α operate on valley isospin and spin, respectively, and the z direction for the spin space is assumed to be aligned with the magnetic field.

2. Symmetry and explicit symmetry breaking

Labeling states in a single Landau level by m_k and defining composite indices $\alpha \equiv \{x, y, z\}$ and $\beta \equiv \{x, y\}$, we may introduce the 15 operators

$$\begin{aligned} S_\alpha &= \sum_{m_k} \sum_{\tau \sigma \sigma'} \langle \sigma' | \sigma_\alpha | \sigma \rangle c_{\tau \sigma' m_k}^\dagger c_{\tau \sigma m_k}, \\ T_\alpha &= \sum_{m_k} \sum_{\sigma \tau \tau'} \langle \tau' | \tau_\alpha | \tau \rangle c_{\tau' \sigma m_k}^\dagger c_{\tau \sigma m_k}, \\ N_\alpha &= \frac{1}{2} \sum_{m_k} \sum_{\sigma \sigma' \tau} \langle \tau | \tau_z | \tau \rangle \langle \sigma' | \sigma_\alpha | \sigma \rangle c_{\tau \sigma' m_k}^\dagger c_{\tau \sigma m_k}, \\ \Pi_{\alpha\beta} &= \frac{1}{2} \sum_{m_k} \sum_{\sigma \sigma' \tau \tau'} \langle \tau' | \tau_\beta | \tau \rangle \langle \sigma' | \sigma_\alpha | \sigma \rangle c_{\tau' \sigma' m_k}^\dagger c_{\tau \sigma m_k}. \end{aligned} \quad (110)$$

The operator S_α represents the total spin and the operator T_α represents the total valley pseudospin. In the $n = 0$ Landau level for graphene there is an equivalence between valley and sublattice degrees of freedom, so N_α can be identified as a Néel vector in the $n = 0$ Landau level. The operators $\Pi_{\alpha\beta}$ couple the spin and valley isospin and will be discussed further below.

Under commutation the operators of Eq. (110) satisfy an SU(4) Lie algebra that commutes with the Coulomb interaction H_C [25]. Thus, if H_v and H_Z are much smaller than H_C , the Hamiltonian (108) has an approximate SU(4) symmetry. If Zeeman splitting is ignored, SU(4) symmetry is broken explicitly by H_v in Eq. (109), with the degree of symmetry breaking depending on the coupling parameters g_z and g_\perp . For characteristic graphene lattice spacings, terms involving g_z and g_\perp are much smaller than the SU(4)-symmetric Coulomb term and explicit breaking of SU(4) should be small in realistic systems. Four basic symmetry-breaking patterns have been studied, as summarized in Fig. 20 [24, 25].

1. For $g_z \neq 0$ and $g_\perp \neq 0$, the symmetry is broken to

$$\text{SU}(4) \supset \text{SU}(2)_s \times \text{U}(1)_v \supset \text{U}(1)_s \times \text{U}(1)_v, \quad (111)$$

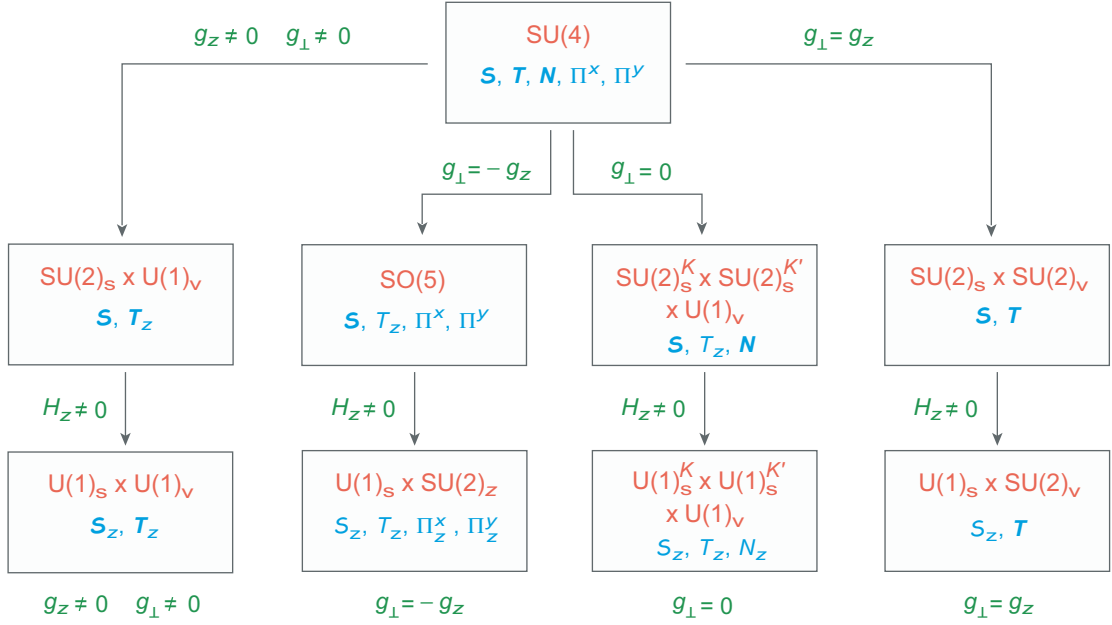


FIG. 20: Symmetry-breaking pattern for SU(4) quantum Hall ferromagnetism generated by the operators in Eq. (110) [24, 25]. The SU(4) symmetry is broken by explicit terms H_v and H_C in the Hamiltonian (108) that depend on the parameters g_z , g_\perp , and H_z .

where $SU(2)_s$ is associated with spin conservation, $U(1)_s$ with conservation of its z component, and $U(1)_v$ with conservation of T_z . If Zeeman splitting is ignored, spin is conserved but only the z component of valley isospin is conserved. The full Hamiltonian (108) with the Zeeman term conserves only the z components of spin and valley isospin.

2. If $g_\perp = 0$ but $g_z \neq 0$, the symmetry is broken in the manner

$$\begin{aligned} SU(4) \supset SU(2)_s^K \times SU(2)_s^{K'} \times U(1)_v \\ \supset U(1)_s^K \times U(1)_s^{K'} \times U(1)_v. \end{aligned} \quad (112)$$

If Zeeman splitting is neglected this implies conservation of spins independently in the K and K' valleys, but that valley isospin is broken to $U(1)_v$. If the Zeeman term is included, the full Hamiltonian (108) conserves only the z components of spin in each valley, and the z component of valley isospin.

3. If $g_z = g_\perp \neq 0$, the symmetry-breaking pattern is

$$SU(4) \supset SU(2)_s \times SU(2)_v \supset U(1)_s \times SU(2)_v. \quad (113)$$

In the absence of Zeeman splitting, this corresponds to full rotational symmetry in the spin and valley isospin spaces. If the Zeeman term is included in the full Hamiltonian (108), the $SU(2)$ isospin symmetry is conserved but only the z component of the spin is conserved.

4. If $g_\perp = -g_z \neq 0$, the 10 generators $\{\Pi_\alpha^B, \vec{S}, T_z\}$ commute with the Hamiltonian, forming the Lie group $SO(5)$. Thus

$$SU(4) \supset SO(5) \supset U(1)_s \times SU(2)_z, \quad (114)$$

where $\{T_z, \Pi_z^x, \Pi_z^y\}$ generates the $SU(2)_z$ symmetry [25]. If Zeeman splitting is neglected, the system exhibits an $SO(5)$ symmetry generated by spin and valley isospin. The full

Hamiltonian (108) with the Zeeman term included conserves $SU(2)_z$ but only the z component of spin. At a mean-field level, the 10 generators of the $SO(5)$ symmetry in Eq. (114) produce rotations on a vector space defined by order parameters associated with the remaining five generators of $SU(4)$: $\{T_x, T_y, N_x, N_y, N_z\}$ [25]. The vector space and the rotations generated by $SO(5)$ are illustrated schematically in Fig. 21(b), which generalizes the Bloch sphere of Fig. 21(a). The spin operators \mathbf{S} generate rotations in the Néel vector space \mathbf{N} , the operator T_z generates rotations in the valley vector space defined by T_x and T_y , and the Π operators rotate between the Néel and valley spaces. Thus $SO(5)$ is a symmetry interpolating between Néel states associated with N_α and states associated with valley isospin degrees of freedom T_x and T_y .

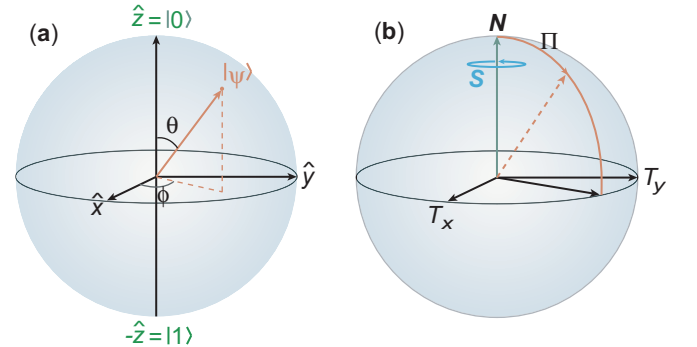


FIG. 21: (a) Bloch sphere representing a system with two basis states $|0\rangle$ and $|1\rangle$. (b) The 5D space operated on by the $SU(4) \supset SO(5)$ subgroup and the actions of the generators on this space. This represents a generalization of the Bloch sphere in (a). Adapted from Ref. [25].

XII. EMERGENT STATES IN MAGNETIC FIELDS

Little evidence exists for emergent states in neutral monolayer graphene, as expected because of the low density of states near the Fermi surface. However, in a strong magnetic field this situation changes since electrons in the resulting highly degenerate Landau levels can undergo strong electron–electron and electron–phonon interactions that can *break symmetries spontaneously rather than explicitly*. The spontaneous breaking of symmetry can produce highly collective states that differ qualitatively from low-lying states of the weakly interacting system with explicit symmetry breaking, since the emergent and weakly-interacting states are typically separated by quantum phase transitions.

As we have discussed in Ref. [26], there is evidence that the ground state of monolayer graphene in a strong magnetic field is such a (spontaneously) broken-symmetry state. In particular the ground state for monolayer graphene in a magnetic field is known to be very strongly insulating, exhibiting a rapid divergence of the longitudinal resistance R_L at a critical magnetic field B_c , with B_c smaller for cleaner samples. This behavior suggests that the resistance in this state is a consequence of emergent intrinsic properties of the state itself and not of impurity scattering.

With this motivation, let us turn to a discussion of emergent states in graphene created through strong electron–electron and electron–phonon correlations that break symmetries spontaneously rather than explicitly. We give first a more conventional view. Then we shall reformulate the discussion of graphene emergent states in terms of powerful new approaches based on fermion dynamical symmetries. In all of this discussion “graphene” will be shorthand for monolayer graphene in a strong magnetic field.

A. The role of correlations

Some general basis states for collective states that could be realized by placing two electron spins in $n = 0$ graphene valleys are illustrated in Fig. 22.

(1) In Fig. 22(a), both electrons are in the same valley (with opposite spins) and the adjacent valley is unoccupied, so valleys alternate in charge $+2e, 0, +2e, 0, \dots$, around the carbon ring. The right side of Fig. 22(a) illustrates the general lattice occupation, with adjacent sites alternating between being occupied by two spin-singlet electrons and by no electrons. This is a *charge density wave* (CDW).

(2) In Fig. 22(b), the electrons are in adjacent valleys with opposite spin projections. The right side of Fig. 22(b) illustrates the lattice occupation, with adjacent sites alternating between spin-up and spin-down electrons. This is an *antiferromagnetic* (AF) *spin-density wave* (SDW).

(3) In Fig. 22(c), the electrons are in adjacent valleys with the same spin projections. The right side of Fig. 22(c) illustrates the lattice occupation, with a spin-up electron at each site. This is a *ferromagnetically polarized state* (F).

(4) A fourth possible collective mode on the lattice is *Kekulé distortion* (KD), which induces alternating shorter and

longer bonds around the ring in the graphene structure (a “bond density wave” [28]). The terminology references August Kekulé, who proposed the alternating single and double bond structure for the benzene ring in Fig. 1(b). A Kekulé distortion state will be illustrated in Fig. 23(d) below.

The collective modes described above are illustrated schematically in Fig. 23. Assuming the effective Hamiltonian of Eq. (109) to capture the essential physics, we expect in the simplest picture that the system could be in one of four possible phases exhibiting different forms of long-range order [24].

1. A spin-singlet charge density wave phase CDW illustrated schematically in Fig. 23(a) that is not affected by the Zeeman term H_Z in the Hamiltonian.
2. A ferromagnetic phase F, illustrated schematically in Fig. 23(b). The symmetry is broken to $U(1)$ by H_Z , corresponding to conservation of spin projection.
3. An antiferromagnetic or Néel phase AF, illustrated schematically in Fig. 23(c). The symmetry is broken to $U(1)$ by H_Z , corresponding to conservation of spin projection.
4. A spin-singlet Kekulé distortion phase KD illustrated schematically in Fig. 23(d) that is not affected by the Zeeman term in the Hamiltonian.

These competing emergent modes are a result of correlations. Which, if any, of these modes are realized depends on which correlations dominate, which will now be discussed.

B. Symmetry-breaking interactions

Symmetries may be broken spontaneously by short-range electron–electron (e–e) interactions, and short-range electron–phonon (e–ph) interactions between the lattice and the electrons, with the electron–electron interactions generally being repulsive while the electron–phonon interactions are attractive. The most important e–ph interaction is thought to be Kekulé distortion, which perturbs the valley locations and contributes to the g_{\perp} coefficient in Eq. (109). Hence the valley-isospin T_x and T_y degrees of freedom should couple to Kekulé distortion modes. A systematic analysis by Kharitonov [24] suggests that the e–e interactions could favor any of the states described above: F, AF, CDW, or KD, depending on details of the symmetry-breaking interactions, but the leading terms in the attractive e–ph interactions always favor the KD mode.

Thus, we deal with a system having multiple possible emergent ground states, with the actual ground state determined by a delicate balance among the different e–e and e–ph interactions. This is the hallmark of *complexity*: a choice between competing emergent ground states that is sensitive to even weak external perturbations. Complexity is more common in soft condensed matter systems, but can occur in hard condensed matter systems when there are multiple collective ground-state candidates that are nearly degenerate, as we expect to be the case here.

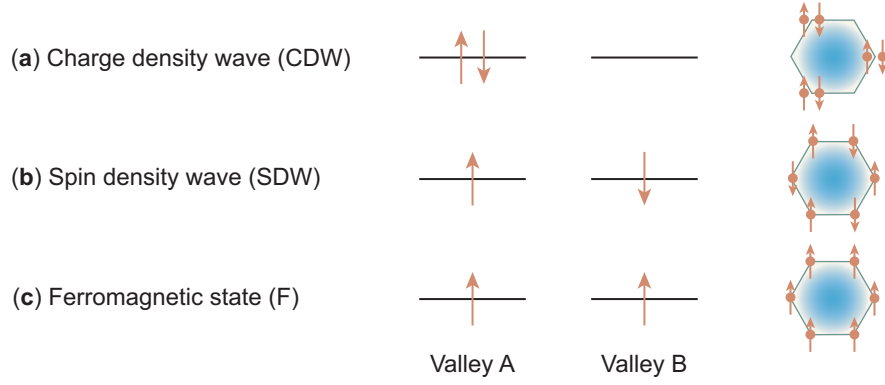


FIG. 22: Some possible basis states for collective states in the graphene $n = 0$ Landau level. Electron occupation for adjacent valleys A and B are shown, with up and down arrows indicating spin-up electrons and spin-down electrons, respectively. In the absence of Landau level mixing valley indices and the sublattice indices A and B coincide for $n = 0$. The corresponding lattice occupation is illustrated on the right. (a) A charge density wave (CDW). (b) A spin density wave (SDW). (c) A ferromagnetic state (F). Figure adapted from Ref. [27].

XIII. LOW-ENERGY COLLECTIVE MODES

In the preceding section we have seen that graphene in a strong magnetic field behaves as an $SU(4)$ ferromagnet if only the long-range Coulomb interaction is retained in the Hamiltonian. In the presence of shorter-range valley and spin interaction terms this symmetry is broken to an approximate $SU(4)$ symmetry. We discussed the classification of states with these terms in the Hamiltonian, and the effect of adding to the Hamiltonian the Zeeman term. Those considerations led to $SU(4)$ symmetry and symmetry-breaking classification schemes and serve as a basis for implementing numerical simulations or low-energy field theory approximations. In this section those symmetries and general principles will be used to elucidate wavefunctions for possible collective modes that could develop in graphene because of non-perturbative electron–electron and electron–phonon interactions.

A. Basis states for collective modes

Let us address some plausible basis states corresponding to the modes discussed in the preceding section, guided by the presentation in Kharitonov [24]. If attention is restricted to a single Landau level labeled by n , the degeneracy of states for a 2D electron gas in a magnetic field corresponds to the possible values of the quantum number m_k distinguishing the states for that n . However, for graphene the degeneracy of the Landau states (n, m_k) will be modified by the spin, sublattice pseudospin, and valley isospin degrees of freedom. In the simplest case where valley mixing is neglected we may equate the valley isospin and sublattice pseudospin labels, leaving potentially four additional degrees of freedom (valley isospin \otimes real spin) for each Landau state (n, m_k) . If these four “internal” degrees of freedom are taken to be degenerate, this leads to a Hamiltonian with $SU(4)$ symmetry for quantum Hall states. Physically, this corresponds to four copies of a Laughlin-like incompressible state as described in Section VIII B.

We begin by defining a Dirac 4-component field in the val-

ley and sublattice degrees of freedom with fixed spin polarization σ [24],

$$\psi_{\sigma}(\mathbf{r}) = \begin{pmatrix} \psi_{KA\sigma}(\mathbf{r}) \\ \psi_{KB\sigma}(\mathbf{r}) \\ \psi_{K'B\sigma}(\mathbf{r}) \\ -\psi_{K'A\sigma}(\mathbf{r}) \end{pmatrix}_{KK' \otimes AB}, \quad (115)$$

where the ordering and signs are chosen to give the most symmetric representation of the Dirac Hamiltonian and $KK' \otimes AB$ denotes the direct product of valley (KK') and sublattice (AB) degrees of freedom. Letting the spin polarization index σ take the two values \uparrow and \downarrow , the 8-component operator

$$\psi(\vec{r}) = \begin{pmatrix} \psi_{\uparrow}(\mathbf{r}) \\ \psi_{\downarrow}(\mathbf{r}) \end{pmatrix}_s \quad (116)$$

defines the most general spinor in the direct product of valley (KK'), sublattice (AB), and spin (s) spaces.

The $n = 0$ Landau level is located exactly at the Dirac point, and in each valley labeled by K or K' the wavefunctions reside entirely on one actual sublattice, $K \leftrightarrow A$ or $K' \leftrightarrow B$. Therefore, for the $n = 0$ level the field operator has only two non-vanishing components for a given spin polarization σ . Accordingly, in the $n = 0$ LL the non-vanishing components of Eq. (116) can be collected into a 4-component vector

$$\psi^{(0)}(\vec{r}) = \begin{pmatrix} \psi_{KA\uparrow}^{(0)}(\mathbf{r}) \\ \psi_{KA\downarrow}^{(0)}(\mathbf{r}) \\ \psi_{K'B\uparrow}^{(0)}(\mathbf{r}) \\ \psi_{K'B\downarrow}^{(0)}(\mathbf{r}) \end{pmatrix}_{KK' \otimes s} \quad (117)$$

in the valley isospin and spin space, where the superscript (0) indicates that this is valid specifically for the $n = 0$ LL.

B. Most general many-body wavefunction

Let the operator $c_{nm_k\lambda\sigma}^{\dagger}$ create an electron in the (n, m_k) Landau level with λ the sublattice or valley index and σ the spin

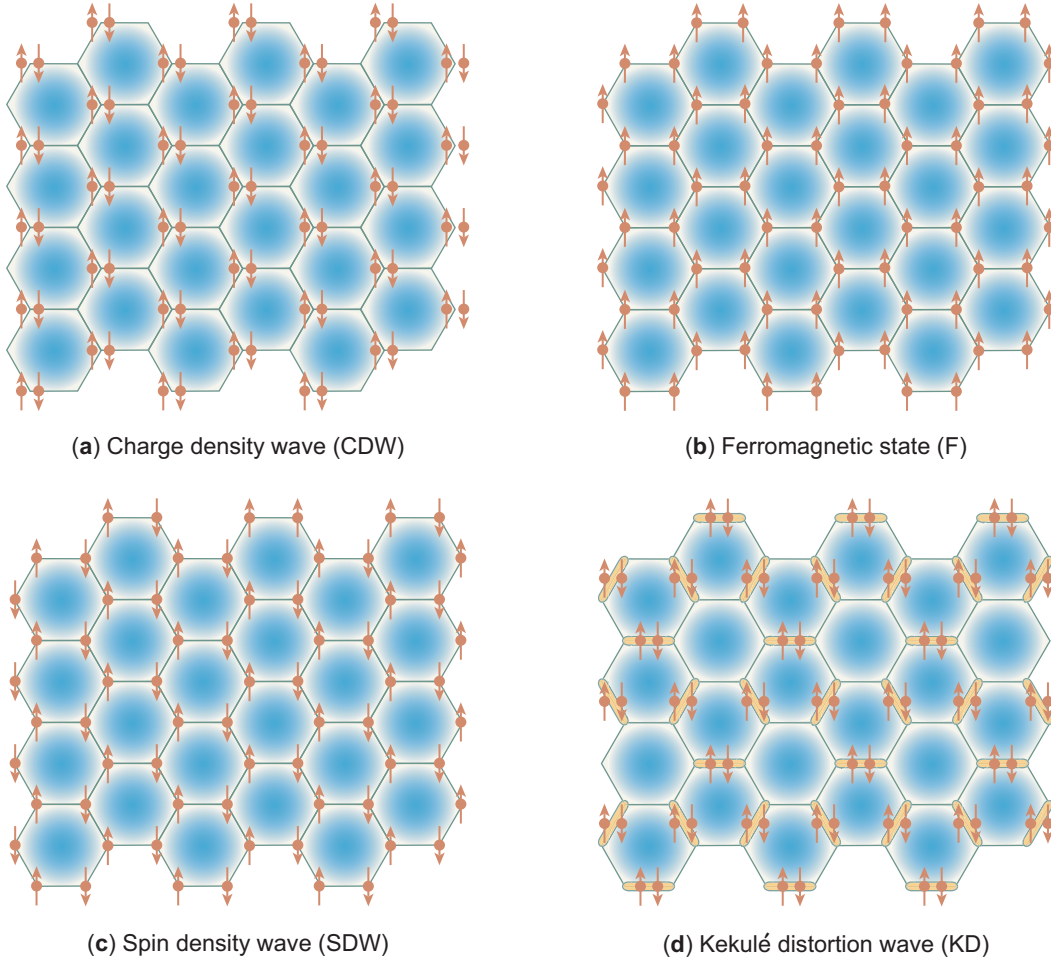


FIG. 23: Some collective states in the monolayer graphene, adapted from Ref. [24]. (a) Charge density wave (CDW). (b) Ferromagnetic state (F). (c) Spin density wave (SDW), corresponding to an antiferromagnetic Néel state. (d) Kekulé distortion (KD) mode (“bond density wave”).

polarization index. For the $\nu = 0$ state in graphene, corresponding to two electrons per 4-fold degenerate $n = 0$ Landau level, a general many-body wavefunction can be written [24]

$$\Psi = \prod_{m_k} \left(\sum_{\lambda\sigma, \lambda'\sigma'} \Phi_{\lambda\sigma, \lambda'\sigma'}^* c_{0m_k\lambda\sigma}^\dagger c_{0m_k\lambda'\sigma'}^\dagger \right) |0\rangle, \quad (118)$$

where the range of m_k is given by Eq. (97), and where the vacuum state $|0\rangle$ corresponds to completely filled Landau levels for $n < 0$ and completely empty Landau levels for $n \geq 0$. Each factor in the product \prod_{m_k} creates a pair of electrons in the state $\Phi = \{\Phi_{\lambda\sigma, \lambda'\sigma'}\}$ at orbital m_k of the $n = 0$ Landau level,

1. with λ and λ' equal to sublattice labels A or B,
2. with σ and σ' equal to spin-up (\uparrow) or spin-down (\downarrow),
3. and with the valley isospin and sublattice pseudospin labels identified: $K \leftrightarrow A$ and $K' \leftrightarrow B$.

Letting V denote the valley isospin symmetry and S the electron spin symmetry, the wavefunction Φ in Eq. (118) describes how the 4-fold degenerate $V \otimes S$ spin-isospin subspace of each orbital is occupied by two electrons.

C. Explicit vs. spontaneous symmetry breaking

States like the ground state in graphene are thought to be the result of *spontaneous symmetry breaking*, where the symmetry is broken by an unsymmetric vacuum rather than by explicit terms in the Hamiltonian. Then there are likely multiple solutions of the form (118) that have similar energy but represent emergent states having very different character, with the one of lowest energy determined by details of the symmetry-breaking correlations. Kharitonov [24] has given an overview examining states based on the $n = 0$ Landau level in the spirit of this section, with a general discussion of which are expected to be favored energetically. We refer readers to that discussion for more details of that approach.

We shall instead take a fundamental point of view that emergent states in graphene (or any many-body fermionic system) are separated from the weakly interacting states by a phase transition; thus they have no direct connection with states generated by explicit breaking of some symmetry. One needs exact solutions, or reasonable approximations, for states with symmetry broken spontaneously to investigate such emergent states. Within the framework discussed to this

point, these typically require numerical solutions. In Section XIV we shall introduce a different approach to determining the nature of low-lying emergent states based on dynamical symmetries for monolayer graphene in a magnetic field. The corresponding results will have two important implications.

1. We will be able to obtain *analytical solutions* that correspond to spontaneously broken symmetry, and thus to matrix elements of observables for possible emergent graphene states.
2. Our analysis will suggest that the most useful symmetry to break spontaneously for emergent states in monolayer graphene isn't $SU(4)$, as assumed in most discussions in the literature, but rather is an $SO(8)$ parent symmetry of $SU(4)$.

One important consequence is the prediction of more, and more varied, emergent states in graphene from breaking $SO(8)$ spontaneously than from breaking $SU(4)$ spontaneously.

XIV. FERMION DYNAMICAL SYMMETRY

The preceding material has given a general introduction to monolayer graphene in a strong magnetic field from a traditional point of view. The remainder of this review describes an alternative way to view the emergent states of this system, by solving for relevant matrix elements in a Hilbert space that has been truncated to a manageable collective subspace using the properties of Lie groups and Lie algebras. Reviews of these methods applied to various problems in nuclear structure physics and high-temperature superconductors may be found in Refs. [29–32] and references cited there, with a textbook overview given in Ref. [4]. Specific applications for graphene are given in Refs. [23, 26, 33] and in Ch. 20 of Ref. [4].

A. The microscopic dynamical symmetry method

The dynamical symmetry method uses generators of Lie groups and Lie algebras to construct a microscopic theory imposing a truncation of the full Hilbert space to a tractable subspace; Fig. 24(a) illustrates. Such a drastic truncation is justified if it leads to correct matrix elements for physical observables, as illustrated in Fig. 24(b). Two quantum theories may use different methodologies, but each must produce matrix elements of observables as physical output; valid comparisons between theories, and of theories to data, must be through *matrix elements corresponding to observables*. Wavefunctions and operators considered individually are *not observables* and thus are not a reliable basis of comparison.

A formal statement of the microscopic dynamical symmetry method begins with the following hypothesis [31]:

Dynamical Symmetry Hypothesis: Strongly-correlated emergent states imply a dynamical symmetry described by a Lie algebra that is generated by commutation of operators representing the emergent mode.

Dynamical symmetries may be defined for fermions or bosons, but our interest here will be in fermionic systems. The *Dynamical Symmetry Hypothesis* is supported by a large amount of evidence from various fields of many-body physics [4, 23, 26, 31–38].

B. Dynamical symmetry solution algorithm

Assuming the *Dynamical Symmetry Hypothesis*, microscopic solutions for emergent states in quantum many-body systems may be found by the following procedure [4, 31, 32].

1. Use phenomenology and theory to identify emergent degrees of freedom that are relevant physically for the problem.
2. *Close a commutation algebra* on a set of second-quantized operators creating, annihilating, and counting these modes. This Lie algebra is specified by the microscopic generators for emergent physical states and is termed the *highest symmetry*.
3. Truncate the full Hilbert space to a *collective subspace* by requiring that matrix elements of the operators found in the preceding step don't cause transitions out of the collective subspace. This dramatic reduction of the space is termed *symmetry-dictated truncation* (see Fig. 24). Collective states in this subspace have low energy but their wavefunction components are *selected by symmetry, not energy*. This means that they may contain both low-energy and high-energy components of a basis appropriate for the weakly interacting system.
4. Identify subalgebra chains of the highest symmetry ending in algebras imposing expected conservation laws, like those for charge and spin. Associated with these Lie algebras will be corresponding *Lie groups*.
5. Each subalgebra chain and corresponding subgroup chain specifies a *dynamical symmetry* associated with the highest symmetry, and each dynamical symmetry defines a *distinct quantum phase*. Thus a given highest symmetry can birth multiple quantum phases, each distinct physically but *all related through a common highest symmetry*.
6. Construct *dynamical symmetry Hamiltonians* that are polynomials in the Casimir invariants for subgroup chains. Each chain defines a wavefunction basis labeled by eigenvalues of chain invariants (Casimirs and elements of the Cartan subalgebras), and a Hamiltonian that is diagonal in this basis, because it is constructed from invariants.
7. Thus, the dynamical symmetries allow *the Schödinger equation to be solved analytically* for each subgroup chain.
8. Examine the physical content of each dynamical symmetry by *calculating matrix elements of observables*. This is possible because of the eigenvalues and eigenvectors obtained in step 6, and because consistency requires that any transition operators be related to group generators; otherwise transitions would mix irreducible multiplets and break the symmetry.
9. Construct the most general Hamiltonian in the model space as a linear combination of terms in the Hamiltonians for each symmetry group chain. Invariant operators of different subgroup chains don't generally commute, so an invariant for one chain may be a source of symmetry breaking for another.

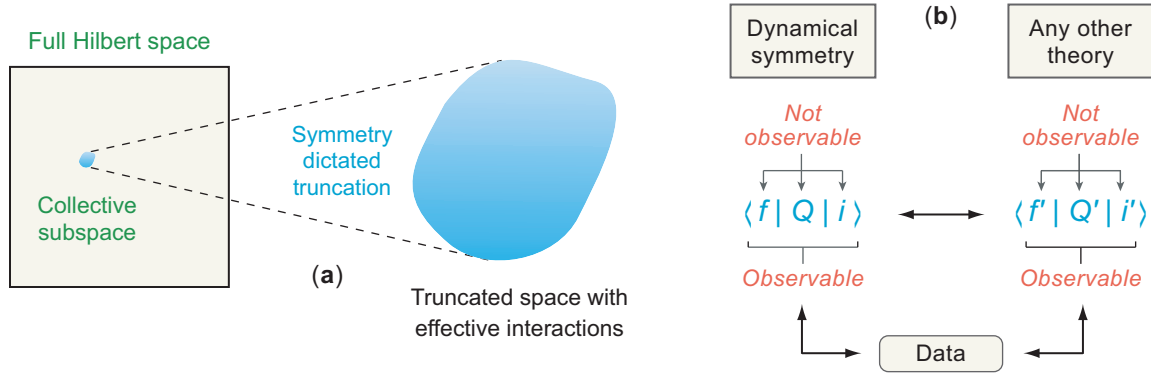


FIG. 24: (a) Emergent-symmetry truncation of the full fermionic Hilbert space to a collective subspace using principles of dynamical symmetry. (b) Comparison of matrix elements among different theories and data. Wavefunctions and operators are *not* observables. Only *matrix elements* are related directly to experimental data and serve as valid comparison criteria.

10. Thus the competition and quantum phase transitions between different dynamical symmetry chains may be studied.

11. More ambitious formulations that may include terms breaking the dynamical symmetries can be solved by

- a) coherent state or other approximations of the dynamical symmetry described in step (7), or
- b) perturbation theory around the symmetric solutions (which are non-perturbative vacuum states, so these “perturbative” solutions are actually non-perturbative with respect to the non-interacting ground state), or
- c) numerical solutions incorporating symmetry-breaking terms.

Reviews and applications of this methodology to both fermionic and bosonic systems in many fields may be found in Refs. [4, 23, 26, 31–38], and references cited there.

C. Validity of the dynamical symmetry approach

The *only approximation* in the microscopic dynamical symmetry approach is the symmetry-dictated truncation described in point (3) above and indicated schematically in Fig. 24; if all degrees of freedom are accounted for the method is microscopic and exact. Practically, only select degrees of freedom can be accommodated and the effect of the excluded Hilbert space must be incorporated through renormalized (effective) interactions operating in the truncated space. Thus the utility of the approach depends on

1. making a wise initial choice for the emergent degrees of freedom and their symmetries, and
2. the availability of sufficient information from theoretical understanding and phenomenology to specify the effective interactions in the truncated space.

As for any microscopic theory, the validity of this approach then stands on whether calculated matrix elements are consistent with experimental observables.

XV. DYNAMICAL SYMMETRY IN GRAPHENE

In most theoretical approaches, studying the emergent modes for monolayer graphene in a strong magnetic field requires numerical calculations, since the corresponding states are likely to be highly non-perturbative. Let us now address these states that were described in Sections XII and XIII, using the fermion dynamical symmetry method outlined in Section XIV. This will allow determining properties of various emergent states *analytically* rather than by computer calculations.

A. Basis states

Spin and valley isospin quantum number assignments for a useful basis are illustrated in Fig. 25 [compare with the wavefunction in Eq. (117)]. For example, consider the state labeled $|2\rangle$ in Fig. 25(c). The electron occupies valleys labeled by valley isospin K ($\tau = +$) [see Fig. 25(a-b)] with spin down ($\sigma = \downarrow$), so this basis state corresponds to quantum numbers in the second row of the table in Fig. 25(a). The table of Fig. 25(a) also displays a mapping of the four basis states labeled by a to a label m_i that takes values of the four possible projections $m_i = \{\pm\frac{1}{2}, \pm\frac{3}{2}\}$ of a fictitious angular momentum $i = 3/2$; this mapping will allow adaptation of some existing results in the literature to the graphene problem.

B. $SO(8)$ generators and Lie algebra

Let A_{ab}^\dagger create an electron pair with one electron in the $a = (\tau_1, \sigma_1)$ level and one in the $b = (\tau_2, \sigma_2)$ level, with m_k labeling $n = 0$ Landau states coupled to zero term by term,

$$A_{ab}^\dagger = \sum_{m_k} c_{am_k}^\dagger c_{b-m_k}^\dagger. \quad (119)$$

Then the hermitian conjugate $A_{ab} = (A_{ab}^\dagger)^\dagger$ annihilates a pair. [Don’t confuse m_k in (119) with the label m_i in Fig. 25(a).] There are $4 \times 4 = 16$ possible combinations ab in Eq. (119),

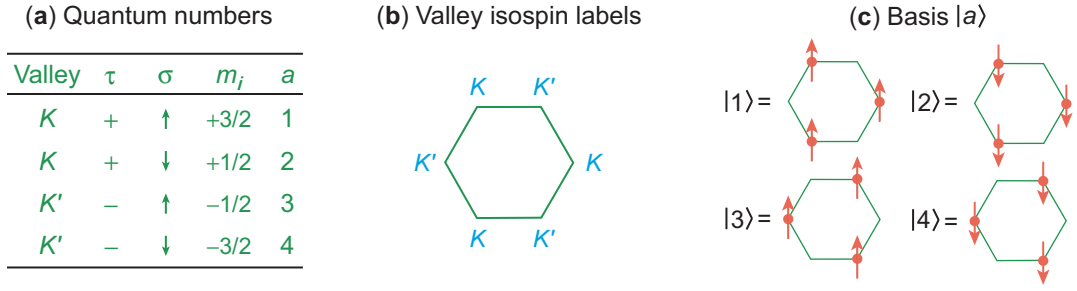


FIG. 25: (a) Valley isospin (τ) and spin (σ) quantum numbers. Each row of the table labeled by a corresponds to a basis state $|a\rangle$ displayed in (c). (b) The valley isospin labels K ($\tau = +$) and K' ($\tau = -$). (c) Four basis states corresponding to the rows of table (a).

but antisymmetry of fermionic wavefunctions reduces this to six independent operators A^\dagger and six independent hermitian conjugates A . Introduce also the 16 particle–hole operators,

$$B_{ab} = \sum_{m_k} c_{am_k}^\dagger c_{bm_k} - \frac{1}{4} \delta_{ab} \Omega, \quad (120)$$

where δ_{ab} is the Kronecker delta and Ω is the total degeneracy of the Landau level. Then the commutator algebra for the 28 operators A , A^\dagger , and B is [39]

$$[A_{ab}, A_{cd}^\dagger] = -B_{db} \delta_{ac} - B_{ca} \delta_{bd} + B_{cb} \delta_{ad} + B_{da} \delta_{bc}, \quad (121a)$$

$$[B_{ab}, B_{cd}] = \delta_{bc} B_{ad} - \delta_{ad} B_{cb}, \quad (121b)$$

$$[B_{ab}, A_{cd}^\dagger] = \delta_{bc} A_{ad}^\dagger + \delta_{bd} A_{ca}^\dagger, \quad (121c)$$

$$[B_{ab}, A_{cd}] = -\delta_{ac} A_{bd} - \delta_{ad} A_{cb}, \quad (121d)$$

which is isomorphic to the Lie algebra $SO(8)$.

C. A more physical generator basis

Generators of a Lie algebra span a linear vector space, so any independent linear combination generates the same algebra in a different basis. To facilitate interpretation for graphene, it is useful to express the generators of Eq. (121) in a new basis. First note that the operators in Eq. (120) can be replaced by the operators in Eq. (110) through comparing definitions (Section 4 of the Supplement [1]). By such methods the spin operators of Eq. (110) are given in terms of the B_{ab} generators as

$$S_x = B_{12} + B_{21} + B_{34} + B_{43}, \quad (122a)$$

$$S_y = -i(B_{12} - B_{21} + B_{34} - B_{43}), \quad (122b)$$

$$S_z = B_{11} - B_{22} + B_{33} - B_{44}, \quad (122c)$$

the valley isospin operators of Eq. (110) as

$$T_x = B_{13} + B_{31} + B_{24} + B_{42}, \quad (123a)$$

$$T_y = -i(B_{13} - B_{31} + B_{24} - B_{42}), \quad (123b)$$

$$T_z = B_{11} + B_{22} - B_{33} - B_{44}, \quad (123c)$$

the Néel vector of Eq. (110) as

$$N_x = \frac{1}{2}(B_{12} + B_{21} - B_{34} - B_{43}), \quad (124a)$$

$$N_y = -\frac{i}{2}(B_{12} - B_{21} - B_{34} + B_{43}), \quad (124b)$$

$$N_z = \frac{1}{2}(B_{11} - B_{22} - B_{33} + B_{44}), \quad (124c)$$

and the interpolating operators $\Pi_{\alpha\beta}$ of Eq. (110) as

$$\Pi_{xx} = \frac{1}{2}(B_{14} + B_{41} + B_{23} + B_{32}), \quad (125a)$$

$$\Pi_{yx} = -\frac{i}{2}(B_{23} - B_{32} + B_{41} - B_{14}), \quad (125b)$$

$$\Pi_{zx} = \frac{1}{2}(B_{13} + B_{31} - B_{24} - B_{42}), \quad (125c)$$

$$\Pi_{xy} = -\frac{i}{2}(B_{32} - B_{23} + B_{41} - B_{14}), \quad (125d)$$

$$\Pi_{yy} = -\frac{1}{2}(B_{41} + B_{14} - B_{23} - B_{32}), \quad (125e)$$

$$\Pi_{zy} = -\frac{i}{2}(B_{31} - B_{13} - B_{42} + B_{24}). \quad (125f)$$

Inverse transformations expressing the B_{ab} in terms of the $\{S_\alpha, T_\alpha, N_\alpha, \Pi_{\alpha x}, \Pi_{\alpha y}\}$ are given in Section 4 of the Supplement [1]. From Appendix D, the $SU(4)$ algebra generated by the operators in Eq. (110) is a subalgebra of the $SO(8)$ algebra, with its generators corresponding to particular linear combinations of the subset of $SO(8)$ generators defined by the particle–hole operators B_{ab} in Eq. (120).

D. Coupled representations for pair operators

Next, observe that valley isospin is approximately conserved for low-lying states and spin is conserved if Zeeman splitting can be ignored. Hence it is useful to employ pairing operators coupled to states of good total spin and good total valley isospin. An operator creating an electron pair coupled to good spin and isospin may be written

$$A_{M_S M_T}^{\dagger ST} \equiv \sum_{m_1 m_k} \sum_{n_1 n_2} \langle \frac{1}{2} m_1 \frac{1}{2} m_2 | S M_S \rangle \times \langle \frac{1}{2} n_1 \frac{1}{2} n_2 | T M_T \rangle c_{m_1 n_1 m_k}^\dagger c_{m_2 n_2 - m_k}^\dagger, \quad (126)$$

where in this equation

- S is the total spin, with projection M_S ,
- T is the total valley isospin, with projection M_T ,
- the $SU(2)$ Clebsch–Gordan coefficient $\langle \frac{1}{2} m_1 \frac{1}{2} m_2 | S M_S \rangle$ couples the spins to good total spin $|S M_S\rangle$, and
- the $SU(2)$ Clebsch–Gordan coefficient $\langle \frac{1}{2} n_1 \frac{1}{2} n_2 | T M_T \rangle$ couples the isospins to good total isospin $|T M_T\rangle$.

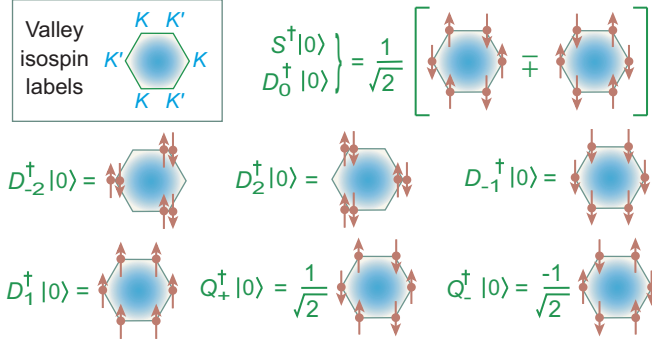


FIG. 26: Configurations resulting from the pair creation operators of Eq. (128) operating on the vacuum $|0\rangle$. Location of the dots (K or K' site) indicates valley isospin; arrows indicate spin polarization.

The fermion pair wavefunctions are restricted to total spin and isospin combinations ($S = 1, T = 0$) or ($S = 0, T = 1$) by the antisymmetry requirement. The six coupled pairing operators constructed from Eq. (126) that satisfy this condition are

$$\begin{aligned} S^\dagger &= \frac{1}{\sqrt{2}} (A_{14}^\dagger - A_{23}^\dagger) & D_0^\dagger &= \frac{1}{\sqrt{2}} (A_{14}^\dagger + A_{23}^\dagger), \\ D_1^\dagger &= A_{13}^\dagger & D_{-1}^\dagger &= A_{24}^\dagger, \\ D_2^\dagger &= A_{12}^\dagger & D_{-2}^\dagger &= A_{34}^\dagger, \end{aligned} \quad (127)$$

while $S = (S^\dagger)^\dagger$ and $D_\mu = (D_\mu^\dagger)^\dagger$ represent six corresponding hermitian-conjugate annihilation operators. The six equations (127), their six hermitian conjugates, the 15 equations (110), and the number operator S_0 defined in Eq. (150) (see also Appendix D) represent independent linear combinations of the 28 generators of $\text{SO}(8)$ defined in Eqs. (119) and (120). Therefore, since Eq. (121) defines an $\text{SO}(8)$ Lie algebra, the 28 operators

$$G_{\text{SO}(8)} = \{S_\alpha, T_\alpha, N_\alpha, \Pi_{\alpha x}, \Pi_{\alpha y}, S_0, S, S^\dagger, D_\mu, D_\mu^\dagger\} \quad (128)$$

constitute an equally valid set of generators for $\text{SO}(8)$, expressed in a new generator basis.

E. $\text{SO}(8)$ pair states in graphene

Configurations resulting from applying the pair creation operators in Eq. (128) to the vacuum $|0\rangle$ are shown in Fig. 26, as are configurations generated by the linear combinations

$$|Q_\pm\rangle = Q_\pm^\dagger |0\rangle \equiv \frac{1}{2} (S^\dagger \pm D_0^\dagger) |0\rangle = \frac{1}{2} (|S\rangle \pm |D_0\rangle), \quad (129)$$

which will prove to be useful later. The physical meaning of the states in Fig. 26 may be clarified by constructing the corresponding electronic configurations. For example, consider D_2^\dagger applied to $|0\rangle$ for a single Landau level (so we omit a LL index). From Eqs. (127) and (119),

$$D_2^\dagger = \frac{1}{\sqrt{2}} A_{10}^\dagger = A_{12}^\dagger = \sum_{m_k} c_{1m_k}^\dagger c_{2-m_k}^\dagger = \sum_{m_k} c_{K\uparrow m_k}^\dagger c_{K\downarrow -m_k}^\dagger,$$

where the correspondence between the labels $a = 1, 2, 3, 4$ and the valley and spin labels in Fig. 25(a) was used. We conclude that $D_2^\dagger |0\rangle$ creates a state with one spin-up and one spin-down electron on each equivalent site K . For the graphene hexagon the spin is zero on each site for this state but the charge alternates from 0 (no electrons) to -2 (two electrons) between adjacent sites; thus $D_2^\dagger |0\rangle$ generates a *charge density wave* on the K sites. By similar considerations, application of the generator D_{-2}^\dagger to the pair vacuum $|0\rangle$ generates a charge density wave on the K' sites.

It is convenient to introduce *order parameters* to keep track of emergent order on the lattice,

$$\begin{aligned} \langle S_z \rangle &\equiv \langle \hat{n}_1 \rangle - \langle \hat{n}_2 \rangle + \langle \hat{n}_3 \rangle - \langle \hat{n}_4 \rangle \\ \langle T_z \rangle &\equiv \langle \hat{n}_1 \rangle + \langle \hat{n}_2 \rangle - \langle \hat{n}_3 \rangle - \langle \hat{n}_4 \rangle, \\ \langle N_z \rangle &\equiv \langle \hat{n}_1 \rangle - \langle \hat{n}_2 \rangle - \langle \hat{n}_3 \rangle + \langle \hat{n}_4 \rangle, \end{aligned} \quad (130)$$

where \hat{n}_i counts electrons in basis state $|i\rangle$. These have the following interpretation.

1. $\langle S_z \rangle$ measures net spin (*ferromagnetic order*).
2. $\langle T_z \rangle$ measures the difference in charge between the K and K' sites (*charge order*).
3. $\langle N_z \rangle$ measures the difference in spins between the K and K' sites (*antiferromagnetic order*, also known as *Néel* or *spin density wave order*).

For example, $D_2^\dagger |0\rangle$ in Fig. 26 was interpreted above as a component of a charge density wave. Evaluating Eq. (130) for this state gives $\langle T_z \rangle = 2$ and $\langle S_z \rangle = \langle N_z \rangle = 0$, which characterizes a state having charge density wave order but no ferromagnetic or antiferromagnetic order, consistent with our earlier interpretation. Evaluation of the order parameters using Eq. (130) for the other pair states in Fig. 26 suggests the following physical interpretations for these operators applied to the pair vacuum.

1. $D_{\pm 2}^\dagger$ generates *charge density waves*, with charge concentrated on alternate sites.
2. $D_{\pm 1}^\dagger$ generates *ferromagnetic states* in which electrons are distributed equally on all sites, with all spins aligned.
3. S^\dagger, D_0^\dagger , and Q_\pm^\dagger generate *antiferromagnetic spin waves* with a single spin on each site, but spin direction alternating between adjacent sites.

These operators can create emergent states corresponding to highly collective pairing condensates exhibiting a rich variety of structure, as will now be demonstrated.

F. The $\text{SO}(8)$ collective subspace

Let us work in a single $n = 0$ Landau level, so we suppress the LL index and assume $2k + 1$ degenerate states in the Landau level labeled by the integer quantum number m_k , with

$$m_k = \{-k, -k + 1, \dots, k - 1, k\}. \quad (131)$$

A $2N$ -fermion state is produced by acting N times on the vacuum with $\text{SO}(8)$ pair creation operators of Eq. (127) [23, 26, 31, 32],

$$|\text{SO}(8)\rangle = (S^\dagger)^{N_S} (D^\dagger)^{N_D} |0\rangle, \quad (132)$$

where in this expression

- N_S is the number of S pairs (created by S^\dagger operators),
- N_D is the number of D pairs (created by D^\dagger operators),
- $N = N_S + N_D$ is the total number of pairs, and
- the pair creation operators S^\dagger and D^\dagger are defined in Eq. (127).

A more general wavefunction could have u broken pairs, but states with no broken pairs are expected to dominate at low energy and we consider only $u = 0$ here. As will be shown in Section XV G, the wavefunction (132) written as a product of collective fermion pairs is in fact *equivalent* to the wavefunction (118) used often in the literature for the $\text{SU}(4)$ subspace—despite their superficially different structure—as a consequence of the Pauli exclusion principle.

G. Structure of $\text{SO}(8)$ pairs

In this section we demonstrate the equivalence of the $\text{SO}(8)$ pair state defined by Eq. (132) and the state defined by Eq. (118). From Eqs. (127) and (132), an N -pair state in the $u = 0$ subspace (no broken pairs) is given by

$$|\Psi\rangle = (A_{12}^\dagger)^{N_{12}} (A_{13}^\dagger)^{N_{13}} (A_{14}^\dagger)^{N_{14}} (A_{23}^\dagger)^{N_{23}} \times (A_{24}^\dagger)^{N_{24}} (A_{34}^\dagger)^{N_{34}} |0\rangle, \quad (133)$$

where the total pair number N is

$$N = \frac{1}{2}n = N_{12} + N_{13} + N_{14} + N_{23} + N_{24} + N_{34}, \quad (134)$$

with n the total number of electrons and N_{ab} the number of electron pairs created by A_{ab}^\dagger operating on the vacuum state. From Eq. (121b), the B_{ab} form an $\text{SU}(4)$ subalgebra of the $\text{SO}(8)$ algebra (121) under commutation (see Appendix D). Let us investigate the $\text{SO}(8)$ pair structure by considering the irreducible representations (irreps) associated with the $\text{SO}(8) \supset \text{U}(4) \supset \text{SU}(4)$ subgroup chain.

1. Pauli restrictions on collective pairs

If no pairs are broken ($u = 0$), at half filling the number of pairs is $N = \frac{1}{2}\Omega = 2k + 1$. The highest-weight $\text{U}(4)$ representation is given by $(\frac{1}{2}\Omega, \frac{1}{2}\Omega, 0, 0)$, where we use $\text{SO}(6)$ quantum numbers to label the $\text{SU}(4)$ states, since $\text{SU}(4)$ and $\text{SO}(6)$ are homomorphic. Define a highest-weight (HW) state in this space to be the pair state with maximal value of m_i from the table in Fig. 25(a). This state has one electron in the $a = 1$

level and one electron in the $a = 2$ level. Thus, for $N = 2k + 1$ pairs the highest-weight state is

$$|\text{HW}\rangle = \frac{1}{(2k+1)!} (A_{12}^\dagger)^{2k+1} |0\rangle \\ = \frac{1}{(2k+1)!} \left(\sum_{m_k} c_{1m_k}^\dagger c_{2,-m_k}^\dagger \right)^{2k+1} |0\rangle, \quad (135)$$

with the sum running over the $2k + 1$ states in the Landau level labeled by the quantum number m_k of Eq. (131). The other states of the irreducible representation may then be created by successive judicious application of lowering and raising operators, beginning with the highest weight state (the standard *Cartan–Dynkin algorithm*) [4]. The highest weight state (135) seems quite complicated, involving a sum with many terms raised to a high power. However, *because of the Pauli principle* the actual structure of this state is much simpler than Eq. (135) might suggest.

We may illustrate by a simple example, constructing explicitly the highest-weight state for $k = 1$, which corresponds to $2k + 1 = 3$ pairs in a single Landau level. Writing out the sum over $m_k = \{-1, 0, +1\}$ in Eq. (135) gives

$$|\text{HW}\rangle = \frac{1}{3!} \left(c_{1,-1}^\dagger c_{21}^\dagger + c_{10}^\dagger c_{20}^\dagger + c_{11}^\dagger c_{2,-1}^\dagger \right)^3 |0\rangle \\ = c_{10}^\dagger c_{20}^\dagger c_{11}^\dagger c_{21}^\dagger c_{1,-1}^\dagger c_{2,-1}^\dagger |0\rangle \\ = \prod_{m_k=-k}^{m_k=+k} c_{1m_k}^\dagger c_{2m_k}^\dagger |0\rangle,$$

where the *Pauli principle* (antisymmetry of the fermion creation operators) causes any products having two or more creation operators with the same index to vanish in raising the sum inside the parentheses to the $2k + 1$ power. Applying similar considerations for arbitrary k , the most general highest-weight state is

$$|\text{HW}\rangle = \frac{1}{N!} (A_{12}^\dagger)^N |0\rangle = \frac{1}{N!} \left(\sum_{m_k} c_{1m_k}^\dagger c_{2,-m_k}^\dagger \right)^N |0\rangle \\ = \prod_{m_k=-k}^{m_k=+k} c_{1m_k}^\dagger c_{2m_k}^\dagger |0\rangle, \quad (136)$$

where the simplification in the last step again follows from the Pauli principle. Thus the highest-weight state is a product state of pairs, one for each of the $N = 2k + 1$ states labeled by m_k in the Landau level. Other states can be constructed by applying the Cartan–Dynkin algorithm. These will be functions of the generators B_{ab} , so for an arbitrary state $|\psi\rangle$ in the weight space

$$|\psi\rangle = F(B_{ab}) |\text{HW}\rangle, \quad (137)$$

where the function $F(B_{ab})$ is specified by the Cartan–Dynkin procedure. For example, from Eqs. (123) and (120) the lowering operator T_- is given by

$$T_- \equiv \frac{1}{2}(T_x - iT_y) = \sum_{m_k} (c_{k'\uparrow m_k}^\dagger c_{k\uparrow m_k} + c_{k'\downarrow m_k}^\dagger c_{k\downarrow m_k}),$$

and the state produced by acting with T_- on the highest-weight state is

$$\begin{aligned} |\psi\rangle &= T_- |\text{HW}\rangle \\ &= \prod_{m_k} \left[\sum_{n_k} (c_{k'\uparrow n_k}^\dagger c_{k\uparrow n_k} + c_{k'\downarrow n_k}^\dagger c_{k\downarrow n_k}) \right] c_{k'\uparrow m_k}^\dagger c_{k\downarrow m_k}^\dagger |0\rangle \\ &= \prod_{m_k} (c_{3m_k}^\dagger c_{2m_k}^\dagger + c_{4m_k}^\dagger c_{1m_k}^\dagger) |0\rangle, \end{aligned} \quad (138)$$

where the only terms that survive in the final expression are characterized by having an annihilation operator in a factor inside the square brackets that is balanced by a creation operator from the factor outside the square brackets. All other $u = 0$ states follow from successive applications of raising and lowering operators formed from the generators in Eqs. (122)–(125).

2. Pair and product wavefunctions

From the preceding discussion, the states at half filling corresponding to $N = \frac{1}{2}\Omega$ take the form

$$\begin{aligned} |\psi\rangle &= F(B_{ab}) |\text{HW}\rangle \\ &= \prod_{m_k} \left(\sum_{\tau\sigma\tau'\sigma'} \Phi_{\tau\sigma\tau'\sigma'}^* c_{\tau\sigma m_k}^\dagger c_{\tau'\sigma' m_k}^\dagger \right) |0\rangle, \end{aligned} \quad (139)$$

where τ, τ' are valley isospin projection quantum numbers and σ, σ' are spin projection quantum numbers. This is the same form (118) as the most general collective pair state used by Kharitonov in Ref. [24] to classify possible broken symmetry states for the $n = 0$ Landau level in graphene.

Thus, the general pairing wavefunction of Eq. (132) that characterizes the $\text{SO}(8) \supset \text{SU}(4)$ fermion dynamical symmetry is *equivalent to the product form in Eq. (118)* appearing in standard discussions of quantum Hall ferromagnetism, for which the summations are over the internal (τ, σ) rather than Landau (m_k) degrees of freedom.

The equivalence of Eqs. (132) and (118) is a consequence of the Pauli principle and the fundamental restriction that it places on allowed pair configurations within the collective subspace of fermion pairs.

H. Beyond quantum Hall ferromagnetism

The B_{ab} operators of Eq. (120) are in one-to-one correspondence with the operators used to formulate the effective low-energy Hamiltonian (108) describing explicit breaking of $\text{SU}(4)$ symmetry in quantum Hall ferromagnetism. Thus all physics discussed in the prior literature using this effective Hamiltonian (see [24, 25] and references cited therein)

is implicit in the present formalism. Moreover, the discussion of Section XV G 2 shows that the pair basis (133) spanning the collective subspace of the $\text{SO}(8)$ fermion dynamical symmetry is *equivalent* to the most general wavefunction (118) that has been proposed [24] for collective states breaking the $\text{SU}(4)$ symmetry spontaneously, despite an apparent difference in form.

Thus the collectively-paired $\text{SO}(8)$ subspace truncation of the full Hilbert space recovers the understanding in the existing literature of the classes of states to be expected from spontaneous breaking of the $\text{SU}(4)$ symmetry. However, the existing discussions of these collective states have been largely qualitative, and have turned to numerical simulations or simplified models to discuss the actual structure of these emergent states. We shall now show that the present Fermion dynamical symmetry formalism is capable of addressing the quantitative nature of those collective states *analytically*.

I. Graphene $\text{SO}(8)$ dynamical symmetries

The subset of the full Hilbert space spanned by the states specified by Eq. (132) is assumed to correspond to the *collective subspace* of Fig. 24(a). Following the procedure outlined in Section XIV B, the $\text{SO}(8)$ symmetry can be used to construct effective Hamiltonians that are diagonal in this subspace, the $\text{SO}(8)$ generators don't couple the collective subspace to the rest of the Hilbert space, and effective interactions operate in the collective subspace that represent the average effect of the excluded Hilbert space. The pair basis displayed in Fig. 26 can exhibit charge density wave, antiferromagnetic, and ferromagnetic order. Therefore, the pair condensate defined by Eq. (132) can produce a rich variety of strongly-correlated quantum phases that correspond in the mean-field limit to spontaneously broken symmetries. Let's examine some of those solutions.

The graphene $\text{SO}(8)$ subgroup chains that end in the group $\text{SU}(2)_\sigma \times \text{U}(1)_c$ imposing spin and charge conservation are shown in Fig. 27, with Zeeman splitting ignored. If Zeeman splitting were included it would influence directly only the spin sector and break $\text{SU}(2)_\sigma$ down to the $\text{U}(1)_\sigma$ group generated by \mathcal{S}_z . Seven subgroup chains are displayed, representing seven distinct subgroup paths (indicated by directed line segments) connecting the highest symmetry $\text{SO}(8)$ to the final symmetry $\text{SU}(2)_\sigma \times \text{U}(1)_c$ imposing spin and charge conservation. Each defines an emergent mode representing a distinct quantum phase for which matrix elements such as those for energies, order parameters, and transition rates may be calculated analytically within the dynamical symmetry formalism. The following examples describe several of these subgroup chains.

1. The set $\{\mathcal{S}, \mathcal{S}^\dagger, \mathcal{S}_0\}$ generates an $\text{SU}(2)_p$ Lie group and the set $\{\mathcal{S}_\alpha, \Pi_{\alpha x}, \Pi_{\alpha y}, T_z\}$ generates an $\text{SO}(5)$ Lie group that commutes with the $\text{SU}(2)_p$ group. Furthermore, the components of the total spin \mathcal{S}_α generate an $\text{SU}(2)_\sigma$ subgroup of $\text{SO}(5)$ and \mathcal{S}_0 generates a $\text{U}(1)_c$ subgroup of $\text{SU}(2)_p$. Thus one emergent state with highest symmetry $\text{SO}(8)$ that conserves spin and charge corresponds to the dynamical symmetry sub-

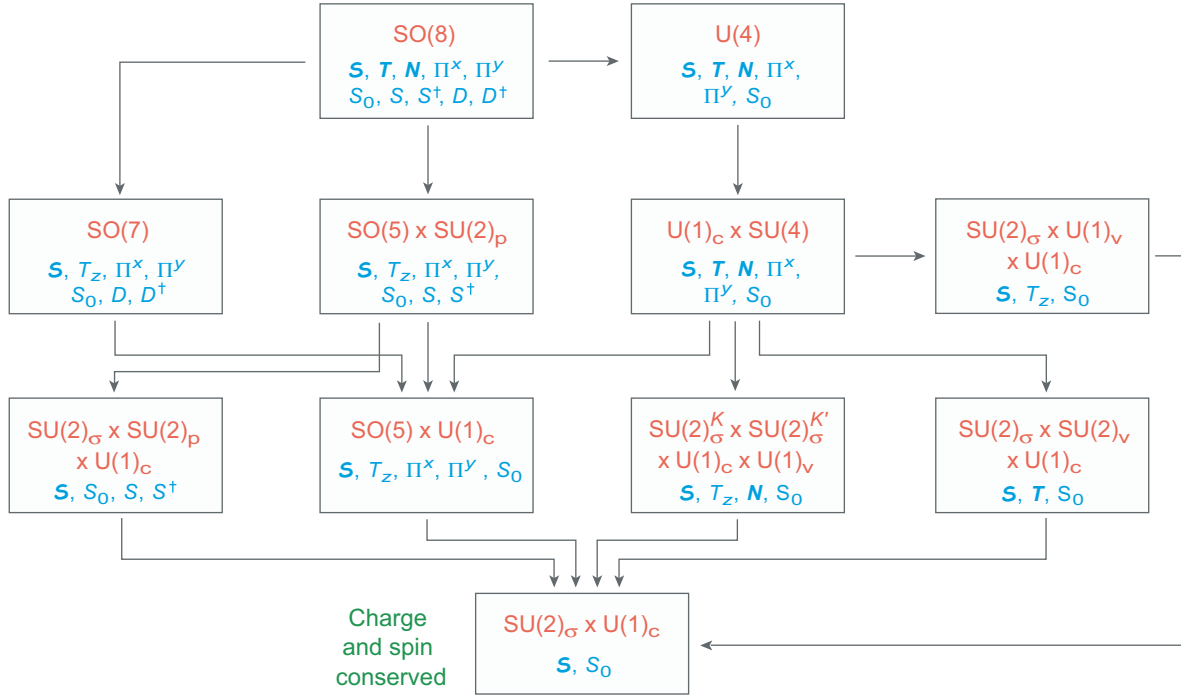


FIG. 27: $SO(8)$ fermion dynamical symmetry subgroup chains for monolayer graphene in a magnetic field [23, 26, 33]. Each box is labeled by a Lie group in red and the group generators in blue. Seven subgroup chains are indicated by directed paths beginning at the highest symmetry $SO(8)$ and ending with the group $SU(2)_\sigma \times U(1)_c$ corresponding to conservation of charge and spin. These subgroup chains define seven distinct fermion dynamical symmetries that correspond to seven different emergent states or quantum phases, that are compatible with the $SO(8)$ highest symmetry and that conserve charge and spin (If the Zeeman term is ignored in the Hamiltonian). If the Zeeman term is included it affects only the spin sector and breaks $SU(2)_\sigma$ down to the $U(1)_\sigma$ group generated by \mathcal{S}_z .

group chain

$$\begin{aligned} SO(8) &\supset SO(5) \times SU(2)_p \\ &\supset SU(2)_\sigma \times SU(2)_p \supset SU(2)_\sigma \times U(1)_c \end{aligned} \quad (140)$$

displayed in Fig. 27. Alternatively, $SO(5)$ may be broken according to the dynamical symmetry pattern

$$\begin{aligned} SO(8) &\supset SO(5) \times SU(2)_p \\ &\supset SO(5) \times U(1)_c \supset SU(2)_\sigma \times U(1)_c, \end{aligned} \quad (141)$$

which also has highest symmetry $SO(8)$ with conserved spin and charge, but represents a different quantum phase than that described by the chain of Eq. (140).

2. Removal of the 12 pairing operators $\{S, S^\dagger, D_\mu, D_\mu^\dagger\}$ from the $SO(8)$ generators in Eq. (128) yields the 16-generators of a $SO(8) \supset U(4) \supset U(1)_c \times SU(4)$ subgroup, with the $U(1)_c$ subgroup generated by the particle number operator S_0 and the $SU(4)$ subgroup generated by the 15 generators of Eq. (110). There are several options for $SO(8) \supset U(4) \supset U(1)_c \times SU(4)$ subgroup chains.

- (a) The subset $\{S_\alpha, \Pi_{\alpha x}, \Pi_{\alpha y}, T_z\}$ generates an $SO(5)$ subgroup of $SU(4)$; hence

$$\begin{aligned} SO(8) &\supset U(4) \supset U(1)_c \times SU(4) \\ &\supset SO(5) \times U(1)_c \supset SU(2)_\sigma \times U(1)_c \end{aligned} \quad (142)$$

is one possibility.

- (b) A $SU(2)_\sigma^K \times SU(2)_\sigma^{K'}$ symmetry results if inter-valley scattering is ignored and spin is conserved within each valley. Thus a second subgroup chain is

$$\begin{aligned} SO(8) &\supset U(4) \supset U(1)_c \times SU(4) \\ &\supset SU(2)_\sigma^K \times SU(2)_\sigma^{K'} \times U(1)_c \times U(1)_\nu \\ &\supset SU(2)_\sigma \times U(1)_c, \end{aligned} \quad (143)$$

where T_z generates the $U(1)_\nu$ subgroup.

- (c) A third subgroup chain is

$$\begin{aligned} SO(8) &\supset U(4) \supset U(1)_c \times SU(4) \\ &\supset SU(2)_\sigma \times SU(2)_\nu \times U(1)_c \\ &\supset SU(2)_\sigma \times U(1)_c. \end{aligned} \quad (144)$$

The three chains (142)-(144) represent physically distinct emergent states that conserve charge and spin. They are related by having the same $SO(8)$ highest symmetry, but correspond to different collective excitations that are selected by different effective interaction parameter sets.

3. The 21 operators

$$G_{SO(7)} = \{S_\alpha, \Pi_{\alpha x}, \Pi_{\alpha y}, T_z, S_0, D_\mu^\dagger, D_\mu\}$$

generate an $SO(7)$ subgroup of $SO(8)$ and the 11 operators

$$G_{SO(5)} = \{S_\alpha, \Pi_{\alpha x}, \Pi_{\alpha y}, T_z, S_0\}$$

generate an $\text{SO}(5) \times \text{U}(1)_c$ subgroup of $\text{SO}(7)$, implying a subgroup chain

$$\text{SO}(8) \supset \text{SO}(7) \supset \text{SO}(5) \times \text{U}(1)_c \supset \text{SU}(2)_\sigma \times \text{U}(1)_c. \quad (145)$$

This subgroup chain defines a *critical dynamical symmetry*, where an entire quantum phase can exhibit critical behavior; this will be discussed further in Section XV M below.

The states represented by dynamical symmetry chains in Fig. 27 are *non-perturbative (emergent)* and represent *different quantum phases*. These are strongly-correlated, exact many-body solutions but, using mean-field language, the symmetry has been *broken spontaneously* for these states. The quantum phases of Fig. 27 are separated by quantum phase transitions and cannot be related perturbatively to each other, nor can they be related perturbatively to the states corresponding to small fluctuations around $\text{SU}(4)$ symmetry of the quantum Hall ferromagnetism model in Fig. 20. We may gain a deeper understanding of these broken-symmetry states by using *generalized coherent states* to approximate the exact dynamical symmetry solutions corresponding to the subgroup chains of Fig. 27.

J. Generalized coherent states for graphene

The dynamical symmetry limits represented by subgroup chains in Fig. 27 correspond to particular choices of effective interaction parameters and have *exact analytical solutions* for physical matrix elements. For arbitrary values of effective interaction parameters, solutions are superpositions of the different symmetry-limit solutions that are not easily expressed in concise analytical form. In this more general case there is a powerful alternative: the *generalized coherent state approximation*, which permits analytical solutions for values of interaction parameters that need not correspond to symmetry limits. An overview of this method may be found in Ch. 21 of Ref. [4] and a more comprehensive technical review has been given in Ref. [40].

One way to visualize the nature of the collective states that are implied by the subgroup chains of Fig. 27 is to use coherent states to construct the corresponding ground-state total energy surfaces. In generalized coherent state approximation for the present case the energy is determined by the variational condition $\delta \langle \eta | H | \eta \rangle = 0$, with H the $\text{SO}(8)$ Hamiltonian and $|\eta\rangle$ the coherent state. Let us illustrate the method for the three subgroup chains of Fig. 27 that contain the $\text{SO}(5) \times \text{U}(1)_c$ subgroup. Thus our coherent state solutions will represent an approximate superposition of symmetry-limit solutions corresponding to the

$$\begin{aligned} \text{SO}(8) &\supset \text{SO}(5) \times \text{SU}(2)_p \supset \text{SO}(5) \times \text{U}(1)_c, \\ \text{SO}(8) &\supset \text{U}(4) \supset \text{U}(1)_c \times \text{SU}(4) \supset \text{SO}(5) \times \text{U}(1)_c, \quad (146) \\ \text{SO}(8) &\supset \text{SO}(7) \supset \text{SO}(5) \times \text{U}(1)_c, \end{aligned}$$

dynamical symmetry chains illustrated in Fig. 27, which for brevity will be termed the $\text{SO}(5) \times \text{SU}(2)$, $\text{SU}(4)$, and $\text{SO}(7)$ symmetries, respectively.

1. Another useful generator basis

To leverage some results already worked out in the existing literature for coherent states, it is useful to introduce a new basis P'_μ for the particle-hole operators B_{ab} in Eq. (120) that is given by

$$P'_\mu = \sum_{m_j m_l} (-1)^{\frac{3}{2}+m_l} \langle \frac{3}{2} m_j \frac{3}{2} m_l | r \mu \rangle B_{m_j - m_l}, \quad (147)$$

with the definition

$$B_{m_j - m_l} \equiv \sum_{m_k} c_{m_j m_k}^\dagger c_{-m_l m_k} - \frac{1}{4} \delta_{m_j - m_l} \Omega, \quad (148)$$

where the table in Fig. 25(a) provides a one-to-one mapping between $m_i; m_j$ values and ab values for the index on B ,

$$m_i = \left\{ \frac{3}{2}, \frac{1}{2}, -\frac{1}{2}, -\frac{3}{2} \right\} \longleftrightarrow a = \{1, 2, 3, 4\}.$$

As an example, from Fig. 25(a) $B_{ab} = B_{12}$ and $B_{m_j m_l} = B_{3/2, 1/2}$ label the same quantity, which is defined through either Eq. (120) or Eq. (148).

The index r in Eq. (147) can take values $r = 0, 1, 2, 3$, with $2r + 1$ projections μ for each possibility, giving a total of 16 operators P'_μ . By inserting explicit values of the Clebsch-Gordan coefficients in Eq. (147), the 16 independent P'_μ may be evaluated in terms of the 16 independent B_{ab} . These are worked out in Ref. [23] and in Section 3 of the Supplement [1]. A number operator n_i may be introduced through

$$n_i \equiv B_{ii} = \sum_{m_k} c_{i m_k}^\dagger c_{i m_k} - \frac{\Omega}{4}, \quad (149)$$

where 2Ω is the degeneracy of the space for particles contributing to $\text{SO}(8)$ symmetry. It is also useful to define

$$S_0 \equiv \frac{n - \Omega}{2} = P_0^0, \quad (150)$$

where a total particle number operator

$$n \equiv \sum_a n_a = n_1 + n_2 + n_3 + n_4, \quad (151)$$

[a labels the 4 basis states in Fig. 25(a)] has been introduced. Physically, S_0 may be interpreted as half the particle number measured from half filling ($n = \Omega$). Summarizing, our coherent state discussion will be formulated in the $\text{SO}(8)$ generator basis (called the nuclear $\text{SO}(8)$ basis in the Supplement [1])

$$G'_{\text{SO}(8)} = \{P^1, P^2, P^3, S_0, S, S^\dagger, D_\mu, D_\mu^\dagger\}. \quad (152)$$

where S_0 is defined in Eq. (150). The $\text{SO}(8)$ commutation algebra for the generators (152) is given in Ref. [23] and in Section 5 of the Supplement [1].

2. $\text{SO}(8)$ coherent state energy surfaces

In terms of the generators in Eq. (152), the Hamiltonian may be written

$$H = H_0 + G_0 S^\dagger S + G_2 D^\dagger \cdot D + \sum_{r=1,2,3} b_r P^r \cdot P^r, \quad (153)$$

where we define

$$D^\dagger \cdot D \equiv \sum_{\mu} D_{\mu}^{\dagger} D_{\mu} \quad P^r \cdot P^r \equiv \sum_{\mu} P_{\mu}^r P_{\mu}^r, \quad (154)$$

the G_0 , G_2 , and b_r are effective interaction strengths in the collective subspace, and we shall approximate H_0 as constant. The coherent state solution isn't restricted to the dynamical symmetry limits but it is instructive physically to evaluate the coherent state energy surface for each dynamical symmetry limit. For the three SO(8) dynamical symmetry chains of Eq. (146) the coherent state total energy surface can be parameterized as [41]

$$E_g(n, \beta) = \langle H \rangle \\ = N_g [A_g \beta^4 + B_g(n) \beta^2 + C_g(n) + D_g(n, \beta)], \quad (155)$$

where n is particle number and β is the single order parameter characterizing these states (β measures AF order and indicates the mixture of S and D_{μ} pairs in the ground state; the alternative AF order parameter $\langle N_z \rangle$ is maximal at the values of β that correspond to minimum total energy). The parameters appearing in Eq. (155) depend on the group g and are tabulated in Ref. [23]. The ground states at fixed $n/2\Omega$ will be given by those values of $\beta \equiv \beta_0$ that correspond to minima of the energy surface $E(n, \beta)$. Evaluation of these constraints for Eq. (155) indicates that minima correspond to [41]

$$\beta_0^{\text{SU}(2) \times \text{SO}(5)} = 0 \quad \beta_0^{\text{SO}(7)} = 0, \\ \beta_0^{\text{SU}(4)} = \pm \sqrt{n/4\Omega}, \quad (156)$$

for the three dynamical symmetries defined in Eq. (146) that are labeled SO(5) \times SU(2), SU(4), and SO(7), respectively. Coherent state total energy surfaces for these symmetries are shown in Fig. 28(a-c).

3. Physical interpretation of energy surfaces

The nature of the energy surfaces displayed in Fig. 28(a-c) is interpreted physically in Fig. 28(d-f). The coherent state wavefunction for $N = \frac{1}{2}n$ pairs is a superposition of terms having different pair numbers p , since it is an approximation that conserves only average particle number [23, 41],

$$|\text{SO}(5) \times \text{SU}(2)\rangle = \sum_p C_p (S^\dagger)^p |0\rangle \simeq (S^\dagger)^N |0\rangle, \\ |\text{SU}(4)\rangle = \sum_p C_p (S^\dagger \pm D_0^\dagger)^p |0\rangle \\ = 2 \sum_p C_p (Q_{\pm}^\dagger)^p |0\rangle \simeq (Q_{\pm}^\dagger)^N |0\rangle, \quad (157)$$

where the C_p are given in Ref. [41], S^\dagger and Q_{\pm}^\dagger are defined in Eqs. (127) and (129) (and Fig. 26), and the final approximations are justified because the fluctuation in particle number is small for extended physical systems and sums in (157) are dominated by terms with $p \sim N$ [23]. From Eq. (157),

1. The SO(5) \times SU(2) ground state in Fig. 28(d) is a coherent superposition of S pairs, with order parameters $\langle S_z \rangle$, $\langle T_z \rangle$, and $\langle N_z \rangle$ or $\langle \beta \rangle$ all equal to zero.
2. The SU(4) ground state in Fig. 28(f) is a coherent superposition of Q_- or Q_+ pairs with finite AF order parameters $\langle N_z \rangle$ or $\langle \beta \rangle$, but vanishing ferromagnetic $\langle S_z \rangle$ and charge density wave $\langle T_z \rangle$ order. The symmetry is broken spontaneously if one of the degenerate energy minima at finite β is chosen as the physical ground state.
3. The SO(7) ground state in Fig. 28(e) is a superposition of S and Q_{\pm} pairs that resembles an SO(5) \times SU(2) state if $\beta \sim 0$, and resembles an SU(4) AF state if $\beta \sim \pm\beta_0$:

$$|\beta = 0\rangle \propto (S^\dagger)^N |0\rangle \quad [\sim \text{SO}(5) \times \text{SU}(2)], \quad (158a)$$

$$|\beta = \beta_0\rangle \propto (Q_+)^N |0\rangle \quad [\sim \text{SU}(4) \text{ AF}], \quad (158b)$$

$$|\beta = -\beta_0\rangle \propto (Q_-)^N |0\rangle \quad [\sim \text{SU}(4) \text{ AF}], \quad (158c)$$

where the degenerate energy minima β_0 in the SU(4) limit are given by

$$\beta = \beta_0 = \pm \left(\frac{n}{4\Omega} \right)^{1/2}. \quad (159)$$

Undoped graphene has $n = \Omega$ in the ground state so that $\beta_0 = \pm \frac{1}{2}$. It follows that the fluctuations in β suggested by the flat regions of Fig. 28(e) are *maximal*: they represent excursions over the full range of β consistent with SO(8) \supset SU(4) symmetry for a Landau level with n electrons. The flat energy surface indicates that in the SO(7) ground state many configurations having large differences in β are *nearly degenerate in energy*.

Thus the SO(5) \times SU(2) and SU(4) symmetries may be distinguished by the order parameters $\langle N_z \rangle$ or $\langle \beta \rangle$, which are finite in the SU(4) state but vanish in the SO(5) \times SU(2) state. The SO(7) dynamical symmetry is characterized by *maximal fluctuations in $\langle \beta \rangle$* . It is an example of a *critical dynamical symmetry*, which will be discussed further in Section XV M.

K. Quantum phase transitions

Transitions between different dynamical symmetry chains correspond to quantum phase transitions, which can be studied by varying control parameters in coherent state approximation. In Ref. [23] the approximate SO(8) coherent state Hamiltonian

$$H = G_0 S^\dagger S + b_2 P^2 \cdot P^2, \quad (160)$$

was employed to study transitions among the quantum phases associated with the dynamical symmetries in Eq. (146). Approximate Casimir expectation values associated with dominant symmetries of the subgroup chains are [23]

$$\langle C_{\text{SO}(5) \times \text{SU}(2)} \rangle \sim \langle S^\dagger S \rangle \quad \langle C_{\text{SU}(4)} \rangle \sim \langle P^2 \cdot P^2 \rangle \\ \langle C_{\text{SO}(7)} \rangle \sim \langle S^\dagger S \rangle + \langle P^2 \cdot P^2 \rangle.$$

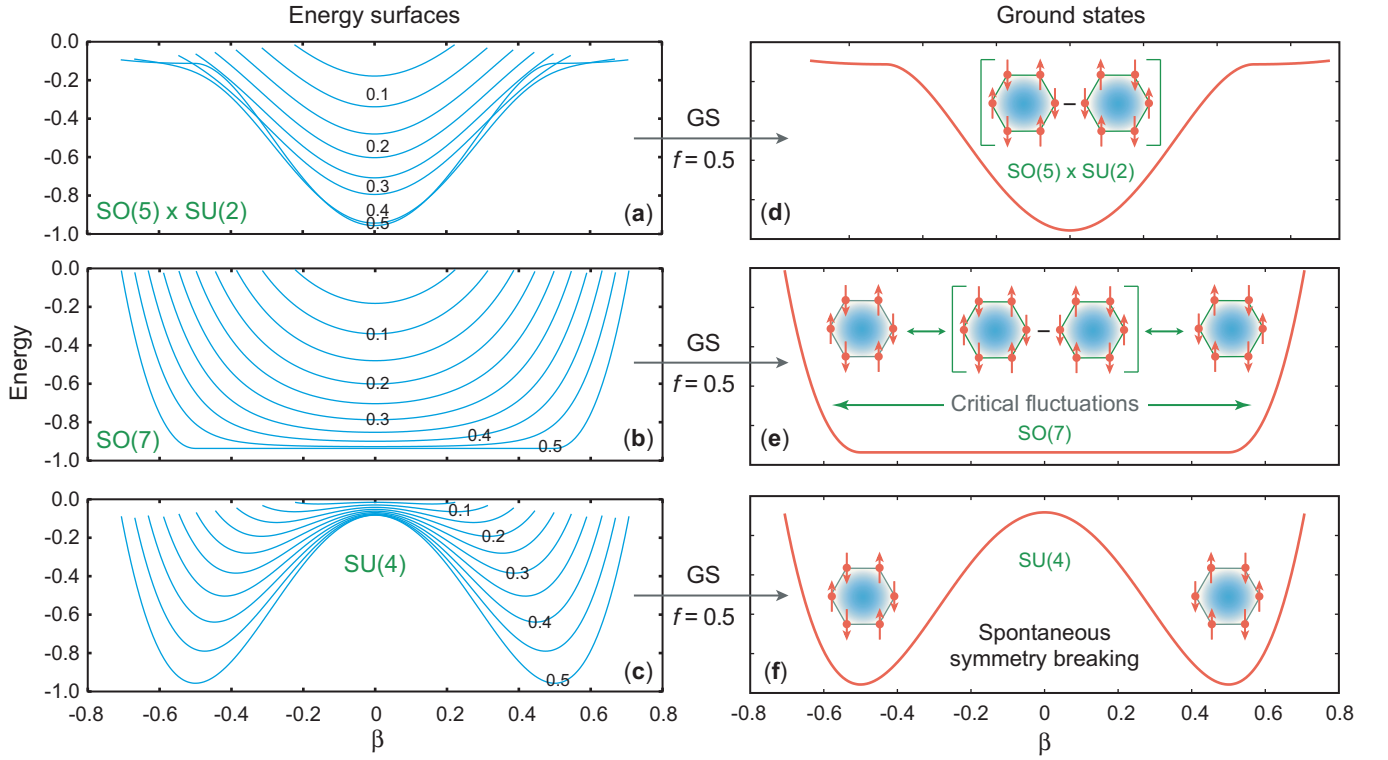


FIG. 28: Coherent state energy surfaces for a single layer of undoped graphene in a magnetic field [26]. These figures are slices along a particular axis; full diagrams are multidimensional. (a)-(c) Energy surfaces vs. AF order parameter β for the dynamical symmetry limits of Fig. 27 that are displayed in Eq. (146). Curves are labeled by fractional occupation $f = n/2\Omega$ defined in Eq. (105). (d)-(f) Ground-state ($f = 0.5$) energy surfaces corresponding to (a)-(c), respectively. The inset diagrams in (d)-(f) represent schematically the corresponding ground-state wavefunctions in terms of the configurations in Fig. 26.

The Hamiltonian (160) can be rewritten,

$$H = G_0(S^\dagger S + qP^2 \cdot P^2), \quad (161)$$

where a control parameter $q = b_2/G_0$ has been defined that tunes the Hamiltonian between $SU(2) \times SO(5)$ and $SU(4)$ phases, via an intermediate quantum critical $SO(7)$ phase.

1. If $q \ll 1$ the ground-state energy surface is approximated by Fig. 28(d), with a minimum at $\beta = 0$, no AF order, and $SU(2) \times SO(5)$ dynamical symmetry.
2. If $q \gg 1$ the ground-state energy surface is approximated by Fig. 28(f), with a set of degenerate energy minima at $|\beta| \neq 0$, spontaneously broken symmetry corresponding to $SU(4)$ dynamical symmetry, and antiferromagnetic order.
3. If $q \sim 1$, the ground-state energy is approximated by Fig. 28(e), with large fluctuations in AF order parameter β and $SO(7)$ critical dynamical symmetry.

Figure 29(a) illustrates $SO(8)$ quantum phase transitions controlled by varying q in Eq. (161). The heavy solid red curve near $q \sim 1$ corresponds to the quantum phase transition

$$SO(5) \times SU(2) \longleftrightarrow SU(4),$$

mediated by the $\sim SO(7)$ critical dynamical symmetry. Quantum phase transitions may also be induced at constant q by using the filling fraction f of Eq. (105) to vary particle number, as in Fig. 29(b). The heavy solid red curve at

$$f = \frac{n}{2\Omega} \sim 0.25$$

then defines the $\sim SO(7)$ critical-phase boundary between the $SO(5) \times SU(2)$ and $SU(4)$ quantum phases.

L. Universality of Emergent States

The fermion dynamical symmetries described for graphene in this review have many similarities with symmetries observed in other many-body systems. Figure 30 illustrates an impressive *universality of emergent dynamical symmetries* that is observed over a range of disciplines. As illustrated at the bottom of each column of figures in Fig. 30, these systems differ fundamentally at the microscopic level in properties such as characteristic distance and energy scales, forces responsible for interactions, constituent particles, and the nature of single-particle states. Yet the energy surfaces exhibit a clear similarity manifested through a similar Lie group structure (and thus a similar symmetry-dictated truncation of the respective Hilbert spaces) for the symmetries leading to emer-

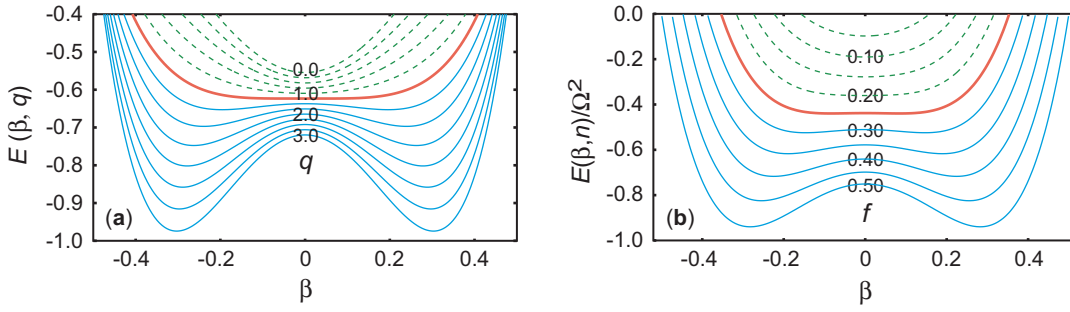


FIG. 29: Total energy surfaces illustrating SO(8) quantum phase transitions for graphene in a magnetic field. Dashed green curves correspond to $\sim \text{SO}(5) \times \text{SU}(2)$ symmetry, solid blue curves to $\sim \text{SU}(4)$ symmetry, and the heavier solid red curve corresponds to SO(7) critical dynamical symmetry occurring near the transition from $\text{SO}(5) \times \text{SU}(2)$ to $\text{SU}(4)$. (a) Phase transition with particle number fixed and coupling strength ratio q as the control parameter. The figure shows coherent state energy surfaces as a function of $q \equiv G_0/b_2$ for a fractional occupation $f = n/2\Omega = 0.5$. (b) Phase transition with coupling strength fixed and particle number as the control parameter. The figure shows coherent state energy surfaces labeled by filling fractions $f = n/2\Omega$ at fixed $q = 2.5$.

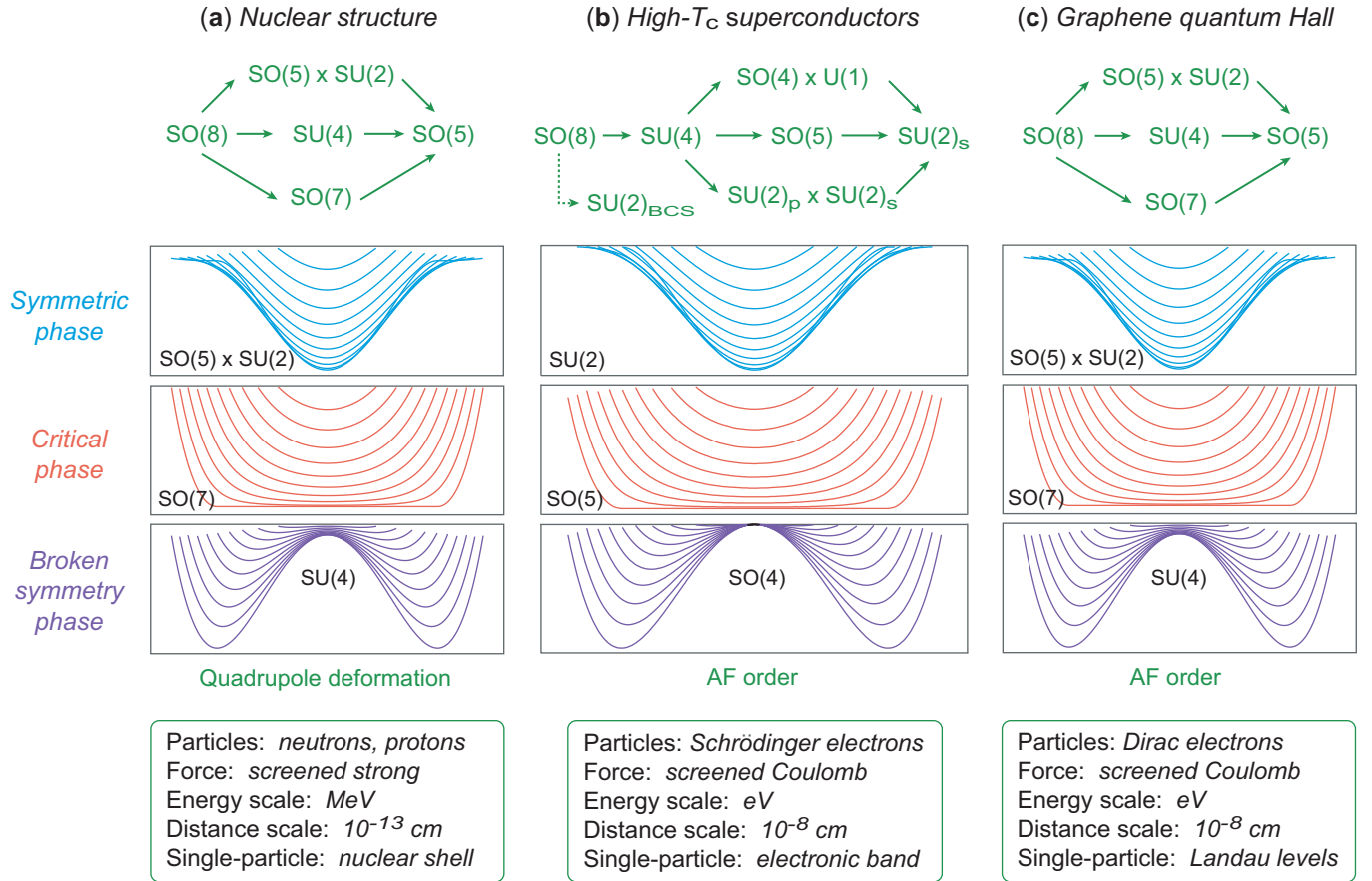


FIG. 30: Dynamical symmetry chains and ground coherent-state energy surfaces for fermion dynamical symmetry in (a) nuclear structure [4, 31], (b) high-temperature superconductivity [35, 42], and (c) monolayer graphene in a strong magnetic field [26]. Plots show total energy as a function of an appropriate order parameter, with each curve corresponding to a different value of a particle number parameter.

gent states. Although the symmetries are different for the different physical systems represented in each column, each row of energy surfaces in Fig. 30 describes a similar level of symmetry breaking. In mean field language, the top row corresponds to no breaking of the symmetry measured by the order parameter on the horizontal axis (quadrupole deforma-

tion for the nuclear case, and two kinds of antiferromagnetism for the superconductor and graphene cases, respectively), the bottom row corresponds to the breaking of that symmetry, and the middle row corresponds to a critical dynamical symmetry mediating between symmetric and broken symmetry phases. These results suggest a new kind of *universality* building on

an abstract similarity in Lie algebras for the truncated Hilbert space of emergent modes in physically very different systems, with the similarities encoded in the Lie algebras and the differences reflected in the effective interaction parameters entering the dynamical symmetry Hamiltonian.

Universality of Emergent States Hypothesis: Fermion dynamical symmetries encode collective macroscopic similarities of emergent states; effective interactions parameterize smoothly the differences that follow from underlying microscopic structure for those macroscopic states that has been averaged out by the symmetry-dictated truncation of the full space. The resulting fermion dynamical symmetries can provide similar descriptions of emergent states in physically very different systems.

This universality of emergent states through similarity of the Lie algebras controlling their collective emergent properties extends well beyond qualitative descriptions: dynamical symmetries provide microscopic descriptions of phenomena within given subfields. For example, Fig. 30 provides a unified picture of emergent states in atomic nuclei, high-temperature superconductors, and graphene in terms of their total energy surfaces, but at the same time, these methods provide a *quantitative description* through a systematic methodology for calculating matrix elements of the interesting observables in each physical system [23, 31, 32].

M. Critical Dynamical Symmetries

The $SO(8) \supset SO(7)$ dynamical symmetry chain shown in Eq. (145) is an example of a *critical dynamical symmetry (CDS)* [43], which is observed with strikingly common features in nuclear structure physics [31, 41, 43], high-temperature superconductors [32, 35, 42], and in the present discussion of monolayer graphene in magnetic fields [23, 26, 33]. Figure 30 illustrates the remarkable universality of critical dynamical symmetries across these varied fields.

- The $SO(8) \supset SO(7)$ symmetry in Fig. 30(a), which is observed in nuclear structure physics,
- the $SU(4) \supset SO(5)$ symmetry in Fig. 30(b), which is observed in high-temperature superconductors, and
- the $SO(8) \supset SO(7)$ symmetry in Fig. 30(c), which has been proposed here for monolayer graphene in a magnetic field,

all exhibit a common set of properties characteristic of critical dynamical symmetry.

1. The energy surface is extremely flat as a function of one or more order parameters for a range of control parameters.

2. The flat energy surfaces associated with critical dynamical symmetries imply an infinity of nearly degenerate ground states having very different wavefunctions and values of the order parameter(s).
3. Critical dynamical symmetries can lead to *interpolating phases*, in which order-parameter fluctuations can establish a doorway between two different phases; see Fig. 28(e). Thus they may play a role in facilitating quantum phase transitions.
4. In all cases observed thus far, a CDS doorway connects a phase exhibiting spontaneously broken symmetry to one where the symmetry has been restored; Figs. 28 and 29 give examples.
5. The flat energy surfaces characteristic of critical dynamical symmetry are conducive to fluctuations produced by perturbations and corresponding *complexity* (extreme sensitivity of observables to initial conditions) [32, 44].
6. A critical dynamical symmetry may be viewed in some sense as a generalization of a quantum critical point that extends critical fluctuations to an entire *quantum critical phase*.

Because of these properties, we have proposed that critical dynamical symmetry may be a fundamental organizing principle for quantum criticality and for quantum phase transitions in complex systems that exhibit multiple emergent modes [32].

Note finally that the flat energy surfaces for critical dynamical symmetries imply the existence of many nearly degenerate classical ground states, distinguished by different values of order parameters and by different wavefunction components. This suggests that in a quantum variational sense a better ground state with lower energy could be found by using the *generator coordinate method* (see Ch. 8 of Ref. [4] for an introduction) to obtain a new ground state that is a superposition of the nearly degenerate quantum critical states. We have suggested that an emergent state obtained by applying the generator coordinate method to the critical $SO(5)$ phase in Fig. 30(b) may be largely responsible for pseudogap features observed in high temperature superconductors [32]. The critical $SO(7)$ graphene energy surface in Fig. 30(c) is, up to scaling of axes, almost identical to the critical $SO(5)$ energy surface in Fig. 30(b). This raises the question of whether similar generator coordinate states might exist in graphene, and what their properties would be.

XVI. SUMMARY AND CONCLUSIONS

We have given a general overview of monolayer graphene, and of the highly collective emergent states that appear in the presence of a strong magnetic field. After summarizing the conventional view of these states we have shown that they also may be described in terms of fermion dynamical symmetries corresponding to subgroup chains originating in an $SO(8)$

highest symmetry and that conserve charge and spin. The previously known quantum Hall ferromagnetic SU(4) symmetry of graphene in strong magnetic fields has been extended by adding to the one-body SU(4) operators a set of two-body operators that create or annihilate fermion pairs in either (1) a total valley isospin triplet, total spin singlet state, or (2) a total valley isospin singlet, total spin triplet state. This extended set of 28 (16 particle-hole and 12 pairing) operators closes an SO(8) Lie algebra under commutation. A rich set of low-energy collective modes is found associated with the subgroup structure of SO(8), which has seven dynamical symmetry subgroup chains (implying seven distinct emergent quantum phases) that have SO(8) as a highest symmetry and states that conserve spin and charge.

It was possible to decouple a subspace of collective pairs from the full Hilbert space of the problem by exploiting the established methodology of fermion dynamical symmetries. This permitted exact, analytical, many-body solutions to be obtained in the dynamical symmetry limits. In addition to exact solutions in specific dynamical symmetry limits, a generalized SO(8) coherent state approximation was introduced that permits a broad range of generic solutions to be obtained that extend quantitative calculations beyond the dynamical symmetry limits.

The pairs spanning the collective subspace were shown to be equivalent mathematically to pairs that have already been discussed in the graphene literature [24], and to define possible ground states with spontaneously broken symmetry created by strong electron-electron and electron-phonon correlations in the $n = 0$ Landau level. The present development (1) places these pairs on a firm, unified mathematical footing and (2) permits analytical solutions for emergent states that required numerical simulation for their quantitative description in previous work.

Finally, it has been shown that there are uncanny dynamical symmetry analogies among emergent states for graphene in a strong magnetic field, high temperature superconductors, and strongly collective states in atomic nuclei. This implies a deep and intriguing mathematical affinity for emergent states among physical problems that have very different microscopic structures and are not usually viewed as having more than a superficial connection.

Appendix A: Resistivity and conductivity tensors

In simple conductors a current flows in the same direction as an applied electric field, governed by the basic form of *Ohm's Law*, $I = V/R$, with the resistance R , the voltage V , and the current I being scalar quantities. This also may be expressed in terms of the electric field E and current density j as $j = \sigma E$ or $E = \rho j$, where σ is the conductivity scalar and $\rho = \sigma^{-1}$ is the resistivity scalar. However, in the classical Hall effect a current flows perpendicular to an applied electric field because of an applied magnetic field. In such more general cases σ and ρ become tensors and Ohm's Law takes the form $\mathbf{j} = \boldsymbol{\sigma} \mathbf{E}$ or $\mathbf{E} = \boldsymbol{\rho} \mathbf{j}$, where \mathbf{j} is the current density vector and \mathbf{E} is the electric field vector. In 2D the *conductivity tensor* $\boldsymbol{\sigma}$ and

resistivity tensor $\boldsymbol{\rho}$ can be expressed as 2×2 matrices,

$$\boldsymbol{\sigma} = \begin{pmatrix} \sigma_{11} & \sigma_{12} \\ \sigma_{21} & \sigma_{22} \end{pmatrix} = \begin{pmatrix} \sigma_{xx} & \sigma_{xy} \\ \sigma_{yx} & \sigma_{yy} \end{pmatrix}, \quad (\text{A1})$$

$$\boldsymbol{\rho} = \begin{pmatrix} \rho_{11} & \rho_{12} \\ \rho_{21} & \rho_{22} \end{pmatrix} = \begin{pmatrix} \rho_{xx} & \rho_{xy} \\ \rho_{yx} & \rho_{yy} \end{pmatrix}, \quad (\text{A2})$$

where the components are $\sigma_{ij} = j_i/E_j$ and $\rho_{ij} = E_i/j_j$. Thus Ohm's Law generalizes to a matrix equation, $j_i = \sigma_{ij}E_j$ or $E_i = \rho_{ij}j_j$ (implied sum on repeated indices), with the interpretation that a non-zero σ_{ij} means that an electric field in the j direction produces a current density in the i direction. Only for the diagonal elements are the applied field and current in the same direction. The conductivity and resistivity tensors are now related by matrix inversion:

$$\begin{aligned} \boldsymbol{\rho} = \boldsymbol{\sigma}^{-1} &= \begin{pmatrix} \sigma_{xx} & \sigma_{xy} \\ \sigma_{yx} & \sigma_{yy} \end{pmatrix}^{-1} = \begin{pmatrix} \sigma_{xx} & \sigma_{xy} \\ -\sigma_{xy} & \sigma_{xx} \end{pmatrix}^{-1} \\ &= \frac{1}{\sigma_{xx}^2 + \sigma_{xy}^2} \begin{pmatrix} \sigma_{xx} & -\sigma_{xy} \\ \sigma_{xy} & \sigma_{xx} \end{pmatrix}, \end{aligned}$$

where $\sigma_{yx} = -\sigma_{xy}$ and $\sigma_{xx} = \sigma_{yy}$ have been assumed, and

$$\begin{aligned} \boldsymbol{\sigma} = \boldsymbol{\rho}^{-1} &= \begin{pmatrix} \rho_{xx} & \rho_{xy} \\ \rho_{yx} & \rho_{yy} \end{pmatrix}^{-1} \\ &= \frac{1}{\rho_{xx}^2 + \rho_{xy}^2} \begin{pmatrix} \rho_{xx} & -\rho_{xy} \\ \rho_{xy} & \rho_{xx} \end{pmatrix}. \end{aligned}$$

For the Hall effect in 2D, the *Hall resistance* R_H is related to the *Hall resistivity* by $R_H = -\rho_{xy}$, the *Hall conductivity* σ_H is given by $\sigma_H = \sigma_{xy}$, and the *diagonal conductivity* is σ_{xx} . The voltages V_H and V_L in Fig. 10 are commonly measured in a Hall experiment. Thus it is often convenient to work with resistance rather than resistivity, with

$$R_H \equiv \frac{V_H}{I} \quad (\text{Hall resistance}) \quad (\text{A3})$$

$$R_L \equiv \frac{V_L}{I} \quad (\text{Longitudinal resistance}). \quad (\text{A4})$$

Ordinarily resistance implies energy dissipation through impurity scattering. The Hall resistance R_H has the units of resistance but no energy dissipation is associated with it in a clean system. It is *defined* by the ratio of measured quantities V_H and I .

Appendix B: Anderson localization

The effect of impurity scattering on electrical conductivity of ten is discussed in terms of the *Anderson model* of localization [45]. The model consists of a system of atomic levels at different lattice sites with a hopping term allowing electrons to jump from one site to another (in the simplest approximation, only between nearest-neighbor sites). It is then assumed that the energy of an electron on each site is not constant, but varies randomly over some range w to simulate the effect of

impurity scattering. The Hamiltonian for sites labeled by n with one orbital per site is

$$H = \sum_n \varepsilon_n a_n^\dagger a_n + V \sum_{\{nm\}} a_n^\dagger a_m, \quad (\text{B1})$$

where brackets on the summation indices signify a restriction to nearest-neighbor hopping. If $w = 0$, all sites have the same energy, the resulting eigenstates are Bloch states delocalized over the entire system, and a band structure results for which electron transport is approximately ballistic. On the other hand, in the limit $V = 0$ there is no hopping between sites, the states are localized, and there is no electron transport. Thus this simple Hamiltonian implements a metal–insulator transition controlled by the ratio w/V . If w/V is small the material is conducting but if w/V is large the states are localized and the material becomes insulating. This suppression of conductivity by impurity scattering is termed *Anderson localization* and the corresponding transition between conducting and insulating phases is termed the *Anderson transition*. The Anderson model is difficult to solve exactly but concepts derived from it are common in discussing the conductor–insulator transition.

It might be expected that this metal–insulator transition would involve a smooth interpolation between the two regimes near a finite critical value of w/V . This is approximately true in $d = 3$ dimensions, but for $d \leq 2$ it is found that *an infinitesimal value for w/V is sufficient to destroy conductivity completely*, except in certain special cases. Thus, an unperturbed 2D electron gas is expected to be insulating, except in the clean limit. However, this conclusion can be avoided in the presence of a magnetic field, which breaks time-reversal symmetry and interferes with localization. In 3D,

1. when $w/V > (w/V)_{\text{crit}}$, there are no extended states but
2. when $w/V < (w/V)_{\text{crit}}$, extended and localized states coexist, separated by a *mobility edge* E_c

Extended (conducting) states have energy $E > E_c$ and localized (insulating) states have $E < E_c$, with the conductivity tending smoothly to zero as w/V approaches $(w/V)_{\text{crit}}$ from below. The 2D electron gas in a magnetic field has similar behavior, with both extended and localized states separated by a mobility edge; this is central to explaining the integer quantum Hall effect in Section VII B 1. For further discussion of localization, see Ch. 12 of Phillips [9].

Appendix C: The Gauss–Bonnet and Chern theorems

For a 2D surface there is a relationship between its geometry and its topology called the *Gauss–Bonnet theorem*, which may be expressed through the *Gauss–Bonnet equation*,

$$\frac{1}{2\pi} \int_S K dA = 2(1 - g), \quad (\text{C1})$$

where the integral is over a closed surface S , the local curvature is K , and g is the genus of the surface (number of “holes”),

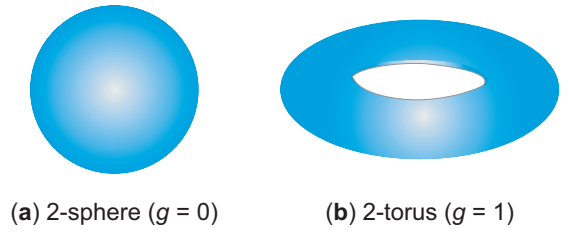


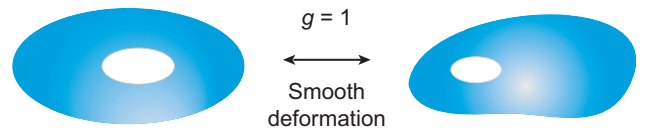
FIG. 31: (a) The 2D sphere, which has genus $g = 0$. (b) The 2D torus, which has genus $g = 1$.

which characterizes its topology). The Gauss–Bonnet theorem relates the geometrical properties of the 2-surface (carried by the local curvature K on the left side) and its topological properties (carried by the genus g on the right side), with g a topological invariant since the number of holes is unchanged by smooth deformations of the surface. For example, consider the 2D manifolds displayed in Fig. 31. For the sphere, inserting $g = 0$ and the Gaussian curvature $K = R^{-2}$ in Eq. (C1) gives the expected result, $A = 4\pi R^2$. For the torus the integral on the left side of Eq. (C1) vanishes (because the torus has regions of positive and negative curvature K that cancel exactly), which is consistent with Eq. (C1) only if $g = 1$, as expected for the torus.

One fundamental implication of the linkage of geometry and topology for a 2-surface implied by Eq. (C1) is illustrated in Fig. 32. Because the integer $2(1 - g) = 0$ for $g = 1$ on the right side of Eq. (C1) cannot change continuously into another integer for a small, smooth deformation of the surface, *the integral on the left side cannot change under this deformation either*. Thus, in Fig. 32 the left side is *topologically protected* against change for smooth deformations that do not change the genus.

The Gauss–Bonnet equation (C1) relates geometry and topology for spatial manifolds, but in 1944 S.-S. Chern generalized the Gauss–Bonnet equation to the *Gauss–Bonnet–Chern equation* (which for brevity we will term the *Chern equation*),

$$\frac{1}{2\pi} \int_S \Omega dA = C_n. \quad (\text{C2})$$



$$\text{Topological protection: } \frac{1}{2\pi} \int_S K dA = 0$$

FIG. 32: Smooth deformations that do not change the genus g cannot change the Gauss–Bonnet topological invariant defined by the curvature K integrated over the surface in Eq. (C1). The curvature may be changed locally by a smooth deformation but $\int_S K dA$ is topologically protected if the deformation does not alter the genus for the surface. Adapted from Ref. [4].

This resembles the Gauss–Bonnet formula (C1), except that for n a positive integer,

1. Equation (C2) is valid for any $2n$ -dimensional closed Riemannian manifold.
2. The *Chern index* C_n on the right side of (C2) is an integer that labels a *Chern class*.
3. The *Berry curvature* Ω is evaluated over a closed manifold of quantum states defined on S .
4. The Chern index C_n isn't determined by the genus of the surface S , as in (C1), but rather by *the topology of a manifold of quantum states (the Hilbert space)* defined over S .

For 2D manifolds the index C_n is a *Chern number of the first kind* C_1 , which takes values from the set of integers Z . General implications of Eq. (C2) will be termed the *Chern theorem*.

Chern Theorem: The integral of Berry curvature over a closed manifold of quantum states is quantized in terms of topological Chern numbers that take integer values.

By analogy with the Gauss–Bonnet equation (C1) and Fig. 32, Eq. (C2) is topologically protected under smooth deformations that do not change the Chern number on its right side; the Chern number can be changed only by a *phase transition* to a state having a different topology. As discussed in Section VII B 4, this topological protection accounts for the remarkable flatness of the plateaus in Fig. 9.

Readable general introductions to topological properties of the quantum Hall effect may be found in Ref. [14] and in Ch. 28 of Ref. [4]. For a more mathematical discussion of Chern classes in physics, see Frankel [46] or Nakahara [47].

Appendix D: U(4) and SU(4) subgroups of SO(8)

From Eq. (121b), the 16 operators B_{ab} defined in Eq. (120) are closed under commutation and form a subalgebra of SO(8) corresponding to the chain (see Fig. 27)

$$\text{SO}(8) \supset \text{U}(4) \supset \text{U}(1)_c \times \text{SU}(4), \quad (\text{D1})$$

where the $\text{U}(1)_c$ factor corresponding to conservation of electron number (charge) is generated by S_0 defined in Eq. (150), and the $\text{SU}(4)$ factor is generated by the 15 operators in Eqs. (122)–(125), but expressed in a different basis than for Eq. (120). Because of the direct product $\text{U}(1)_c \times \text{SU}(4)$ in Eq. (D1), the $\text{U}(1)_c$ and $\text{SU}(4)$ factors are independent and it is common to keep track of the particle number associated with the $\text{U}(1)_c$ factor separately and refer loosely to the symmetry associated with the generators in Eq. (120) as $\text{SU}(4)$, rather than the more precise $\text{U}(4)$ or $\text{U}(1) \times \text{SU}(4)$.

Acknowledgments

We wish to thank Yang Sun for useful discussions and Matthew Murphy for help with some of the calculations and illustrations that were used here. L.-A. W. is supported by the Basque Country Government (Grant No. IT1470- 22) and Grant No. PGC2018-101355-B-I00 funded by MCIN/AEI/10.13039/501100011033. F. W. was supported partially by LightCone Interactive LLC during the completion of this work.

-
- [1] F. Williams, L. Wu, and M. Guidry, *Supplement: Emergent fermion dynamical symmetries for monolayer graphene in a strong magnetic field*, URL http://eagle.phys.utk.edu/guidry/Graphene_suppl4.html, arXiv: 1606.06687 (2016).
- [2] M. O. Goerbig, *Rev. Mod. Phys.* **83**, 1193 (2011).
- [3] P. R. Wallace, *Phys. Rev.* **71**, 622 (1947).
- [4] M. Guidry and Y. Sun, *Symmetry, Broken Symmetry, and Topology in Modern Physics: A First Course* (Cambridge University Press, Cambridge, 2022).
- [5] K. S. Novoselov et al., *Nature* **438**, 197 (2005).
- [6] C. Bena and G. Montambaux, *New J. Phys.* **11**, 095003 (2009).
- [7] C. Kittel, *Introduction to Solid State Physics* (John Wiley and Sons, New York, 2004).
- [8] J. J. Quinn and K.-S. Li, *Solid State Physics: Principles and Modern Applications* (Springer Verlag, Berlin, 2009).
- [9] P. Phillips, *Advanced Solid State Physics* (Westview Press, Boulder, 2003).
- [10] K. von Klitzing, G. Dorda, and M. Pepper, *Phys. Rev. Lett.* **45**, 494 (1980).
- [11] J. P. Eisenstein and H. L. Stormer, *Science* **248**, 1510 (1990).
- [12] X. G. Wen, *Quantum Field Theory of Many-Body Systems* (Oxford University Press, Oxford, 2004).
- [13] D. Vanderbilt, *Berry Phases in Electronic Structure Theory* (Cambridge University Press, Cambridge, 2018).
- [14] M. O. Goerbig, *arXiv: 1606.06687* (2016).
- [15] D. C. Tsui, H. L. Stormer, and A. C. Gossard, *Phys. Rev. Lett.* **48**, 1599 (1982).
- [16] R. B. Laughlin, *Phys. Rev. Lett.* **50**, 1395 (1983).
- [17] J. K. Jain, *Composite Fermions* (Cambridge University Press, Cambridge, 2007).
- [18] M. O. Goerbig and N. Regnault, *Phys. Scr.* **T146**, 014017 (2012).
- [19] Y. Zhang et al., *Nature* **438**, 201 (2005).
- [20] K. I. Bolotin, F. Ghahari, M. D. Shulman, H. L. Stormer, and P. Kim, *Nature* **462**, 196 (2009).
- [21] B. E. Feldman, B. Krauss, J. H. Smet, and A. Yacoby, *Science* **337**, 1196 (2012).
- [22] X. Du, I. Skachko, F. Duerr, A. Luican, and E. Y. Andrei, *Nature* **462**, 192 (2009).
- [23] L.-A. Wu, M. Murphy, and M. W. Guidry, *Phys. Rev.* **B95**, 115117 (2017).
- [24] M. Kharitonov, *Phys. Rev.* **B85**, 155439 (2012).

- [25] F. Wu, I. Sodemann, Y. Araki, A. H. MacDonald, and T. Jolicoeur, *Phys. Rev.* **B90**, 235432 (2014).
- [26] L.-A. Wu and M. W. Guidry, *Sci. Rep.* **6**, 22423 (2016).
- [27] J. Jung and A. H. MacDonald, *Phys. Rev.* **B80**, 235417 (2009).
- [28] C. Chamon, *Phys. Rev.* **B62**, 2806 (2000).
- [29] C. L. Wu, D. H. Feng, X.-G. Chen, J.-Q. Chen, and M. W. Guidry, *Phys. Lett.* **B168**, 313 (1986).
- [30] C. L. Wu, D. H. Feng, X.-G. Chen, J.-Q. Chen, and M. W. Guidry, *Phys. Rev.* **C36**, 1157 (1987).
- [31] C.-L. Wu, D. H. Feng, and M. W. Guidry, *Advances in Nuclear Physics* **21**, 227 (1994).
- [32] M. W. Guidry, Y. Sun, L.-A. Wu, and C.-L. Wu, *Front. Phys.* **15**, 43301 (arXiv:2003.07994) (2020).
- [33] M. W. Guidry, *Fortschr. Phys.* **65**, 160057 (2017).
- [34] R. Bijker, F. Iachello, and A. Leviatan, *Ann. Phys.* **236**, 69 (1994).
- [35] M. W. Guidry, L.-A. Wu, Y. Sun, and C.-L. Wu, *Phys. Rev.* **B63**, 134516 (2001).
- [36] F. Iachello and A. Arima, *The Interacting Boson Model* (Cambridge University Press, Cambridge, 1987).
- [37] F. Iachello and R. D. Levine, *Algebraic Theory of Molecules* (Oxford University Press, Oxford, 1995).
- [38] F. Iachello and P. Truini, *Ann. Phys.* **276**, 120 (1999).
- [39] J. Q. Chen, D. H. Feng, and C.-L. Wu, *Phys. Rev.* **C34**, 2269 (1986).
- [40] W.-M. Zhang, D. H. Feng, and R. Gilmore, *Rev. Mod. Phys.* **62**, 867 (1990).
- [41] W.-M. Zhang, D. H. Feng, and J. N. Ginocchio, *Phys. Rev.* **C37**, 1281 (1988).
- [42] L.-A. Wu, M. W. Guidry, Y. Sun, and C.-L. Wu, *Phys. Rev.* **B67**, 014515 (2003).
- [43] W.-M. Zhang, D. H. Feng, and J. N. Ginocchio, *Phys. Rev. Lett.* **59**, 2032 (1987).
- [44] M. W. Guidry, Y. Sun, and C.-L. Wu, *Chinese Science Bulletin* **56**, 367 (2011).
- [45] P. W. Anderson, *Phys. Rev.* **109**, 1492 (1958).
- [46] T. Frankel, *The Geometry of Physics* (Cambridge University Press, Cambridge, 2012).
- [47] M. Nakahara, *Geometry, Topology and Physics* (Taylor and Francis, Boca Raton, 2003).